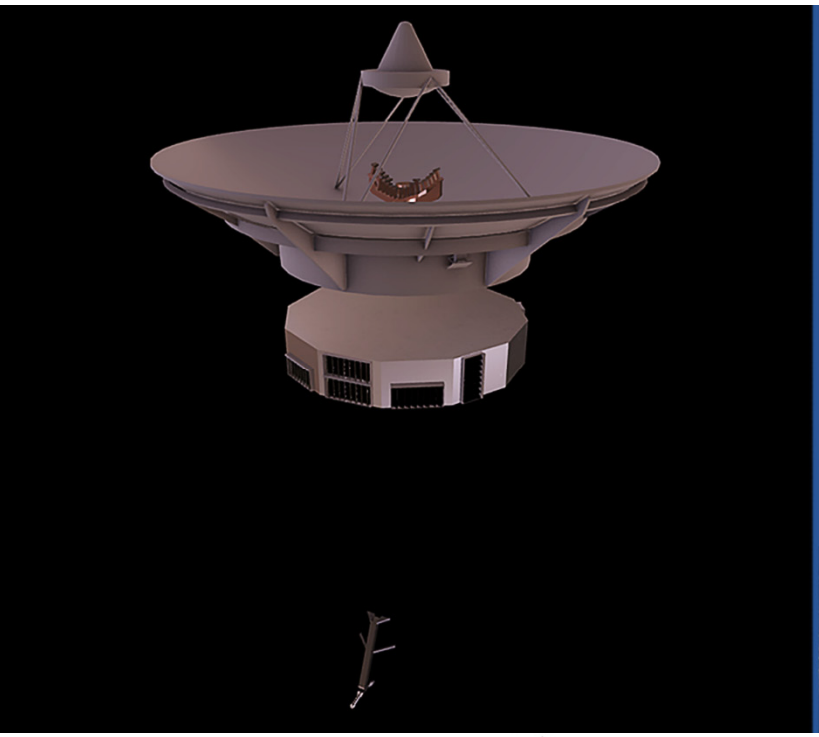

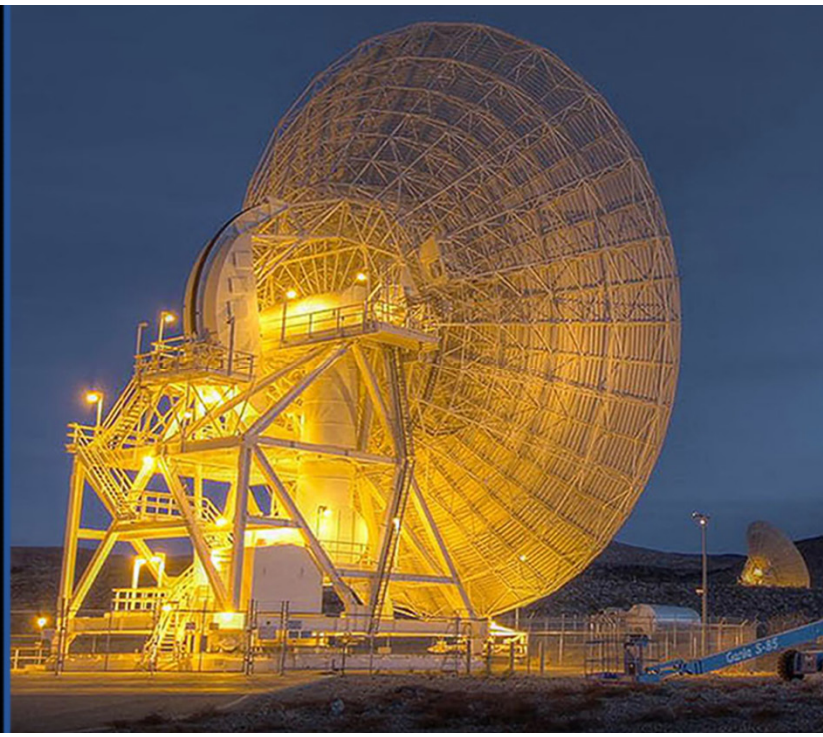

Radio Science Subsystem

The Radio Science Subsystem (RSS) used the spacecraft X-band communication link, an S-band downlink and a Ka-band uplink and downlink to study structure, composition, pressure, and temperature of atmospheres and ionospheres, ring structure, surface properties and particle sizes, body and system masses, gravity fields and gravitational waves. The **science objectives** of RSS were to study the atmospheres and ionospheres of Saturn and Titan, properties of rings, and gravity fields of Saturn and its satellites. During Cassini's cruise phase, RSS was also used to search for gravitational waves coming from beyond our solar system. Some of these experiments measured Doppler shifts (frequency shifts) and other changes to radio signals that occurred when the spacecraft passed behind Saturn, moons, as viewed from Earth to derive information about the structure and composition of the occulting bodies, atmospheres, and the rings.

RSS consists of a Ka-band traveling wave tube amplifier, a translator, an exciter; an S-band transmitter; and various microwave components. RSS used the spacecraft's Radio Frequency Subsystem (RFS) and one or more of the three Deep Space Network (DSN) antenna complexes to obtain the required scientific data. The RFS sent radio signals from Cassini spacecraft to Earth (DSN) using the spacecraft's high-gain antenna (HGA). In route, the radio signal interacted with Saturn's moons, rings or Saturn's atmosphere.

CONTENTS

RADIO SCIENCE SUBSYSTEM 1
- Executive Summary 6
- Top 20 RSS Science Highlights 6
- RSS Instrument Summary 8
  - Cruise Phase Science 9
  - Radio Frequency Subsystem 9
    - Ultra-stable oscillator 10
  - Attitude and Articulation Control Subsystem 11
  - Other Subsystems 12
  - Ground Systems 13
    - Closed-loop tracking receiver 13
    - Open-loop radio science receiver 13
- Key Objectives for RSS Instrument 14
  - Titan Science 14
    - Gravity 14
    - Atmosphere 15
    - Ionosphere 15
    - Surface—bistatic experiments 15
  - Saturn Science 15
    - Gravity 15
    - Atmosphere 16
    - Ionosphere 16
  - Enceladus Science 17
    - Gravity 17
    - Atmosphere/ionosphere 17
  - Icy Satellite Science 18
  - Ring Science 18
  - Cruise Science 19
- RSS Science Assessment 19
- RSS Saturn System Science Results 21
  - Titan Science 21
    - Gravity 21
    - Atmosphere 28
    - Ionosphere 31
    - Titan surface scattering results 32
    - Open questions 35
  - Saturn Science 36
    - Atmosphere 36
    - Ionosphere 39
    - Gravity 43
    - Open questions 47
  - Enceladus Science 48
    - Gravity 48
    - Ionosphere 51
    - Open questions 52

Icy Satellite Science 52
Phoebe 53
Iapetus 53
Hyperion 54
Dione 55
Rhea 55
Open questions 58
Ring Science 58
RSS ring occultations during the Cassini Prime Mission 58
Radial structure in the rings 60
Density waves in Saturn's rings 65
Particle size distribution 68
Periodic microstructure in Saturn's rings A and B 68
Open questions 70
RSS Non-Saturn Science Results 71
Cruise Science 71
Gravitational wave experiment 71
Solar conjunction experiment 76
Solar wind 80
Open questions 85
Acronyms 88
References 90

Figures

Figure RSS-1. Configuration for radio science observations at a generic planet. 8
Figure RSS-2. The USO output frequency scaled to X-band by the Cassini transponder over several years, showing long-term aging process as expected. 11
Figure RSS-3. Allan Deviation of the Cassini USO as a function of integration time from a representative test. 12
Figure RSS-4. Ground tracks of the 10 Titan gravity flybys showing uneven sampling of the moon's gravity. 23
Figure RSS-5. Distribution of Titan mean anomalies of the 10 gravity flybys at the time of closest approach. 24
Figure RSS-6. Estimated gravity anomalies (upper panel) and related formal uncertainties (lower panel) from the analysis of the first six Titan gravity flybys (T11–T74 (4 × 4). 27
Figure RSS-7. Vertical profiles of electron density from Titan RSS occultations, compared with other observations. ... 32
Figure RSS-8. Panels (a) and (b) depict selected geometry parameters of the Cassini T14 observations and panel (c) depicts the corresponding ground tracks. ..... **Error! Bookmark not defined.**
Figure RSS-9. Uncalibrated spectrograms of the first positive detection of bistatic echoes from Titan surface observed on the T14 flyby on May 20, 2006 (DOY 140). 35
Figure RSS-10. Weighted averages of dusk and dawn electron density profiles. 39
Figure RSS-11. Zonal gravity harmonic coefficients J_2–J_{12}. 45
Figure RSS-12. The gravity field due to C21, S21, S22, and J3 as in Table RSS-10 is mapped onto the reference ellipsoid. The negative anomaly at the South Pole, representing the asymmetry between the two hemispheres, is ~2.5 mGal. 50
Figure RSS-13. RSS observations of Rev125 Enceladus occultation. 51
Figure RSS-14. Gallery of Earth-based views of selected RSS ring and atmosphere occultations in 2007 and 2008 ... 60

Figure RSS-15. Fitted amplitudes, phases, and pattern speeds vs radius for perturbations induced at a distance by the strong Titan 1:0 ILR. 61
Figure RSS-16. An optical depth profile of the C-ring, derived from the Cassini radio occultation on Rev 7. 62
Figure RSS-17. Optical depth profile of the inner C-ring from a nearly edge-on RSS ring occultation. 63
Figure RSS-18. Prominent ringlets and gaps in the Cassini Division shown in an optical depth profile from the Cassini RSS egress occultation on Rev 7. 63
Figure RSS-19. Results found from the analysis of the Cassini Division occultation data 64
Figure RSS-20. Simulation of non-linear density wave embedded in the eccentric Maxwell Ringlet. 65
Figure RSS-21. Example Cassini RSS F-Ring core detection (ingress occultation on Rev 54, December 19, 2007) 66
Figure RSS-22. Density wave model used to analyze RSS observations of Mimas 5:3 density wave. 67
Figure RSS-23. Occultation profiles of the Janus/Epimetheus 2:1 density wave in the B1 region. 67
Figure RSS-24. Three-wavelength RSS optical depth profiles of eight ring features identified for examination of the constraints imposed by observed interesting differential extinction, or lack thereof, on parameters of a power-law size distribution model. 68
Figure RSS-25. Optical depth contrasts at multiple wavelengths and the inferred minimum and maximum particle sizes. 69
Figure RSS-26. The geometry of the ring occultation experiment used to determine the ring microstructure. 69
Figure RSS-27. The geometry of the ring occultation experiment seen in the spectra. 70
Figure RSS-28. Schematic response of two-way Doppler tracking to a GW 72
Figure RSS-29. Spectrum of two-way Doppler for the 2001–2002 Cassini observations. 73
Figure RSS-30. Sensitivity of the Cassini 2001–2002 gravitational wave observations, expressed as the equivalent sinusoidal strain sensitivity required to produce SNR = 1 for a randomly polarized isotropic background, as a function of Fourier frequency. 74
Figure RSS-31. Sensitivity of the Cassini 2001–2002 burst gravitational wave observations, expressed as characteristic strain sensitivity (GW bandwidth = center frequency) averaged over the sky and polarization state. 75
Figure RSS-32. Upper limits to GW energy density (bandwidth = center frequency) divided by the critical density required to close the universe of an isotropic GW background. 75
Figure RSS-33. Geometry of the 2002 Cassini solar conjunction. 77
Figure RSS-34. The gravitational signal. 78
Figure RSS-35. The Doppler residuals. 79
Figure RSS-36. Transfer function of plasma fluctuations to one-way and two-way phase/Doppler scintillation allows localization of plasma blobs along the line-of-sight. 81
Figure RSS-37. Time series of the plasma contribution to the X-band up- and down links, $y_{up}(t)$ and $y_{dn}(t)$, for DSS25 Cassini track on 2001 DOY 149 = 2001 May 29. 82
Figure RSS-38. Space-time cross-correlation function of the 2001 DOY 149 plasma up- and downlink time series plotted in Figure RSS-37. 82
Figure RSS-39. Map of coronal density structure at a height of 4 solar radii for Carrington Rotation 1976, calculated using a solar rotational tomography technique from ~2 weeks of LAS-CO/SOHO C2 coronagraph observations. 83

Figure RSS-40. As Figure RSS-38, but for 2002 DOY 160 = 2002 June 9. The Sun-Earth-spacecraft angle was about 9.5 degrees and the two-way light time was about 8365 seconds. 84

Tables

Table RSS-1. Cassini Radio Science Bands and Wavelengths. 10
Table RSS-2. Matrix of RSS Science Objectives. 19
Table RSS-3. Main characteristics of Titan's gravity flybys. 23
Table RSS-4. Estimated spherical harmonics coefficients. 26
Table RSS-5. Cassini Bistatic Radar Experiments 33
Table RSS-6. Summary of Cassini Radio Science Results on the Saturn Ionosphere. 40
Table RSS-7. Parameters of the osculating orbit at C/A from the RSS reconstructed trajectory 45
Table RSS-8. Saturn's gravity harmonic coefficients (unnormalized; reference radius 60330 km) and B-ring mass (in units of Mimas' mass), obtained from the analysis of Cassini's Grand Finale gravity orbits. 46
Table RSS-9. Estimates of the ring masses for the three dynamical models (stochastic, tesseral field, normal modes), in units of Mimas mass (GM_M = 2.5026 km^3/s^2). 47
Table RSS-10. Solution for the gravity field of Enceladus. 49
Table RSS-11. Mass estimation results for the Saturn icy satellites encountered by Cassini. 57
Table RSS-12. Estimated values and 1-σ formal uncertainties of Rhea's quadrupole gravity unnormalized coefficients for the Cassini Radio Science Team solution 57
Table RSS-13. RSS Ring Occultations Completed During Cassini Prime Mission 59
Table RSS-14. Overview of data times. 84
Table RSS-15. Cassini Cruise-phase Doppler noises and their transfer functions to two-way observations. 86
Table RSS-16. Required Noise improvement factors to reach ~10^{-16} Doppler noise. 87

Executive Summary

The Cassini RSS team conducted a wide-ranging series of experiments spanning the entire mission. En route to Saturn, the RSS team observed Cassini at solar conjunction, providing what is still today the most rigorous test of Einstein's theory of general relativity, and the single most frequently cited publication of the entire Cassini mission [Bertotti et al. 2003]. A second cruise experiment set new limits on the strength of low-frequency gravitational waves. Upon arrival at Saturn, a series of diametric ring occultations at three wavelengths revealed stunning detail in the rings at sub-km resolution, periodic structure in Saturn's C-ring (possible evidence of a pair of cometary collisions hundreds of years ago), incomplete clumps in the core of Saturn's F-ring, evidence of wake-driven periodic microstructure in rings A and B, and estimates of particle sizes through the main ring system. Companion Saturn atmosphere occultations over the course of the mission provided regional and seasonal information about the atmospheric thermal structure, including evidence of an equatorial oscillation, zonal winds, and complex wave structure. A suite of ionospheric observations revealed highly variable electron density profiles with evidence of ring/ionosphere interactions. Multiple Titan occultations provided accurate thermal profiles from the surface to the stratosphere over a broad range of latitudes and over the course of Saturn's seasons, and ionospheric profiles as well. Bistatic scattering experiments probed the reflectivity of Titan's surface and provided estimates of the dielectric constant of the liquid norther seas. An exquisite series of gravity field measurements during flybys revealed the presence of subsurface oceans on Titan and Enceladus, established firm measurements for the shape and degree of hydrostatic equilibrium for other icy satellites, and during the Grand Finale, determined the gravitational field of Saturn to extraordinary accuracy and determined the mass of Saturn's ring system to be lower than expected, providing strong evidence that the rings are younger than the planet itself.

En route to Saturn, the RSS team observed Cassini at solar conjunction, providing what is still today the most rigorous test of Einstein's theory of general relativity, … .

Top 20 RSS Science Highlights

Titan Science

1. **Measurement of Titan's hydrostatic gravity quadrupole and moment of inertia**, implying a partially differentiated body very different from its Jovian cousin Ganymede, with a low-density core made up by hydrated silicates.

2. **Seasonal variations in Titan's atmospheric thermal structure** from the surface to the stratosphere, with muted variations in the troposphere but larger in the middle atmosphere above 100 km, and a global minimum in the vertical profile of the zonal wind.

3. **Spatial and temporal variations of Titan's electron density structure**, with large low altitude secondary peak, possibly related to energetic ion precipitation.

4. **Bistatic observations of Titan's surface and Northern seas.**

Saturn Science

5. **Discovery of a strong differential rotation in Saturn's atmosphere**, extending down to 9000 km below the cloud level.

6. **Seasonal variations in Saturn's atmospheric thermal structure** from the cloud deck to the stratosphere, with evidence of an equatorial oscillation forced by vertically propagating waves.

7. **Spatial and temporal variations of Saturn's ionosphere**, likely affected by latitudinal variation of neutral molecules.

Enceladus Science

8. Discovery of Enceladus' subsurface ocean and interior structure.

9. Electron density observations at Enceladus.

Icy Satellite Science

10. Measurement of Rhea's quadrupole gravity field.

11. Measurement of Dione's quadrupole gravity field.

Ring Science

12. Measurement of a low mass of Saturn's rings.

13. Particle size determination of Saturn's rings.

14. Orbital properties of Saturn's rings.

15. Periodic microstructure in rings A and B.

16. Evidence for ancient impacts on Saturn's rings.

Cruise Science

17. Precision test of General Relativity.

18. Low-frequency gravitational waves.

19. Plasma turbulence in the inner heliosphere.

20. Precision navigation at solar conjunction.

RSS Instrument Summary

Radio Science experiments are typically divided into two categories: gravitation and propagation. For gravitation, the Cassini spacecraft serves as a point-mass probe within the gravity field of Saturn and its satellites; precision measurements of the Earth-Cassini distance and relative velocity can be used to infer the target body mass and higher order field components. Propagation experiments are radio occultation experiments where the occulting objects under study are planetary and satellite ionospheres and neutral atmospheres, rings, and solar plasma.

Figure RSS-1 shows typical radio science (RS) observational configuration for planetary occultations. The spacecraft transmits a signal that is refracted by the target atmosphere before being received on Earth at a ground station of NASA DSN. The direction of the arrow on the dashed ray path indicates that this is a one-way downlink observation. As the spacecraft moves, the ray probes more deeply into the atmosphere until it is absorbed or occulted by the planet itself. Stability of the signal during the observation depends on the quality of the reference oscillator onboard the spacecraft. Cassini was equipped with an ultra-stable oscillator (USO) to improve stability of its transmitted one-way signal. In two-way mode, a signal is transmitted from Earth and received at the spacecraft; this uplink signal can then be used to control the frequency of the downlink transmission. In general, the two-way mode provides better overall frequency stability than the one-way mode because of the superior quality of the atomic clocks at the ground stations. However, passage of the uplink signal through an atmosphere, ring, or plasma cloud, or reflection from a surface distorts the uplink signal making a USO-referenced one-way mode preferable. In three-

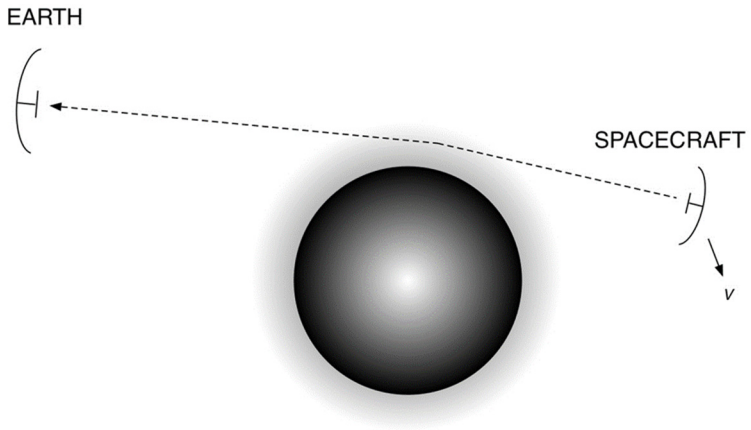

Figure RSS-1. Configuration for radio science observations at a generic planet. Spacecraft moving at velocity *v* gets occulted by the atmosphere then the planet itself.

way mode, one ground station transmits to the spacecraft and a different ground station receives; this is used when an observation spans the handover from one ground station to another. In the Cassini case, three-way was necessary because of the long one-way light time between Saturn and Earth, ranging from 68 to 84 minutes.

During occultations by Saturn, its rings, or its satellites, one-way operation yield observables which are inverted to give temperature-pressure and absorption profiles of neutral atmospheres, electron density profiles of ionospheres, and optical depth and particle size distribution profiles of rings. Most measurements are wavelength dependent and some may include polarization effects, so a wide range of transmitting and receiving equipment is desirable.

During close encounters, the spacecraft antenna is deflected from the Earth direction to point at satellite surfaces or Saturn's ring plane. Such one-way bistatic radar (BSR) experiments require the highest sampling rates of the receivers at the ground stations and contain the most interesting polarization information. Inversions can yield dielectric constant of target surfaces and size distributions for ring particles.

Cruise Phase Science

During the long Cassini phase, RS observations included gravitational wave experiments (GWEs) near solar oppositions and solar conjunction experiments (SCEs). In a GWE, subtle changes in the apparent Earth-spacecraft distance and/or relative velocity, which cannot be attributed to other causes, would indicate passage of gravitational wavefronts through space between Earth and Cassini. GWE observations were conducted in two-way mode for highest clock stability. When the spacecraft's radio signal is occulted by the Sun, then an SCE investigates the solar corona. Operationally, two-way data are collected at large solar radii; but one-way operation with open-loop reception is the practical choice for small solar radii and high solar activity. The shortest radio wavelengths are least affected by the solar plasma; multiple wavelength measurements yield total electron content along the radio path directly.

Radio Frequency Subsystem

The RFS, in conjunction with the Antenna Subsystem, provides communications between the spacecraft and ground stations of the DSN. It also provides a signal source for RS measurements. In earlier documentation—for example, Kliore et al. [2004]—a distinction was made between multi-use radio components (RFS) and RS-only components called the Radio Frequency Instrument Subsystem (RFIS) but that distinction is not maintained here and all radio components fall within the RFS. The RFS includes a pair of redundant X-band transponders for reception and transmission, an S-band transmitter, and a Ka-band transmitter. The USO provided an onboard highly stable time and frequency reference, but it failed in 2011. A Ka-band translator (KaT), which received at 34 GHz and transmitted coherently at 32 GHz, supported general relativity observations during Cruise; it failed before Saturn orbit insertion.

The RFS produces an X-band carrier modulated with data received from the Command & Data Subsystem (CDS), amplifies the modulated carrier, and delivers the signal stream to the Antenna Subsystem for transmission to Earth. It also receives and demodulates X-band commands from the ground via the Antenna Subsystem. At Saturn, where the one-way distance to Earth is 8.2–10.2 astronomical units (AU) and the one-way travel time is 68–84 minutes, commands and instructions from Earth have been received at 1000 bits per second (bps) by the HGA; and data have been transmitted to Earth at selectable rates ranging from 14,220 to 165,900 bps. Data can be recorded on the solid- state recorders for about 15 hours, while the HGA is not pointed at Earth; then they are played back for nine hours. About one gigabit of data can be returned each day via a 34-m DSN antenna; nearly four times that can be returned via a 70-m ground antenna. The two redundant recorders can record and read out nearly 2 gigabits of data simultaneously. The CDS handles combined data rates in excess of 430,000 bps from the instruments while carrying on its functions of command and control. Since RS observables are generated at the DSN, only a very small fraction of telemetry, such as equipment status and spacecraft attitude measurements, are of interest to RS.

The Antenna Subsystem includes the 4-meter diameter HGA reflector (which was also used for Sun shading in the early cruise phase); a frequency-selective subreflector; HGA feeds for S-band, X-band, Ka-band, and Ku-band; and two low-gain antennas (LGA). All antennas operate at X-band; only the HGA operates at S-band, X-band, Ka-band, and Ku-band. The X-band components are for communications and navigation as well as RS; the S-band and Ka-band components are only for RS and the Ku-band components are for the Cassini Titan Radar Mapper (RADAR). Table RSS-1 lists the RS bands.

Table RSS-1. Cassini Radio Science Bands and Wavelengths.

Band	Wavelength (cm)	Frequency (MHz) Uplink	Frequency (MHz) Uplink
S	13	N/A	2298
X	3.6	7175	8425
Ka	0.9	34316	32028

Notes: Separate S-band channels existed to receive the Huygens probe relay in two polarizations at 2040 and 2098 MHz. The X-band uplink polarization is left circular (LCP) when Transponder A is selected and right circular (RCP) when Transponder B is selected. The X-band downlink polarization is LCP when traveling wave tube amplifier A (TWTA-A) is selected and RCP when TWTA-B is selected.

Ultra-stable oscillator

Key to RS instrumentation onboard the Cassini spacecraft, the USO provided the highly stable reference generated on-board the spacecraft until it failed in 2011. The Cassini oscillator is in the class of highest performance thermally-controlled quartz crystal oscillators flown on planetary missions. It was manufactured by Johns Hopkins University, Applied Physics Laboratory. Figure RSS-2 shows the X-band output frequency of the USO over several years showing long-term aging behavior (without accounting for time dilation effects).

Figure RSS-3 shows the excellent Allan Deviation performance of the USO stability as a function of integration time from one representative test in 2011. These data in reality characterize

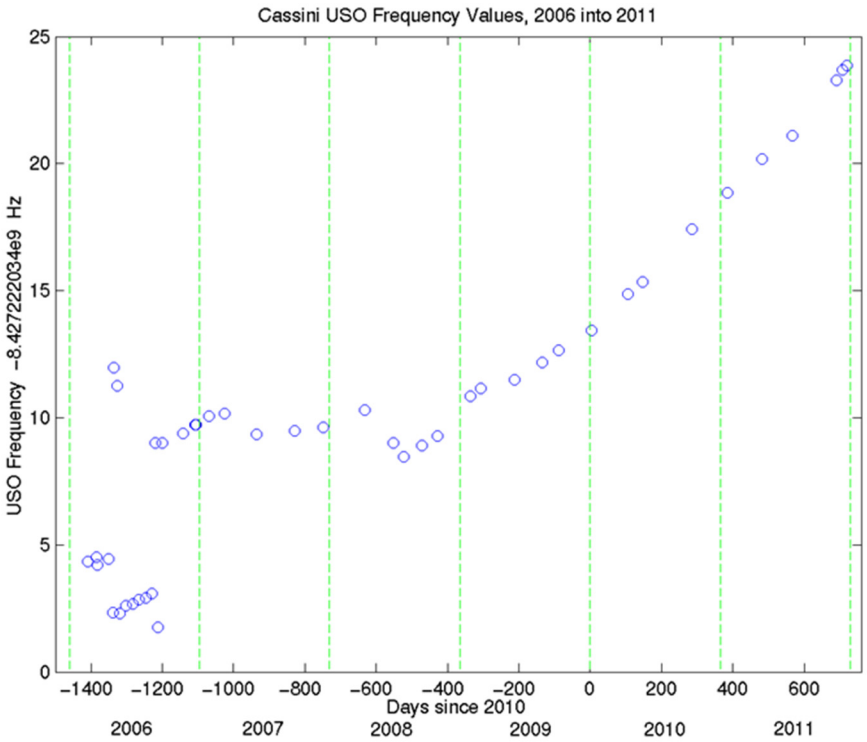

Figure RSS-2. The USO output frequency scaled to X-band by the Cassini transponder over several years, showing long-term aging process as expected.

the end-to-end performance of the radio systems on both the spacecraft and ground station, although independent calibration of the DSN stations have shown that these results are dominated primarily by the limit of the USO performance.

Attitude and Articulation Control Subsystem

The Attitude and Articulation Control Subsystem (AACS) maintains the spacecraft's orientation and consists of redundant Sun sensors mounted on the HGA, redundant stellar reference units mounted on the remote-sensing platform, three mutually perpendicular reaction wheels mounted in the lower equipment module (LEM), plus a fourth backup reaction wheel mounted in the upper equipment module (UEM). Redundant inertial reference units, along with an accelerometer to measure changes in the spacecraft's velocity, are located in the UEM.

The AACS points the selected communication antenna toward Earth and points the remote sensing pallet toward selected targets. It also points one of the two redundant main propulsion engines in the desired direction during engine burns and performs small trajectory correction maneuvers using the onboard thrusters. The AACS uses a pointing system known as inertial vector propagation that keeps track of spacecraft orientation, the direction of the Sun and distance to the Sun, Earth, Saturn, and other possible remote- sensing targets, and the spacecraft-relative pointing

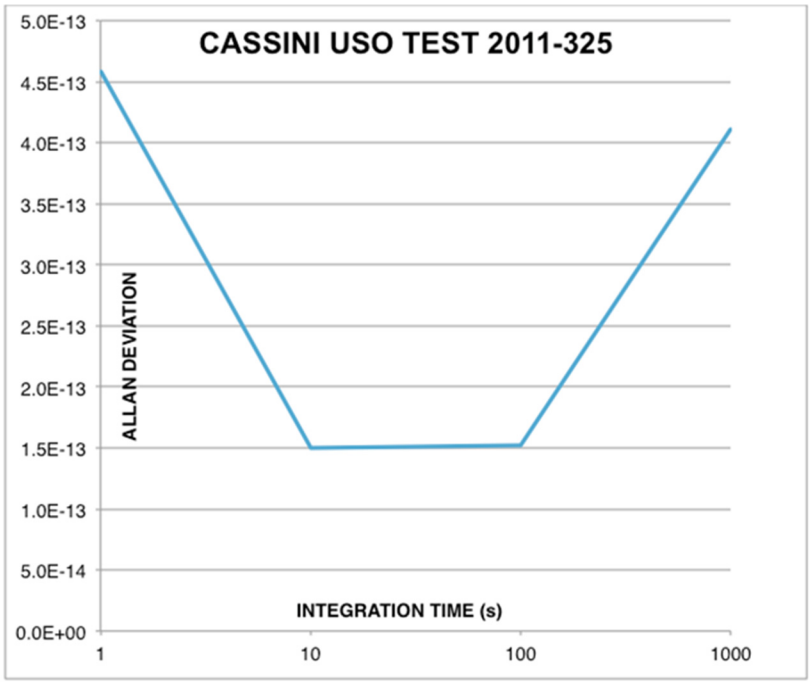

Figure RSS-3. Allan Deviation of the Cassini USO as a function of integration time from a representative test. Four points are plotted at 1, 10, 100, and 1000 seconds.

directions of all science instruments. This subsystem provides sufficient engineering data to support science data interpretation and mission operations.

Other Subsystems

The Propulsion Module Subsystem (PMS) is the largest and most massive subsystem. It consists of a bipropellant element for trajectory changes and a hydrazine element for attitude control, small maneuvers, and reaction wheel desaturation. The Power and Pyrotechnics Subsystem (PPS) converts the radioisotope thermoelectric generator (RTG) power output to provide a regulated 30-V direct-current power bus and provides the capability to turn various users on or off when commanded. Power conditioning equipment can detect over-current conditions and switch the affected user off. The pyrotechnic switching unit also provides redundant power conditioning and energy storage, and it controls the firing of pyrotechnic devices.

The Temperature Control Subsystem (TCS) maintains the temperatures of all critical spacecraft components within their specified limits via electrical temperature sensors. Even at 9 AU from the Sun, spacecraft orientations that expose radiator plates to the Sun can severely degrade the data collected by some of the science instruments. The TCS can turn electric heaters on or off, open or shut thermal louvers in the UEM, use small radioisotope heaters to raise the temperature of selected regions, and utilize thermal blankets and shields. Several instruments have radiator plates for cooling.

Ground Systems

RS data are acquired by the ground instrumentation at DSN stations at Goldstone, California; Canberra, Australia; and Madrid, Spain. During the Grand Finale orbits, additional electrostatic energy analyzer (ESA) ground stations at New Norcia, Australia and Malargue, Argentina, contributed to Cassini RSS experiments. The microwave signals are captured using 34 m or 70 m diameter antennas and are mixed to lower frequencies where they are sampled, averaged, and recorded for later analysis. Two-way and three-way uplink transmissions can be modulated with ranging codes, which allow determination of round-trip times after correlation with the modulation on the downlink signal. Status and performance of the uplink, downlink, and ground antenna systems is recorded in files of monitor data. RS data are acquired via two types of receivers: closed-loop and open-loop.

During the Grand Finale orbits, additional ESA ground stations at New Norcia and Malargue contributed to Cassini RSS experiments.

The ground stations are pointed via the following techniques. Conical scan is dynamical ground antenna pointing during which the boresight is offset from the predicted pointing by a small amount; the observed degradation in signal level is used to determine a new best pointing direction. This is repeated in such a way that the pointing follows a conical path around the best direction; it is not used when the signal is expected to undergo significant amplitude changes. The monopulse technique uses relative amplitude and phase between TE_{11} and TE_{21} circular waveguide mode signals generated in a special Ka-band feed. Aberration correction is a pointing adjustment to account for real motion of the signal source against the sky background during the one-way light travel time. During uplink, the antenna is pointed to the location where the spacecraft will be at the time the signal arrives rather than toward its geometric location at the time of transmission.

Closed-loop tracking receiver

In order to track a spacecraft signal carrier, the closed-loop receiver utilizes a phase-locked loop (PLL) that precisely measures and record the carrier's phase. The Doppler shift is estimated from the phase and converted to relative velocity. Separately, ranging code modulation is extracted and correlated with the uplink code to determine absolute range. The closed-loop tracking receiver provides a Doppler estimate every 0.1 seconds; ranging samples are generated at a rate that depends on the code repetition period and user-selected averaging interval. The tracking receiver also provides a signal to the antenna pointing process.

Open-loop radio science receiver

In open-loop reception, an independent broadband receiver is used without the PLL tracking mechanism described above. The radio science receiver (RSR) down-converts the spacecraft signal via a local oscillator heterodyne process guided by a prediction of the expected frequency.

Additional description of the RSR structure and data format and content is available in the DSN document 820-013, module 0159-Science; a functional description in Asmar et al. [2013]. It captures and records the predetection radio signal at a user-selected sampling rate via an analog-to-digital converter. The digital samples of the propagating electromagnetic wave are stored to disk. Because the received downlink signal can be precisely reconstructed, this mode of data acquisition provides great flexibility in signal processing. The RSR provides superior phase stability, captures the signal during high amplitude or frequency dynamics (where the closed-loop receiver would lose lock), is resilient to multipath effects, and preserves all the information contained in the signal. On the other hand, this method requires additional operational procedures, resources, and generation of predictions sometimes containing complex planetary atmospheric or other models. It also involves handling large file sizes and requires expertise in digital signal processing.

Each DSN complex has at least three RSRs, each capable of independently capturing the output from a different antenna feed, i.e., a different band polarization combination. Similar receivers are also available for very-long-baseline interferometry (VLBI) work; their output can be easily converted to the RSR format, and they can be used when Cassini RS observations require more support than the RSRs alone can provide. The Radio Science Systems Group (RSSG) remotely operates the RSR and VLBI Science Receiver (VSR) from Jet Propulsion Laboratory (JPL).

Key Objectives for RSS Instrument

The key RSS ring science objectives are listed below and discussed in further detail in the section entitled Science Results.

Titan Science

Gravity

Gravity provides unique and crucial information about the interior structure of Titan. When combined with other measurements, such as altimetry and rotation, gravity measurements enable a full tomography of the body. The high-level science questions addressed by the gravity science investigation include:

1. Is Titan in hydrostatic equilibrium?
2. How differentiated is the interior? Is Titan as differentiated as its Jovian cousin Ganymede?
3. What is the density of the core? What is its chemical composition?
4. Is Titan hosting an ocean at depth? If a subsurface ocean exists, what is its density (therefore, its enrichment with salts)?

5. What is the gravitational shape of the moon, and how does it compare with the physical shape?

6. If a higher degree gravity field is measurable, can gravity-topography correlations constrain the thickness of the outer ice shell?

Prior to Cassini, only the density of the moon was sufficiently well determined from Pioneer 11 and Voyager 1 and 2 radiometric measurements [Null et al. 1981; Campbell and Anderson 1989]. Although uncertainties and ambiguities are unavoidable, RSS has been able to answer directly or in combination with other instruments to all these questions, providing a comprehensive picture of the interior structure of the moon.

Atmosphere

The key objectives for Titan atmospheric science were to determine the surface-to-stratospheric thermal structure over a range of latitudes and seasons on Titan, from multiple radio occultation experiments; to measure the wavelength-dependent atmospheric extinction; to investigate atmospheric wave activity; to infer zonal wind characteristics; to characterize diurnal, regional, and seasonal variations in atmospheric structure.

Ionosphere

The key objectives for Titan atmospheric science were to determine the surface-to-stratospheric thermal structure over a range of latitudes and seasons on Titan, from multiple radio occultation experiments; to measure the wavelength-dependent atmospheric extinction; to investigate atmospheric wave activity; to infer zonal wind characteristics; to characterize diurnal, regional, and seasonal variations in atmospheric structure.

Surface—bistatic experiments

The Cassini RSS team carried out a number of bistatic experiments near the Brewster angle at Titan to determine reflectivity and dielectric constant estimates at its three radio wavelengths. A particular focus was to determine the dielectric constant of the liquids in the northern seas.

Saturn Science

Gravity

The key objective for Saturn gravity science was to determine measure gravitational mass (GM), the lower order gravitational moments, and the low-order tidal Love numbers to infer Titan's internal mass distribution from multiple gravitational flybys. During the nominal Cassini tour, the pericenters of the petal orbits were too far from the planet to measure the fine structure of the gravity and magnetic field, the only available tools to probe Saturn's interior. The Grand Finale Orbits (GFO)

brilliantly completed the investigation of the Saturnian system by peeking through the upper cloud deck down to the inner recesses of Saturn's core. In addition, the unique geometry of the GFO orbits, with the pericenters between the planet and the ring system, allowed the determination of the mass of the B-ring, a quantity of utmost importance to reveal the age, hence the nature, of the ring system.

Extensive numerical simulations were carried out in the years preceding the GFO to set the science goals for the RSS gravity investigation at Saturn. The team benefitted from the experience gained with the Juno mission, whose main goal was to probe the deep interior of Jupiter using the same observational tools (Doppler and magnetic measurements), although with dedicated and more accurate instrumentation. The science questions addressed by RSS-Gravity were:

1. To what depth is Saturn differentially rotating? How deep are the flows detected by optical imaging of the clouds?

2. What is the allowed range of core masses? What is the abundance of heavy elements in the interior of Saturn?

3. What is the mass of the B-ring? Are Saturn's rings young or did they form together with the planet?

For a review of the pre-Cassini understanding of the interior of Saturn and the expected improvements from gravity measurements, see Fortney et al. [2016], with earlier references therein. For the relation between the mass and the age of the rings, see Cuzzi and Estrada [1998]. The gravity harmonics of Saturn before the GFO were determined by Jacobson et al. [2006] from the orbital perturbations on the orbits of Saturn's moons.

Atmosphere

The key objectives for Saturn atmospheric science were to determine the surface-to-stratospheric thermal structure over a range of latitudes and seasons on Saturn, from multiple radio occultation experiments; to measure the wavelength-dependent atmospheric extinction; to investigate atmospheric wave activity; to infer zonal wind characteristics; to characterize diurnal, regional, and seasonal variations in atmospheric structure; to help constrain the H/He ratio in Saturn's atmosphere.

Ionosphere

The key objectives for Saturn ionospheric science were to determine the surface-to-stratospheric thermal structure over a range of latitudes and seasons on Saturn, from multiple radio occultation experiments; to measure the wavelength-dependent atmospheric extinction; to investigate atmospheric wave activity; to infer zonal wind characteristics; to characterize diurnal, regional, and seasonal variations in atmospheric structure; to help constrain the H/He ratio in Saturn's atmosphere.

Enceladus Science

Gravity

Enceladus was a special focus of interdisciplinary science in the Cassini mission. Indeed, two major objectives of the Cassini Satellite Surface Working Group were to acquire optical remote sensing observations of Enceladus and to measure its gravity field. This interest is explained by the intriguing characteristics of Enceladus, among which figure the remarkably high and uniform albedo and the presence of old and recent terrains. In the pre-Cassini era, the mean geometric albedo was known to be close to unity, and the total range of albedo over the surface is 20%. This was even more intriguing considering that Enceladus topography contains both old cratered terrains dating from the period of heavy bombardment and smooth terrains recently resurfaced, indicating endogenic activity. Buratti [1998] investigated the photometric properties of Enceladus and concluded that the satellite is completely covered by a young, bright surface layer. Buratti argues that the E-ring, whose thickness peaks at the orbit of Enceladus, is the most likely source for this layer, and that the E-ring itself is probably the result of active surface processes on Enceladus. Alternatively, the bright surface of Enceladus may result from dissipation associated with tidal interactions, perhaps with Dione.

This interest is explained by the intriguing characteristics of Enceladus, among which figure the remarkably high and uniform albedo and the presence of old and recent terrains.

Enceladus' mean radius was known to be ~250 km. How could such a small satellite have undergone substantial evolution? This may be due to the fact that ammonia ice, which plays an important role in lowering the melting point, may have been incorporated into Enceladus. Evidently, the surface properties alone are insufficient to provide information on the interior composition. To understand the nature and history of Enceladus and the other Saturn's satellites, modeling of the interiors and of the thermal evolutions was in order.

As far as Enceladus is concerned, even the most basic parameter, i.e., the mass density, was very poorly known (with about 50% accuracy). A determination of the mass of Enceladus and of its harmonic coefficients of at least degree 2 from data acquired during targeted flybys was deemed a crucial goal to determine its moment of inertia, and hence to constrain models of internal structure.

Atmosphere/ionosphere

The tenuous atmosphere/ionosphere of Enceladus was probed during a serendipitous RSS occultation.

Icy Satellite Science

The objective was to determine the masses (and, where possible, the gravity field) of the icy satellites (especially Dione, Hyperion, Iapetus, Phoebe, and Rhea) in order to determine their mean density to high accuracy, and hence constrain their bulk composition. For Dione and Rhea, which had multiple flybys with radio tracking during the closest approach, the goal was to find out whether these bodies are differentiated and to compare their internal structure to that of Titan and Enceladus.

The mass determination is essential for an improved understanding of their dynamical behavior and evolution. Tyler et al. [1981] determined the masses of Titan and Rhea from Voyager 1 Radio Science measurements at Saturn, and Voyager 2 permitted Tyler et al. [1982] to determine the masses of Tethys and Iapetus. Using the mass of Tethys in combination with the theory of the Tethys-Mimas resonance, they derived the mass of Mimas. Campbell and Anderson [1989] used the combined data set of Pioneer and Voyager data to redetermine the masses of Tethys, Rhea, Titan and Iapetus, but recommended the earlier ground-based determination [Kozai 1957] for Tethys. No mission, before Cassini, yielded a direct determination of the masses of Mimas, Enceladus, Dione, Hyperion, and Phoebe. Phoebe, on an inclined, retrograde orbit, may be a captured object. Determining its density is important to find out whether or not Phoebe is asteroidal in nature.

Ring Science

The primary objective of Cassini Radio Science Subsystem ring experiments was to take advantage of the capability of simultaneous observations at three wavelengths (0.94, 3.6, and 13 cm, or Ka-band, X-band, and S-band, respectively) over multiple occultation opportunities at large, intermediate, and small ring opening angle *B*, to investigate ring structure and physical properties, including:

- High-resolution profiling of radial ring structure and characterization of its variability with wavelength, longitude, ring opening angle, and time. Profiling of the relative abundance of millimeter to decimeter radius particles and characterizing of their variability across resolved ring features.
- Determination of the full particle size distribution over the approximate size range 1 mm to 20 m of broad ring features that can be resolved in the spectra of the near-forward scattered signal. Determination of the vertical ring structure, of the physical ring thickness, and of the particle packing fraction within such features.
- Determination of ring surface mass density, ring viscosity, and bulk density of particle material. Characterization of the variability of these parameters among global ring features (A, B, C …) and within local broad features.

Goals of studies of ring kinematics and dynamics included:

- Determination of the geometry of the Saturn ring system, including determination of Saturn's pole direction and precession rate and a highly accurate (few hundred meter) absolute radius scale of the rings.
- Investigations of ring morphology: A major goal of ring dynamics studies is to explain the presence of non-axisymmetric features such as eccentric ringlets and density waves, and nonequatorial features such as inclined ringlets and bending waves.
- Exploration of ring evolution by characterizing and modeling viscous stresses, and the transport of angular momentum and energy within the rings and their transfer between rings and satellites.

Cruise Science

During the long Cassini phase, RS observations included GWEs near solar oppositions and SCEs. In a GWE, subtle changes in the apparent Earth-spacecraft distance and/or relative velocity, which cannot be attributed to other causes, would indicate passage of gravitational wavefronts through space between Earth and Cassini. GWE observations were conducted in two-way mode for highest clock stability. When the spacecraft's radio signal is occulted by the Sun, then an SCE investigates the solar corona. Operationally, two-way data are collected at large solar radii; but one-way operation with open-loop reception is the practical choice for small solar radii and high solar activity. The shortest radio wavelengths are least affected by the solar plasma; multiple wavelength measurements yield total electron content along the radio path directly.

RSS Science Assessment

Table RSS-2 contains an assessment of RSS ring science based on the objectives in the original Announcement of Opportunity (AO) and the Cassini Traceability Matrix (TM) developed for the Equinox and Solstice missions. Each RSS ring science objective is paired with an AO and TM science objective, with the exception of the Solar Conjunction Experiment (a test of general relativity).

Table RSS-2. Matrix of RSS Science Objectives. Green indicates that RSS data with sufficient quality were obtained during the Cassini mission to contribute to a given science objective.

RSS Science Objectives	AO and TM Science Objectives	RSS Science Assessment	Comments if yellow (partially fulfilled)
Titan Science			
Titan Meteorology	T_AO3, TN2a, TN2c		
Titan Surface and Internal Structure	T_AO4		
Titan Upper Atmosphere	T_AO5		
Titan's Great Seas	TC1a		

Table RSS-2. Matrix of RSS Science Objectives. Green indicates that RSS data with sufficient quality were obtained during the Cassini mission to contribute to a given science objective.

RSS Science Objectives	AO and TM Science Objectives	RSS Science Assessment	Comments if yellow (partially fulfilled)
Titan's Global Seasons	TC1b		
Titan's Interior Ocean	TN1b		
Titan's Internal Structure	TN2b		
Titan's Ionosphere	MC2a		
Saturn Science			
Saturn Temperature	S_AO1		
Saturn Winds and Weather	S_AO2		
Saturn interior structure and rotation	S_AO3, SN1a		
Saturn ionosphere/magnetosphere interaction	S_AO4		
Seasonal variations	SC1a		
Saturn's winds	SC1b		
Ionosphere and ring coupling	MN2a		
Enceladus Science			
Enceladus ocean	IN1a		
Enceladus plume variability	MC1a		
Icy Satellite Science			
Icy satellite interior properties	I_AO4,IN2c		
Ring Science			
Ring structure and dynamics	R_AO1, RC1a, RC1b		
Ring particle size	R_AO2		
Ring-Satellite interaction	R_AO3		
Ring/Ionosphere interactions	R_AO5, MN2a		
F-ring	RC2a		
Ring age and Origin	RN1a		
Ring structure at high resolution	RN1c		
Ring microstructure	RN2a		
Cruise Science			
Gravitational wave experiment	C_AO3		
Solar conjunction experiment			
Solar wind experiment	C_AO2		

RSS Saturn System Science Results

Titan Science

Gravity

Titan played a special role in Cassini: it was at the same time one of the main science targets of the mission, and at the same time its true engine. Titan gravity was used to change the orbital elements of the spacecraft, enabling its complex and extraordinary tour of the Saturnian system. But Titan's gravity, in its fine details, revealed the interior structure of the moon by answering the Key Objectives for RSS Instrument-Titan Science-Gravity. Indeed, lacking an internal dynamo and in the absence of a detectable induction magnetic field, gravity and rotation are the only available tools to peek through the surface and reach the deep interior.

Cassini's observations have unveiled a variety of features and phenomena not found on any other solar system satellite, such as hydrocarbon lakes, river channels, and dune fields, making it a unique object.

Cassini's observations have unveiled a variety of features and phenomena not found on any other solar system satellite, such as hydrocarbon lakes, river channels, and dune fields, making it a unique object. While exogenic processes driven by the dense, hydrocarbon-rich atmosphere, play a crucial role in shaping the complex topography determined by Cassini's radar, contributions from endogenic processes are far less clear. Assessing the presence of active endogenic processes and understanding the origin of the complex topography revealed by Cassini's radar requires the knowledge of Titan's interior structure, which can be indirectly inferred from gravity and rotation data.

Prior to Cassini measurements, models of Titan's interior generally envisaged a core made up of silicates, surrounded by a layer of high-pressure ice, possibly a liquid water or water-ammonia ocean, and an ice-I outer shell, with variations associated with the dehydration state of the core or the presence of mixed rock-ice layers. It was generally expected that Titan could be significantly differentiated [Sohl et al. 2003], although models with higher moment of inertia factor (MOIF) and partial differentiation were also proposed [Fortes et al. 2007]. The determination of Titan's MOIF became therefore a crucial goal for RSS gravity investigations. The MOIF can be inferred from the quadrupole field under the assumption of hydrostatic equilibrium, a hypothesis that Cassini could easily test from the measurement of the J2/C22 ratio (equal to 10/3 for a relaxed body).

Models of Titan's interior envisaging small amounts of ammonia indicated that a subsurface ocean made up of liquid water could exist to the present day—for example, Tobie et al. [2005]. Such a liquid layer has profound implications for the geologic history of Titan and the source of methane. However, one can construct a fully frozen Titan by including only water and rock/metal as bulk

materials, excluding ammonia, and assuming that the crust contains little methane clathrate which acts to lower the thermal conductivity and plasticity of Titan's upper thermal lid [Tobie et al. 2006].

The first hint for a conductive layer came from the analysis of the electric signal acquired during the descent of the Huygens probe in January 2005 [Béghin et al. 2012]. The Huygens Atmospheric Structure Instrument and Permittivity, Wave, and Altimetry (HASI–PWA) observed an electromagnetic (EM) signal at around 36 Hz interpreted as the second harmonic of a Schumann resonance. This physical characteristics of the resonating cavity required a conductive layer at a depth of 65-km (±15-km) that was interpreted as the upper layer of a salty ocean. The measurement of a large obliquity from SAR processing of crossovers was also interpreted as an indication of an outer icy shell decoupled from the interior [Lorenz et al. 2008; Bills and Nimmo 2008].

A conclusive test for the presence of an interior ocean requires the measurement of Titan's time-variable gravity. Therefore, direct testing for the presence of an ocean within Titan's interior became a key goal of the Cassini-Huygens mission. The large eccentricity (e = 0.03) of Titan's orbit causes significant variations in the tidal field from Saturn and induces periodic stresses in the satellite body at the orbital period (about 16 days). Peak-to-peak variations of the tidal field (from pericenter to apocenter) are about 18%. If Titan hosts a liquid layer, the gravity field would exhibit significant periodic variations, controlled by the tidal Love numbers, defined for each spherical harmonic as the ratio between the perturbed and perturbing potential. For Titan the largest effect is by far on the quadrupole field, and the corresponding Love number is indicated by k_2 (assumed to be identical for all degree 2 harmonics).

Analysis of Titan's tidal response [Rappaport et al. 2008] shows that k_2 depends crucially on the presence or absence of an internal ocean. k_2 was found to vary from about 0.03 for a purely rocky interior to 0.48 for a rigid rocky core surrounded by an ocean and a thin (20 km) ice shell. Larger values of k_2, such as 0.7–0.8, are possible if the density of the ocean and the external shell is large (1.1–1.2 g/cm^3). A large k_2 entails changes in the satellite's quadrupole coefficients by a few percent, enough to be detected by accurate range rate measurements of the Cassini spacecraft.

CASSINI FLYBYS OF TITAN

Due to competition with other science goals, the opportunities for gravitational measurements were limited. Titan's main deviations from spherical symmetry are caused by centrifugal and tidal forces, associated respectively with the rotation about its spin axis and the gradient of Saturn's gravity. During the Cassini mission, 10 Titan flybys were committed to gravitational measurements. Table RSS-3 tabulates characteristics of the flybys. The flyby identification is shown in the first column. The color codes identifying each flyby in the table are used also in Figure RSS-4 and Figure RSS-5. The second column indicates the epoch of closest approach (C/A). The gravity signal is stronger for lower pericenter altitudes (third column) while Doppler noise due to interplanetary plasma turbulence decrease for larger Sun-Earth-Probe (SEP) angles (fourth column). T110 was carried out using Cassini's LGA, as the attitude was set by the needs of other instruments. The first four flybys provided the static gravity field and the moment of inertia factor of

Table RSS-3. Main characteristics of Titan's gravity flybys.

Flyby	Closest Approach (C/A) Date	Altitude	SEP
T011	27-FEB-2006 08:25:18 ET	1812 km	150°
T022	28-DEC-2006 10:05:21 ET	1297 km	131°
T033	29-JUN-2007 17:00:51 ET	1933 km	46°
T045	31-JUL-2008 02:14:16 ET	1614 km	30°
T068	20-MAY-2010 03:25:26 ET	1397 km	120°
T074	18-FEB-2011 16:05:17 ET	3651 km	131°
T089	17-FEB-2013 01:57:42 ET	1978 km	106°
T099	06-MAR-2014 16:27:53 ET	1500 km	111°
T110	16-MAR-2015 14:30:55 ET	2274 km	109°
T122	10-AUG-2016 08:32:00 ET	1698 km	113°

the body [Iess et al. 2010]. Two additional flybys (T68 and T74) were needed to ensure a robust determination of k_2 [Iess et al. 2012].

During gravity flybys the spacecraft was tracked from the antennas of NASA's DSN using microwave links at X-band and Ka-band frequencies (8.4 and 32.5 GHz), referred to a common uplink. The state-of-the-art instrumentation enables range rate measurements accurate to 20–50 micron/s at integration times of 60 s.

In order to obtain the optimal gravity measurements, the goal would be to obtain even global sampling of Titan's gravity; however, orbital limitations and competition with other Cassini goals prevented this. Figure RSS-4 shows ground tracks achieved within the limited observational opportunities and emphasizes the scarcity of high latitudinal sampling.

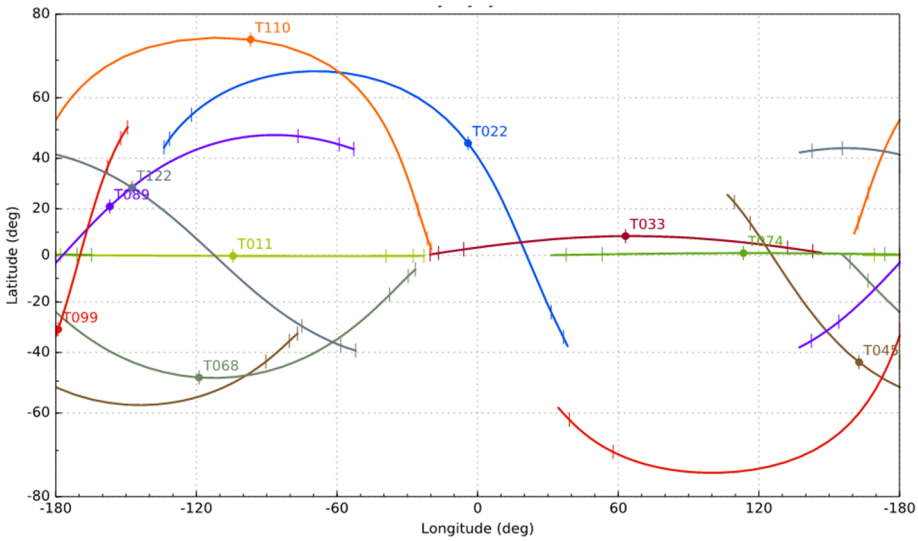

Figure RSS-4. Ground tracks of the 10 Titan gravity flybys showing uneven sampling of the moon's gravity. Each track corresponds to a time window of 3-hours centered at C/A, with tick marks for 30-minute intervals. Lack of coverage on high latitude regions produce larger uncertainties in the reconstructed geoid on those regions.

Figure RSS-5 shows the distribution of the mean anomalies among the 10 flybys. With Titan's orbital eccentricity being about one-half that of our moon at 0.0288, this leads to the ratio of the tidal field at apocenter relative to that at pericenter being about 84%, allowing for considerable response.

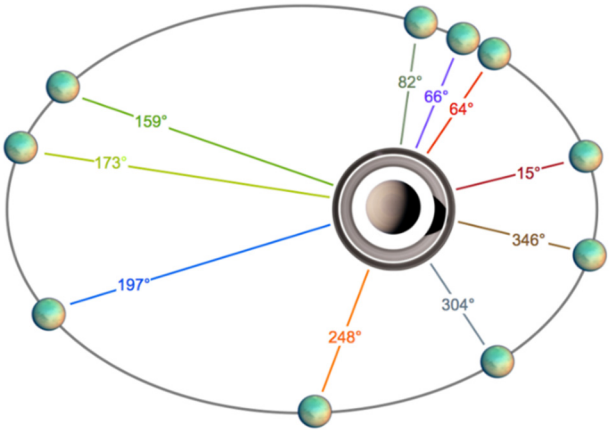

Figure RSS-5. Distribution of Titan mean anomalies of the 10 gravity flybys at the time of closest approach. Measuring Titan's gravity field at different mean anomalies allows a better determination of eccentricity tides (Love number k_2). If the tidal bulge has no phase lag, the tidal variation of the quadrupole gravity coefficients J2 and C22 peaks at pericenter (M = 0°) and apocenter (M = 180°).

Titan Gravity Results

The first four gravity flybys (T11, T22, T33, and T45) provided a determination of Titan's mass and gravity harmonics to degree 3. The quadrupole field was found to be consistent with a hydrostatically relaxed body shaped by tidal and rotational effects. The MOIF inferred from the Radau-Darwin equation is about 0.34, implying incomplete differentiation, either in the sense of imperfect separation of rock from ice or a core in which a large amount of water remains chemically bound in silicates. As has been suggested for Callisto, the proposed incomplete differentiation of Titan may have arisen because of a long accretion time (of order a million years), perhaps because both bodies are at large distance from the parent planet, measured in units of planet radii. The unexpectedly large MOIF has been interpreted in many ways, all ending up in a generally low core density consistent with hydrated silicates.

The equilibrium figure is a triaxial ellipsoid whose semi-axes a, b, and c differ by 410 meters (a–c) and 103 meters (b–c). The nonhydrostatic geoid height variations (up to 19 meters) are small compared to the observed topographic anomalies of hundreds of meters, suggesting a high degree of compensation appropriate to a body that has warm ice at depth. The construction of the geoid and gravity disturbances requires defining a reference ellipsoid. We define the reference ellipsoid as the equipotential surface around the sphere of radius equal to the mean radius of Titan, whose potential is composed of the sum of: (i) the gravitational potential produced by the monopole potential, $J_2^H = (10/3)C_{22}$, and C_{22} ; (ii) the tidal potential due to Saturn; and (iii) the rotational

potential. The equations and the values for the semi-axes of the reference ellipsoid (derived from SOL1 in Iess et al. [2010] are:

$$a = R_t\left[1 + \frac{14}{3}C_{22} + \frac{7}{6}q_r\right] = 2575.239 \text{ km},$$
$$b = R_t\left[1 - \frac{4}{3}C_{22} - \frac{1}{3}q_r\right] = 2574.932 \text{ km},$$
$$c = R_t\left[1 - \frac{10}{3}C_{22} - \frac{5}{6}q_r\right] = 2574.829 \text{ km},$$

for a reference radius R_t = 2575 km. The formal errors are less than 1 m. These values change by about the same amount if SOL2 [Iess et al. 2010] is adopted. A non-hydrostatic reference ellipsoid, constructed from the measured values of J_2 and C_{22}, would differ from the hydrostatic one by at most −9 m for SOL1 and only +0.2 m for SOL2. In both solutions $(a - c)/(b - c) \approx 4$, as expected for a synchronously rotating satellite in hydrostatic equilibrium subjected to the rotational and tidal deformation.

The axes of the reference ellipsoid are larger than the radii found from radar altimetry [Zebker et al. 2009] (a = 2575.15 ±0.02 km, b = 2574.78 ±0.06 km, c = 2574.47 ±0.06 km). The mean planetary radius (2574.73 ±0.09 km) determined by the Cassini radar is slightly smaller than the value of 2575 km adopted in gravity determinations. If this smaller value is used, the axes of the reference ellipsoid become 2574.969 km, 2574.662 km, and 2574.559 km. These values differ respectively by −181 m, −118 m, and +89 m from those determined from radar altimetry, a statistically significant difference especially for the long axis. This interesting discrepancy may stem from several mechanisms. Latitudinal changes of the ice shell thickness resulting from spatial variations of tidal heating [Tobie et al. 2012] and by the subsidence associated with the substitution of methane with ethane-rich liquids percolating into the crust which be composed of methane clathrate hydrates [Choukroun and Sotin 2012].

By combining radio tracking data acquired at different mean anomalies of Titan (see Figure RSS-5) Cassini RSS measurements detected the signature of the periodic stresses [Iess et al. 2012] induced by eccentricity tides. Precise measurements of the acceleration of the Cassini spacecraft during six close flybys between 2006 and 2011 (T11, T22, T33, T45, T68, T74) revealed that Titan responds to the variable tidal field exerted by Saturn with periodic changes of its quadrupole gravity, at about 4% of the static value. Two independent determinations of the corresponding degree 2 Love number yield k_2 = 0.589 ±0.150 and k_2 = 0.637 ±0.224 (2σ). Such a large response to the tidal field requires that Titan's interior is deformable over time scales of the orbital period, in a way that is only consistent with a global ocean at depth. The large value of k_2 points also to an ocean heavily enriched by salts, although the uncertainties are large. The large value of k_2 was confirmed by the yet unpublished analysis of the remaining gravity flybys (T89, T99, T110, T122).

Table RSS-4—from Iess et al. [2012] Table 1 and Table S3 (uncertainties are 2-σ.)—reports the estimated spherical harmonics coefficients for the unnormalized Titan gravity field (degree and

order 4). Eccentricity tides are also included in the model and described by the degree 2 Love number k_2 (last row).

The weak and not so well resolved higher degree gravity (3 × 3 and 4 × 4) was also used to attempt an estimate of the outer shell thickness [Hemingway et al. 2013]. The marked anticorrelation of the 3 × 3 gravity and topography was interpreted as an indication that Titan's ice shell is rigid (elastic thickness >50 km) and that several hundred meters of erosion/deposition have taken place over length scales of ~1000 km, suggesting aeolian transport. However, the gravity topography anti-correlation is much less evident in the latest results. Gravity-topography correlations (Figure RSS-6) were addressed by Mitri et al. [2014], who concluded that a 100 km thick outer ice I shell is underlain by a dense subsurface water ocean containing a high concentration of dissolved salts. The large correlation between the surface topography and the Bouguer anomalies are also consistent the presence of subsurface topographic features under the ice shell. Bouguer anomalies are produced by variations of the ice shell thickness where the surface topography is isostatically compensated. These authors concluded that the ice shell is typically thinner at the poles and thicker in the equatorial and middle latitude regions.

Durante et al. [2019] performed a subsequent analysis of Titan's gravity field and interior structure after Cassini. The results from less et al. [2012] indicated that Titan is subject to large eccentricity tides in response to the time varying perturbing potential exerted by Saturn. The magnitude of the response quadrupole field, expressed in the tidal Love number k_2, was used to infer the existence of an internal ocean. The new gravity field determination provides an improved estimate of k_2 of about 0.62, accurate to a level of a few percent. The value is higher than the simplest models of Titan suggest and the interpretation is unclear; possibilities include a high-density ocean (as high as 1300 kg/m^3), a partially viscous response of the deeper region, or a dynamic contribution to the tidal response. The new solution includes higher degree and order harmonic coefficients (up to 5) and offers an improved map of gravity anomalies. The geoid is poorly correlated with the topography, implying strong compensation. In addition, the updated geoid and its associated uncertainty could be used to refine the gravity-altimetry correlation analysis and for improved interpretation of radar altimetric data.

Table RSS-4. Estimated spherical harmonics coefficients.

	SOL1b Value ±1σ (× 10^6)
J_2	34.227 ±0.477
C_{21}	0.125 ±0.111
S_{21}	0.816 ±0.351
C_{22}	10.263 ±0.069
S_{22}	0.111 ±0.055
J_3	−1.635 ±0.838
C_{31}	0.681 ±0.207
S_{31}	−0.073 ±0.475
C_{32}	0.150 ±0.125
S_{32}	0.104 ±0.114

Table RSS-4. Estimated spherical harmonics coefficients.

	SOL1b Value ±1σ (× 10^6)
C_{33}	−0.221 ±0.016
S_{33}	−0.232 ±0.016
J_4	2.043 ±0.759
C_{41}	0.175 ±0.203
S_{41}	0.033 ±0.250
C_{42}	0.059 ±0.080
S_{42}	0.093 ±0.058
C_{43}	0.026 ±0.015
S_{43}	0.008 ±0.020
C_{44}	−0.007 ±0.002
S_{44}	−0.014 ±0.002
k_2	0.670 ±0.090

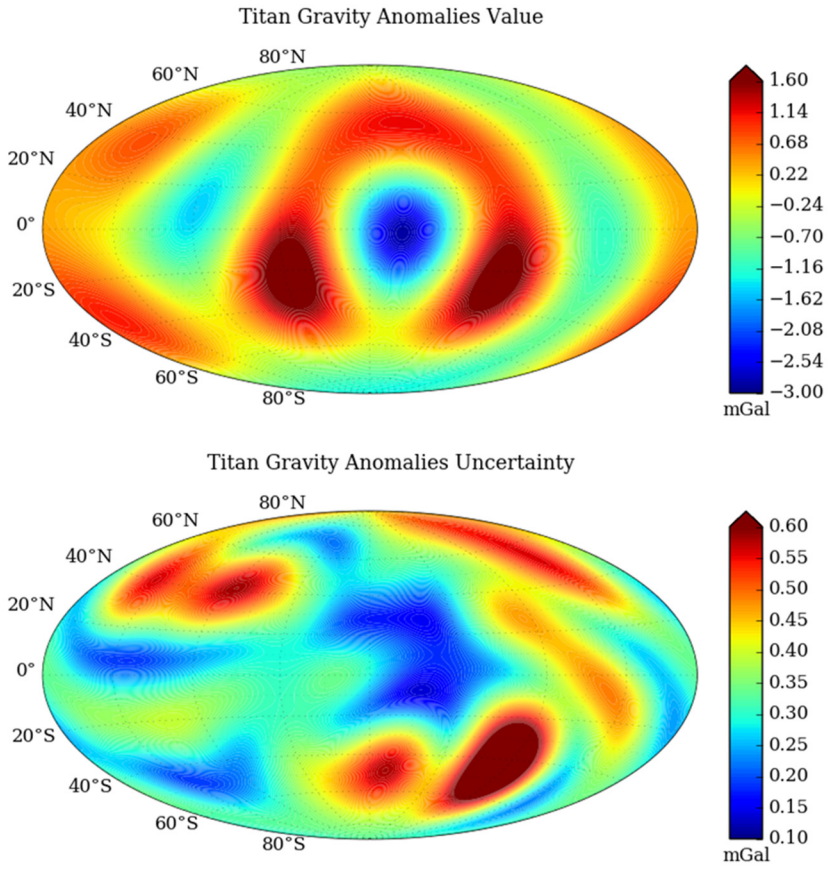

Figure RSS-6. Estimated gravity anomalies (*upper panel*) and related formal uncertainties (*lower panel*) from the analysis of the first six Titan gravity flybys (T11–T74 (4 × 4). The anomalies are computed in mGal over the reference gravity of the ellipsoid defined by the estimated monopole and quadrupole coefficients (GM, J_2, and C_{22}), the tidal field and the rotational state of Titan. Based on the solution SOL1.b from Iess et al. [2012].

Atmosphere

Titan is an interesting object to study, because it is a hybrid combining characteristics of Earth and Venus. Like Earth, its atmosphere is composed mainly of N_2 and it has a hygrological cycle, with methane assuming a role analogous to that of water on Earth. It has seasons, which are determined by the obliquity of Saturn, which is comparable to Earth's. On the other hand, Titan is a slow rotator, and its circulation is cyclostrophic—the winds aloft are globally much larger than the equatorial rotation of its surface, like Venus, but not at all like Earth, where the winds are much smaller than the equatorial surface rotation. Much of what we know about Titan's atmosphere initially came from the Voyager spacecraft flybys in 1980–1981. Although the Voyager soundings were limited, both spatially and in time (early northern spring), the small hemispheric thermal contrasts in Titan's tropospheres suggested that the seasonal response was muted there. In contrast, the large contrasts seen in the upper stratosphere suggested that there were large seasonal swings at those altitudes. A simple calculation of the radiative damping times at different atmospheric levels were consistent with these inferences, the response times being large in the lower atmosphere, and much smaller than the seasonal timescale in the middle atmosphere (stratosphere and mesosphere). The larger meridional temperature contrasts in the stratosphere implied strong zonal winds at these altitudes, especially in the colder northern hemisphere coming out of winter. The implied large seasonal variation expected in the upper stratosphere implied that there would be a large cross-equatorial transport of angular momentum from the northern hemisphere to the southern, as that hemisphere moved into its winter. Thus, there were many meteorological drivers to return to Titan (as Cassini did): first to observe the details of its hygrological cycle near the surface, but also to define better the global spatial structure of the atmosphere and also its seasonal behavior. The last offered a new probe to elucidate the maintenance of cyclostrophic wind systems, which are poorly understood. Titan brings the seasonality card to the analyst's table, which Venus lacks.

The review chapters by Flasar et al. [2014] and Lebonnois et al. [2014] summarize our current understanding of Titan's atmospheric temperature and wind structure, and its seasonal behavior, based in large part on Cassini observations.

There were 20 Cassini radio-occultation soundings of Titan's atmosphere (counting ingress and egress separately). These had relatively high vertical resolution, typically ~1 km through most of the atmosphere, decreasing in the lower troposphere, where differential refraction becomes important, to 10^2 m near the surface. With the failure of the Ultra Stable Oscillator in December 2010, the later occultations were executed in two-way mode. Here, the ground station transmitted a monochromatic signal at X-band to the spacecraft. Upon reception, the electronics onboard multiplied the received X-band signal by 880/749, generated S-band and Ka-band signals from this X-band signal by multiplying by 3/11 and 3.8, respectively, and coherently retransmitted the signal in S-band, X-band, and Ka-band back to Earth. Schinder et al. [2015] describe in detail how the experiment was set up and the received signal record analyzed.

The approach in analyzing radio occultations is to compare the frequency received at the Earth tracking station to what would be expected in the absence of the atmosphere of the target body through which the radio ray passes and is refracted. The difference is the residual frequency.

Knowing the geometry of the occultation, one can derive the bending angle of the ray, i.e., the angle between the incoming ray and that which exits the atmosphere. This can be inverted to retrieve a vertical profile of refractivity—for example, Kliore et al. [2004] and Schinder et al. [2011b]. For Titan, one can assume spherical symmetry in the inversion and use an Abel transform to invert the bending angle profile to retrieve refractivity. Saturn is oblate and the inversions requires ray tracing.

GLOBAL SPATIAL STRUCTURE OF ATMOSPHERIC TEMPERATURES AND ZONAL WINDS

VERTICAL AND MERIDIONAL STRUCTURE

Although the number of soundings were limited, the latitude coverage included high latitudes in both hemispheres, as well as a sampling of low and mid latitudes. Over half the soundings were obtained in northern late winter and early spring. Away from the surface, the troposphere showed little variation with latitude, consistent with the large radiative damping time. In the lowest few kilometers above the surface, variations on the order of a few kelvin appeared. In the northern winter and equinox seasons, variations were small in the summer hemisphere, and the largest variations were seen at high northern latitudes. Near the surface (at the base of the retrieved profiles), the temperature at 80° N was approximately 4 K cooler than at low southern latitudes. The tropopause region, near 40–50 km altitude, exhibited larger variations: high northern latitudes were 4 K cooler than temperatures at 30° S, for example, and even at high southern latitudes in late summer, tropopause temperatures were 2 K cooler [Schinder et al. 2012; Flasar et al. 2014].

Larger meridional contrasts were observed at higher altitudes, consistent with the decrease in radiative damping time. Again, during the northern winter-early spring season the largest contrasts were observed between low latitudes and high northern latitudes, up to 70 K between 100 km and 130 km altitude.

TRANSITION BETWEEN TROPOSPHERE AND STRATOSPHERE

The largest meridional thermal contrasts were observed in the winter/early spring hemisphere at high latitudes, where stratospheric temperatures were much colder than at other latitudes. However, the vertical structure of the transition between the tropopause region and the middle stratosphere—the transition between radiative damping times large compared to seasonal time scales and small damping times—was dramatic [Schinder et al. 2012]. At most latitudes, away from the winter polar region, temperatures above the tropopause region exhibited a rapid increase with altitude from 60 to 130 km, with the vertical gradient gradually becoming smaller at high altitudes. At the high northern latitudes in winter, the usual increase of stratospheric temperatures with altitude, abruptly changed at 80 km, with temperatures decreasing between 80 km and 100 km (by 10 K in the profile at 80° N). The effect decreases at lower latitudes in the winter hemisphere: near 50° N, the decrease has fallen to 1 K. At higher altitudes temperatures resume their increase with altitude, but offset from what one might have expected from the behavior of the temperate profile below 80 km in comparison with profiles observed at lower latitudes. In a manner of speaking, the temperature profiles have abruptly offset from lower

altitudes where there is little meridional (and seasonal) variation to higher altitudes, where these variations become larger. The temperature lapse rate in the transition is statically stable (subadiabatic). What causes it remains speculative, but a radiative origin might be a good guess. Composite Infrared Spectrometer (CIRS) spectra have suggested that organic condensates can form in the lower stratosphere at high latitudes in winter. They also indicate that these latitudes are rich in trace organic compounds that can act as effective radiative coolants. Possibly the increase in infrared opacity at these altitudes can affect the observed destabilization.

One of the most interesting results of the Huygens Doppler Wind Experiment was the minimum at 80 km in the vertical profile of the zonal wind at 10° S, which dipped to just a few meters per second. An analysis of the radio-occultation soundings, composited from 2006 to 2009 and based on the assumption of balanced flow, which relates the zonal winds to meridional gradients in geopotential heights along isobars, indicated that this minimum is global, i.e., it occurs over all latitudes. This is the same altitude, just described, for the abrupt destabilization in the temperature profiles, but only at high latitudes in the winter season. Whether this is coincidental remains to be determined. Possible sources could be damping by interaction of the mean flow with internal gravity waves, but a quantitative analysis remains to be done.

SURFACE TEMPERATURES AND PLANETARY BOUNDARY LAYER

LATITUDE DISTRIBUTION OF SURFACE TEMPERATURES

Because of the weak solar heating and the thickness of Titan's atmosphere (surface pressure ≈ 1.4 bar) the difference between surface temperature and that a few meters higher is expected to be small, so the contrasts discussed above likely hold for the surface itself.

Radio occultations have provided the only means from the Cassini orbiter to map temperatures in the lowest 1½ scale heights of Titan's atmosphere … .

VERTICAL STRUCTURE NEAR THE SURFACE

Radio occultations have provided the only means from the Cassini orbiter to map temperatures in the lowest 1½ scale heights of Titan's atmosphere [Kliore et al. 2004; Schinder et al. 2011b, 2012]. In the earlier part of the mission, when northern hemisphere was in winter and early spring, the occultation profiles had lapse rates in the lowest few kilometers that were close to adiabatic at in the southern hemisphere and at low latitudes in the northern hemisphere. Near 30° S the temperatures lay right on dry adiabats in the lowest 2 km, suggesting efficient vertical mixing from thermal convection. However, the dawn terminator profiles exhibit a more stable structure below the adiabatic layer within 200 m of the surface. This is reminiscent of the nocturnal inversions on Earth, where the surface cools more quickly than the overlying atmosphere during the night, and the atmosphere radiatively cools to the surface and forms a stable layer. However, radiative cooling on Titan is too inefficient to form such a layer over diurnal time scales (16 days), but a turbulent transport with a modest eddy diffusivity ~0.1 m^2/s would suffice.

At high latitudes in the winter hemisphere, temperature profiles become noticeably more stable at the lowest 5 km, being nearly isothermal in the lowest kilometer [Schinder et al. 2012]. Again, this probably reflects cooling to the surface, but over seasonal time scales. In this case, radiative cooling could affect the stable inversion, although turbulent diffusion could also play a role.

Seasonal behavior of temperatures and winds

Radio-occultation soundings near 65° N and S in 2014 and later, as the northern hemisphere moved toward the summer solstice and the southern toward winter, validated the inference of seasonal variation based on the observed meridional structure earlier in the mission. At 65° S the stratosphere above 80 km was rapidly cooling, at a greater rate at higher altitudes [Schinder et al. 2019]. The abrupt transition between 80 and 100 km that was observed at high northern latitudes was not yet evident. At 62° and 66° in the north, the sharp transition seen earlier at high latitudes was decaying, although a remnant persisted. Higher up, the temperatures had not yet attained the larger values seen in the southern hemisphere in late northern winter. Unfortunately, the Cassini tour did not extend a full half year, so a direct comparison that might provide evidence of hemispheric asymmetry is not possible.

Waves

As implied above, absorption of upwardly propagating waves (internal gravity and other types) could effect a drag on the zonal winds in the lower stratosphere, producing the observed minimum in the zonal winds. However, only preliminary analyses of the phase fluctuations (i.e., the small-scale fluctuations in the retrieved temperature profiles) has been done.

Ionosphere

Until the arrival of Cassini, the only direct information concerning the ionosphere of Titan came from the Voyager 1 radio occultation observation. After the careful reanalysis of the original data an electron density peak of about 2.7×10^3 cm^{-3} at an altitude near 1190 km for a solar zenith angle of 90° was found [Bird et al. 1997]. Now we have quite an extended collection of data about Titan's ionosphere from radio occultation, the Langmuir probe, and the ion-neutral mass spectrometer.

The first set of radio occultation observations by Cassini were published in 2009 [Kliore et al. 2008]. This paper presented eight electron density profiles. Figure RSS-7 shows the average of these profiles, along with the Voyager 1 and early Cassini Langmuir probe observations along with a 3-D magneto-hydrodynamic (MHD) model results. A fairly general agreement was found in that there was a density peak in the range of about $2–4 \times 10^3$ cm^{-3} at an altitude near 1200 km. There is a shoulder in the observed densities around a 100 km, which is very likely due to photoionization by soft X-rays. Both the entry and exit T31 results indicated a statistically significant secondary electron density peak near 500 km. Theoretical modeling by Cravens et al. [2008] indicate that ion

precipitation is quite possibly the source of this, somewhat intermittent, secondary peak. Further occultation results were presented in a subsequent paper [Kliore et al. 2011]. This paper presented data from 13 observations obtained by that time (overall only five more profiles were obtained during the lifetime of Cassini and these results were also submitted to the PDF and were similar to previous and published results). The peak electron densities of three of the observed electron density profiles were found to be significantly greater than the average of the others. Using the measured Cassini Plasma Spectrometer (CAPS) Electron Spectrometer (ELS) energetic electron spectra it was shown that these higher peak densities are very likely the result of electron impact ionization.

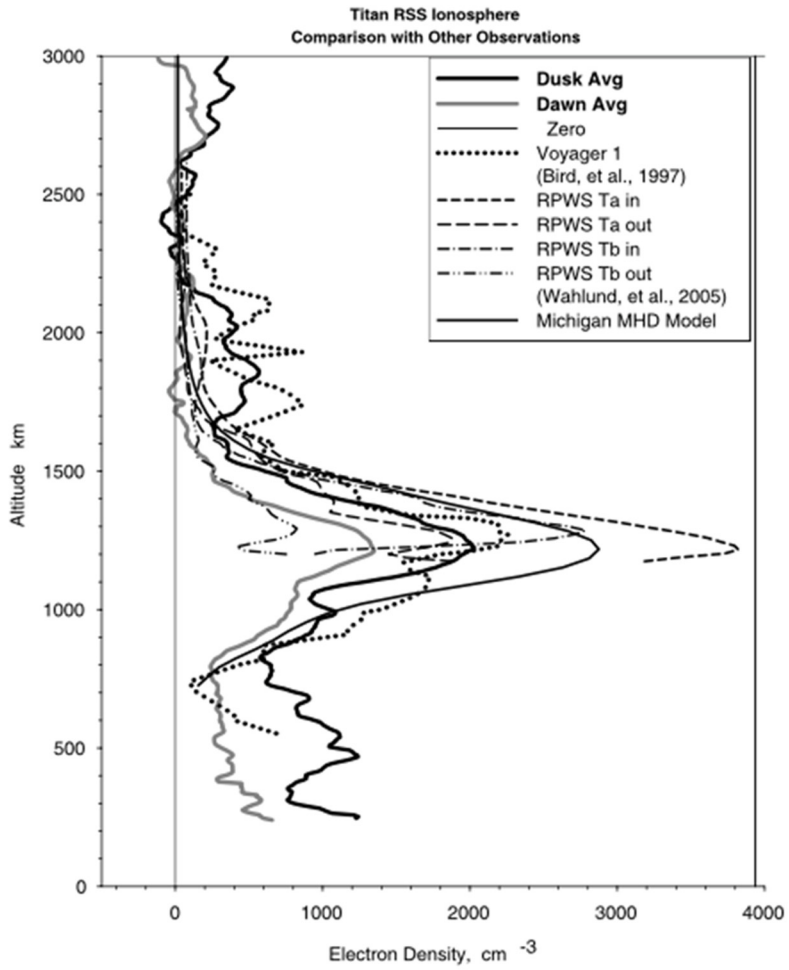

Figure RSS-7. Vertical profiles of electron density from Titan RSS occultations, compared with other observations.

Titan surface scattering results

BSR is the active probing of planetary surfaces by oblique reflection and scattering of microwave signals. Such observations provide statistical information on root-mean-square (rms) surface

slopes and on dielectric constant and density at scales comparable to the radio wavelength (centimeters to meters). An unmodulated radio signal, transmitted from the spacecraft, is scattered by the surface, and the echo is received at a ground station on Earth. A direct signal (from the spacecraft) is often received at the same time, providing a frequency reference for the echo. Fjeldbo [1964] utilized physical optics theory to explain the specular component of the echo as an aggregation of mirror-like reflections from properly oriented elements of the undulating surface. For typical spacecraft transmitters of 1–100 watts, surface echoes as small as 1 zeptowatt (10^{-21} W) can be detected. BSR experiments have been carried out on the Moon, Venus, Mars, and Titan using Soviet, U.S., and European spacecraft [Simpson 2007].

Differential Doppler effects between the direct and reflected paths separates the received echo from the carrier. Dispersion of the echo itself, caused by differential Doppler within the reflecting region, provides a measure of the rms slope of the undulations. Where echo dispersion is not large, the Doppler difference between the two primary paths can be used to infer large-scale topography of the surface. An incident signal with known polarization will generate a reflected signal with both the original and orthogonal components; application of Fresnel reflection theory to absolutely calibrated echoes in one polarization or to relatively calibrated echoes in orthogonal pairs can be used to recover the dielectric constant of the surface material. A simple model relating dielectric constant to porosity then allows estimation of material density.

The first Cassini detectable X-band RS bistatic echoes from Titan's surface were observed on flyby T14 on May 20, 2006 (DOY 140) (Table RSS-5), making Titan the most distant solar system object for which bistatic echoes were successfully detected. The echoes were weak but clearly detectable. Right circularly polarized sinusoidal signal was transmitted by Cassini and both the right and left circularly polarized (RCP and LCP) surface reflected components were observed at the 70 m station of the DSN at Madrid, Spain, Deep Space Station (DSS)-63).

Table RSS-5. Cassini Bistatic Radar Experiments

Start Date	Data Set	Target
2006-03-18	CO-SSA-RSS-1-TBOC1-v1.0	Titan
2006-05-20	CO-SSA-RSS-1-TBOC2-v1.0	Titan
2007-03-25	CO-SSA-RSS-1-TBOC3-v1.0	Titan
2007-07-18	CO-SSA-RSS-1-TBIS1-v1.0	Titan
2008-11-03	CO-SSA-RSS-1-TBOC4-v1.0	Titan
2009-03-27	CO-SSA-RSS-1-TBIS2-v1.0	Titan
2009-04-04	CO-SSA-RSS-1-TBOC5-v1.0	Titan

Cassini was maneuvered continuously to track the region of Titan's surface where mirror- like (quasi-specular) reflected signals may be observed. The ground receivers were tuned to compensate for the large Doppler shift due to relative spacecraft-Titan-Earth motion, allowing detection of the echoes near the center of the recording bandwidth (Figure RSS-8 and Figure RSS-9).

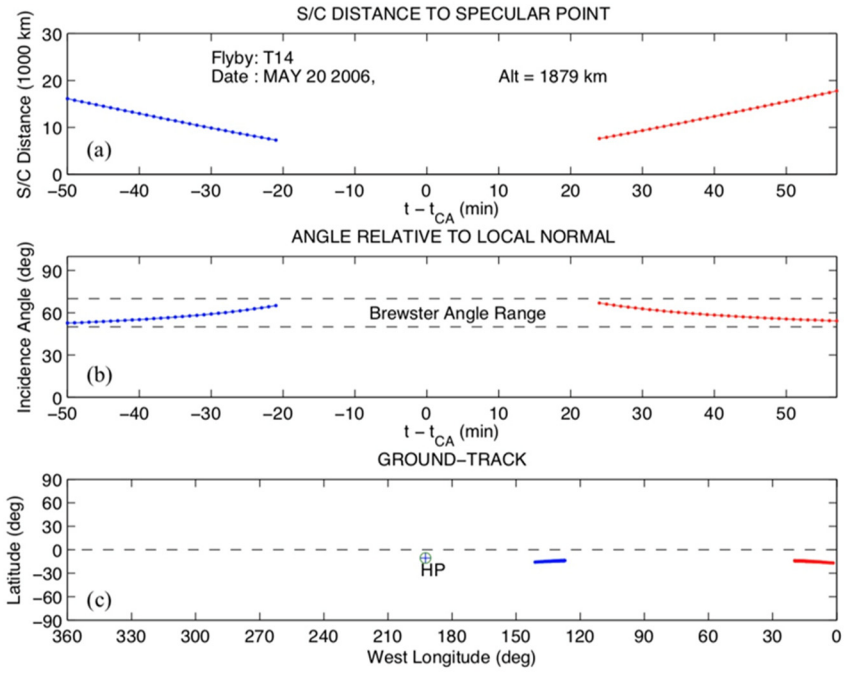

Figure RSS-8. *Panel (a)* and *Panel (b)* depict selected geometry parameters of the Cassini T14 observations and *Panel (c)* depicts the corresponding ground tracks. The Huygens Probe landing site is shown for reference purposes.

The experiment was designed to probe incidence angles θ close to the Brewster, or polarization, angle of likely surface compositions. Careful measurements of the system noise temperature allowed determination of the absolute power in each polarized echo component and, hence, their ratio. The polarization ratio, the known observation geometry, and Fresnel reflectivity were then used to determine the dielectric constant ε.

The T14 surface echoes were detectable on both the inbound and outbound sides, but were intermittent along the ground tracks, suggesting mostly rough terrain occasionally interrupted by patches of relatively flat areas. Polarization ratio measurements were obtained for two localized surface regions of similar latitude ~15° S, well separated longitudes ~14 and ~140° W, and incidence angle θ ~56° and ~64°, respectively. For both regions, the measurements implied surface dielectric constant ε ~1.6, suggesting liquid hydrocarbons, although alternative interpretations are possible [Marouf et al. 2006, 2008].

In Figure RSS-8 panel (a) and panel (b) depict selected geometry parameters of the Cassini T14 bistatic scattering observations. The parameters are plotted versus time relative to closest approach. Inbound (blue) and outbound (red) bistatic observations were implemented before and after the T14 ionospheric/atmospheric occultation (the empty gap in both panels). Panel (c) depicts the corresponding ground tracks. The Huygens Probe landing site is shown for reference purposes. The polarization ratio measurements were obtained for two localized surface regions of similar latitude ~15° S, well separated longitudes ~14 and ~140° W, and incidence angle θ ~56° and ~64°, respectively.

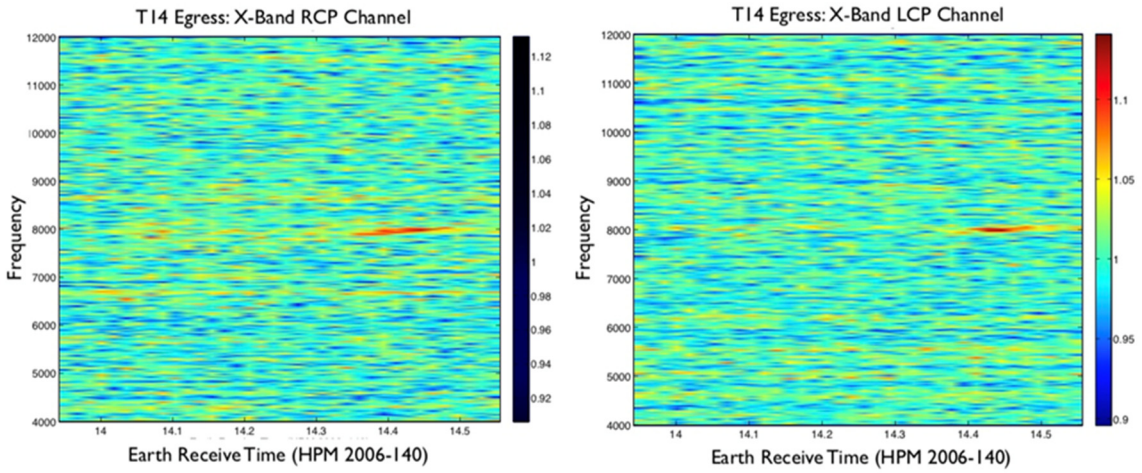

Figure RSS-9. Uncalibrated spectrograms of the first positive detection of bistatic echoes from Titan surface observed on the T14 flyby on May 20, 2006 (DOY 140). The weak echoes were simultaneously detectable in both the RCP and LCP 16 kHz bandwidth X-band channels of the 70 m ground station of the Madrid, Spain DSN complex (DSS-63).

Open questions

Ionosphere

It would be desirable to have more measurements at Titan to enable further examination of the lower ionosphere, which direct measurements cannot probe.

Gravity

The Cassini-Huygens mission provided answers to many key questions on Titan's interior structure. Titan is now a full-fledged member of the Ocean Worlds family, with a low-density core possibly in direct contact with silicates [Castillo and Lunine 2010]. However, major unsolved mysteries remain to understand its interior structure and the exchange processes between the interior, the surface and the atmosphere [Nixon et al. 2018].

The physical mechanism underlying the discrepancy between the gravity equipotential and the global shape is still an open question. The depth of the ocean and the thickness of the outer icy shell remain vaguely determined. Another unsolved mystery is whether the silicate core is in contact with the deep-water ocean, providing an interface similar to the terrestrial seafloor, one of the places where life may have emerged on Earth. Ruling out the existence of a high-pressure ice layer between the core and the ocean would have important consequences for the life-hosting potential of the moon.

Exchange mechanisms between the deep interior and the surface/atmosphere are certainly at play, but Cassini-Huygens has not provided clues on the nature, the extent and timing of these

processes. Whether or not ice convection is taking place in the icy shell is still an unresolved question. No active volcanism has been detected. The presence of methane into Titan's atmosphere requires geologically recent exchange between the interior and the atmosphere, as methane is irreversibly transformed in the atmosphere and its presence requires a supply mechanism. Similar arguments hold for ^{40}Ar, which is found in the atmosphere although its origin is in the decay of ^{40}K contained in the silicates.

Saturn Science

Atmosphere

INTRODUCTION

Saturn's oblateness, a result of its self-gravitation and rapid rotation, is sufficiently large that the usual Abel transform used to analyze spherical atmospheres, cannot be used to retrieve vertical profiles of refractivity from the bending angle ray as it traverses the atmosphere (leading to density, pressure, and temperature). This is particularly true in the troposphere, where refraction of the radio signal as it passes through the atmosphere becomes large. The difficulty emerges because the ray bends toward the local gradient in refractivity (or density in an atmosphere with uniform composition), and not toward the center of the planet, as would be the case with spherical symmetry. This means that the inversions must use ray tracing to retrieve refractivity profiles from the residual Doppler frequency.

Inverting the occultation data requires some assumption of symmetry. The assumption of at least local spherical symmetry is generally used for most atmospheres, but that doesn't work for rapid rotating oblate atmospheres. Here, the assumption used was that the atmosphere was axisymmetric and barotropic, i.e., the mean zonal winds were assumed to only vary with cylindrical radius. In this case, the resulting surfaces of constant density, pressure, temperature, and geopotential height coincide, and the inversion becomes tractable [Schinder et al. 2011a]. Of course, observations from remote-sensing instruments, like CIRS indicate that Saturn's atmosphere is baroclinic, particularly at low latitudes. One can use the occultations to check for consistency and obtain some measure of the error that the assumption of a barotropic atmosphere in the ray tracing introduces.

As with Titan occultations, those of Saturn after December 2010 needed to be done in the two-way mode, described earlier.

There were over 50 occultation soundings from Cassini, spanning low and high latitudes in both hemispheres.

THERMAL AND ZONAL-WIND STRUCTURE

Most of the analysis so far has concentrated on the equatorial region, where there are a large number of soundings within 10 degrees of the equator. The zonal winds can be derived assuming balanced flow, in which the meridional gradient of equipotential height is proportional to the mean zonal wind. A priori, there is no reason why the balanced flow relation does not hold down to the equator, but because the winds are proportional to 1/sin (latitude) in the geostrophic approximation, errors in the geopotential height magnify as one approaches zero latitude. The advantage of radio occultation soundings stems from the ability to refer the retrieved profiles to altitude (or planetary radius). This is possible since a reference body is tracked, namely the virtual image of Earth on the limb. Other remote-sensing instruments, like CIRS, cannot do this, unless they are in an occultation mode, for example tracking a star. In general, they can only obtain a temperature-pressure profile, and must impose a boundary condition, usually at a lower boundary. This becomes complicated in the thermal wind relation, because vertical gradients in the zonal wind must be along cylinders concentric with the rotation axis, rather than truly vertical, as is the case at higher latitudes.

The advantage of radio occultation soundings stems from the ability to refer the retrieved profiles to altitude (or planetary radius).

Retrieving zonal winds from the gradient wind balance first required applying a low-pass filter to the vertical profiles, to avoid small-scale fluctuations, perhaps from waves, from confusing meridional gradients. Then, to allow for the fact that the occultation soundings are not that densely distributed, the meridional distribution was smoothed. The results were encouraging: a vertical oscillation in the zonal winds was observed with a separation of ~2 pressure scale heights between maxima and minima, with peak-to-peak values of ~200 m/s, which is substantial.

SATURN'S SHAPE

Vertical profiles of pressure versus radius were retrieved from all radio occultation soundings, assuming a barotropic atmosphere and winds derived from cloud tracking, as described above. The shape of an isobar depends both on the gravitational potential and the centrifugal potential associated with the atmospheric rotation. The former is calculated using the measured J_n coefficients obtained from two-way radio Doppler tracking. Note that the partitioning between atmospheric winds and any assumed uniform interior rotation is not important, because what the cloud tracking measures are transit times across the visible disk, in other words the total angular rotation of the atmosphere, which determines the centrifugal potential in the atmospheric shell probed by the occultation soundings. With the retrieved profiles at latitudes spanning much of Saturn, the radius of the 1 bar and 1 mbar surfaces were determined as functions of latitude. Were the actual atmosphere barotropic corresponding to the wind model used, then the retrieved pressure surfaces would correspond to that used in the ray tracing. Instead, the retrieved pressures deviated from the model—which used the Voyager winds given by Sanchez-Lavega et al. [2000]—

by ±15 km, which is small compared to Saturn's pressure scale height at these altitudes, ~50 km. Currently the calculation is being redone using the Cassini winds reported by Garcia-Melendo et al. [2011].

Equatorial Oscillation

One of the interesting results from Cassini and ground-based observations is that Jupiter and Saturn exhibit quasi-periodic oscillations in the equatorial stratosphere similar to those observed on Earth. The ground-based observations provided a lengthy time record of several decades, but with limited vertical resolution. Cassini observations provided much more detailed vertical resolution, showing that the equatorial stratosphere consisted of alternating layers of warmer and colder regions. On Saturn, these were two pressure scale heights apart (~100 km). Because of thermal wind balance, these warm and cold anomalies are associated with peak to peak variations in the zonal winds with altitude of ~200 m/s. This structure appears to be zonally symmetric. Cassini observations enabled one to study the temporal evolution of this structure. The equatorial radio occultation soundings, separated by 4–5 years, showed that the pattern descended, but not in a rigid pattern [Schinder et al. 2011a]. This is reminiscent of the situation on Earth, where the oscillation is driven by the absorption of vertically propagating waves with eastward and westward zonal phase velocities.

Waves

Little quantitative analysis of the small-scale structure in the vertical profiles of temperature and pressure has been completed, but it is clearly of interest for studying phenomena like the equatorial oscillation.

NH_3

The extinguishing of the radio occultation signal around 1–2 bar results from a combination of refractive defocusing and absorption by species with large microwave opacities: NH_3, PH_3, etc. This area has yet not received much analysis.

Helium

The tropospheric helium abundance can be determined by using CIRS infrared spectra in the far infrared, using the collision-induced absorption in the translation continuum, and S(0) and S(1) lines of H_2. Helium does not absorb but affects the induced dipole moment of H_2. This analysis can be performed using CIRS spectra alone, but it is consistent with a wide range of helium mole fractions. A more sensitive approach is to combine radio occultations with thermal infrared spectra. For atmospheres with uniform composition, temperatures are proportional to the molecular mass. One can compute synthetic infrared spectra using retrieved occultation temperature profiles for various

assumed masses. The difficulty here is that this approach is that the inferred He mole fraction is smaller than interior modelers predict, which is not easily explained. No obvious systematic errors have been identified in the radio-infrared technique. This work is currently being prepared for publication.

Ionosphere

Until Cassini began to orbit Saturn the only information we had available concerning Saturn's ionosphere came from a handful of decades old radio occultation measurements of electron density profiles by Pioneer 11 and Voyager 1 and 2. Over the lifetime of the Cassini mission over 60 radio occultation observations were carried covering a latitude region from near the equator to 72°.

The results of the early radio occultation observations (12 profiles) were published in 2006 [Nagy et al. 2006]. The resulting electron density profiles all correspond to low latitudes (< 10°) and as all such observations at Saturn were within a few degrees of the terminator as a result of orbital geometry. There were significant orbit to orbit variations observed, an in order to see if noticeable differences existed between dusk and dawn observations averages were obtained as shown in Figure RSS-10. The mean peak densities for the dusk and dawn conditions are about 5.4×10^3

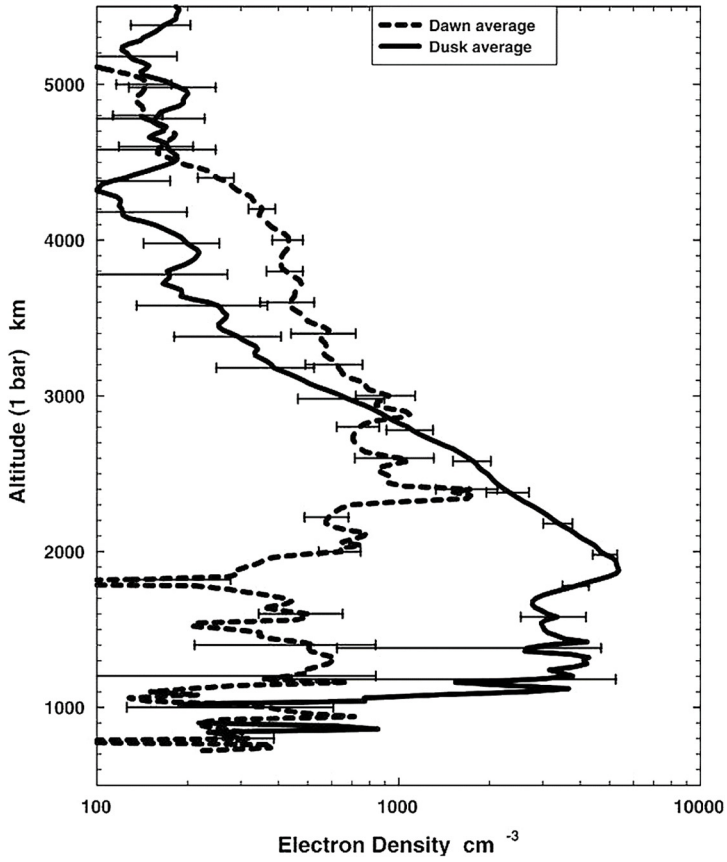

Figure RSS-10. Weighted averages of dusk and dawn electron density profiles.

and 1.7 × 10^3 cm^{-3} and the altitudes of the peaks are at about 1880 and 2360 km, respectively. The measured solar zenith angle for the dusk cases is 95.1 while it is 86 degrees for the observations. The model calculations have indicated that the main ion below and near the peak is H_3^+ and the lifetime of these molecular ions is short, less than a few hundred seconds and thus significant decay is plausible during the five hours of Saturn's nighttime. The decrease in the peak density and the increase in the height of the peak are consistent with such a decay. As the ionosphere decreases at night, it is the bottomside which decreases more rapidly, where the loss rates are higher. This can explain the decrease in the peak density and the rise of the peak height.

The mean observed topside scale heights for the dusk and dawn occultations are about 500 and 1230 km, respectively. It is very dangerous to assume that the topside is in diffusive equilibrium and that temperature gradients are negligible, however at that time there was no information on the plasma temperature and ion composition, thus the scale heights were used to make some estimates on the temperature. Assuming that H^+ is the major topside ion at dawn, the dawn scale height indicates a plasma temperature of about 625°. This value is not inconsistent with the Langmuir probe electron temperature measured during the proximate orbits [Wahlund et al. 2017]. If one assumes that the dusk temperature is at least as large as the dawn one, one arrives at a mean ion mass of about 2.46, which in turn implies the presence of about 72% H_3^+ or 7.7% H_3O^+ or other possible molecular ions; this is also not inconsistent with the Ion and Neutral Mass Spectrometer (INMS) results from the proximal orbits [Waite 2017].

The results of all (except for four, which will be analyzed in the future by Paul Withers, PhD, Boston University) ionospheric radio occultations were published in 2014 [Kliore et al. 2014]. Table RSS-6 shows important aspects of these results, along with numerous relevant parameters. Early indications that the electron densities increase with increasing latitudes was reconfirmed with these more complete results. The original idea to explain this trend was that particle impact ionization increases with latitude and plays a more important role in the total ionization rate [Kliore et al. 2009].

Table RSS-6. Summary of Cassini Radio Science Results on the Saturn Ionosphere.

Orbit ID	Year and Day	Peak Altitude (km)	Peak Electron Density (cm^{-3})	SZA (deg)	Latitude (deg)	L Shell (RS)	EPS Angle (deg)	Ionopause Height (km)	TEC (cm^{-2})	Ring Connection
7N	2005 123	1326.3	6693.5	84.4	−4.9	1.0074	75	6512	8.356E+11	—
7X	2005 123	2472	2215.7	95.9	−9.0	1.0251	75	4808	2.751E+11	—
8N	2005 141	1312	9469.1	85.2	−3.1	1.0029	58	6320	1.013E+12	—
8X	2005 141	1792	1339.4	95.1	−8.3	1.0213	58	5344	2.526E+11	—
9X	2005 159	1168	1688.6	93.8	−7.5	1.0173	41	4728	1.092E+11	—
10N	2005 177	1913.4	7736.1	87.7	1.6	1.0008	25	3640	6.785E+11	—
10X	2005 177	2409.6	1481.3	92.4	−6.1	1.0114	25	5232	3.628E+11	—
11X	2005 196	2528	4287.6	90.8	−4.5	1.0062	8	4096	1.121E+12	—
12N	2005 214	1379.4	10783.9	90.9	7.5	1.0173	9	3144	8.649E+11	—

Table RSS-6. Summary of Cassini Radio Science Results on the Saturn Ionosphere.

Orbit ID	Year and Day	Peak Altitude (km)	Peak Electron Density (cm^{-3})	SZA (deg)	Latitude (deg)	L Shell (RS)	EPS Angle (deg)	Ionopause Height (km)	TEC (cm^{-2})	Ring Connection
12X	2005 214	1326	546.1	89.1	−2.6	1.0021	9	2160	2.993E+11	—
13X	2005 232	2921.9	925.5	87.6	−0.5	1.0001	26	5072	2.131E+11	—
14N	2005 248	1712	12606.9	93.3	−8.4	1.0218	41	3280	7.428E+11	—
28N	2006 260	1360	7965.9	93	−4.3	1.0049	36	3408	1.013E+12	—
44N	2007 130	3032	19028.2	80.4	72.0	10.4721	96	7888	2.806E+12	—
44X	2007 130	1664	757.4	95.5	3.5	1.0037	96	3400	8.343E+10	—
46N	2007 162	2274	11671.2	85.2	−4.1	1.0051	65	7888	4.823E+11	—
47X	2007 179	2637.2	12217.5	94.4	−35.4	1.5050	51	9840	1.964E+12	C
51N	2007 297	2264	2719.8	92.4	−28.4	1.2924	60	6728	9.953E+11	C
51X	2007 297	2916	9466.7	85	−37.9	1.6060	60	9136	1.428E+12	B
54N	2007 353	1456	9615.3	94.3	−14.5	1.0669	114	3160	8.662E+11	—
54X	2007 353	2382	21567.7	85.5	−65.6	5.8598	114	9952	5.073E+12	E
56X	2008 15	2178.4	18436.9	89.6	−68.9	7.7162	141	9920	2.868E+12	E
58X	2008 39	1656	20864.5	89.9	−70.6	9.0636	165	9808	3.573E+12	—
68N	2008 138	1960	8071.5	83.8	23.3	1.1855	101	6552	1.837E+12	D
68X	2008 138	2376	11098.3	90.1	−60.8	4.2016	101	11960	3.037E+12	E
70N	2008 153	2376	2733.5	83.9	37.0	1.5678	86	5144	8.707E+11	B
70X	2008 153	2346.1	10769.6	90.4	−65.1	5.6411	86	10600	1.645E+12	E
72N	2008 168	1672	4803.6	84.2	35.3	1.5013	74	7616	9.005E+11	C
72X	2008 168	2400	14289.4	90.1	−62.9	4.8188	74	9760	2.444E+12	E
73X	2008 175	2472	26192.9	89.9	−61.5	4.3921	67	7328	3.215E+12	E
75N	2008 189	1128	11635.6	85.3	30.0	1.3333	54	9392	1.275E+12	C
75X	2008 189	2184	13083.4	89.5	−57.7	3.5022	54	11336	1.797E+12	E
120N	2009 305	2328	7510.8	93.8	28.5	1.2948	43	5368	1.227E+12	C
120X	2009 305	3216	5140.5	87.6	20.8	1.1443	43	9560	1.391E+12	D
121X	2009 324	2796.1	7090.8	87.1	25.2	1.2214	86	6056	5.138E+11	D
122N	2009 343	2460	5145.2	95.6	41.4	1.7773	80	6648	6.857E+11	B
122X	2009 343	1810.6	16447.2	86.9	29.7	1.3253	80	5488	2.175E+12	C
123X	2009 360	2076.8	4984.6	84.8	1.5	1.0007	96	5256	4.491E+11	—
125N	2010 26	1477.6	5994.6	94.5	−1.4	1.0006	127	8024	2.178E+12	—
125X	2010 26	1888	1540.4	85.5	2.1	1.0013	127	5432	9.119E+11	—
130N	2010 117	1594	10034.2	86.3	17.2	1.0958	145	9920	1.128E+12	—
130X	2010 117	1498.7	24059.9	92.7	12.7	1.0508	145	8344	7.776E+11	—
133N	2020 170	1835.4	6772.3	84.6	−0.4	1.0000	97	4640	5.960E+11	—
133X	2020 170	1309.3	752.3	95.4	0.3	1.0000	96	1464	2.074E+11	—

Table RSS-6. Summary of Cassini Radio Science Results on the Saturn Ionosphere.

Orbit ID	Year and Day	Peak Altitude (km)	Peak Electron Density (cm^{-3})	SZA (deg)	Latitude (deg)	L Shell (RS)	EPS Angle (deg)	Ionopause Height (km)	TEC (cm^{-2})	Ring Connection
135N	2010 205	1685.9	14783.4	86	−13.5	1.0576	64	4856	6.295E+11	—
137N	2010 245	1640	6069.6	87.6	3.8	1.0044	27	4112	6.920E+11	—
151N	2011 213	1624	5571.8	86.5	48.3	2.2597	69	8024	9.328E+11	A
151X	2011 213	2288	6003.3	93.5	40.3	1.7192	69	6176	8.879E+11	B
167N	2012 157	1492.7	7161.7	85.6	4.7	1.0068	133	3888	9.214E+11	—
170N	2012 225	2248	6594.0	89.7	−60.4	4.0987	70	4648	1.803E+12	E
170X	2012 225	1384.9	330.4	95	−1.0	1.0003	70	1896	1.833E+10	—
171N	2012 246	2048	6061.0	88.4	−44.6	1.9725	50	6446	1.546E+12	C. Div.
178X	2013 5	2368	4876.5	89.2	56.1	3.2146	70	6360	2.265E+12	E
180X	2013 31	2344	21488.9	90.4	66.1	6.0924	96	6456	3.774E+12	E
182X	2013 56	2256.8	24509.0	89.5	61.0	4.2546	121	6480	4.526E+12	E
189N	2013 130	2328	10294.0	90.8	−71.9	10.3606	168	6056	2.262E+12	—
190N	2013 140	2584	6246.8	91.3	−70.5	8.9745	159	8552	6.058E+12	—
191N	2013 151	2512	4940.6	93	−44.6	1.9725	149	3640	1.015E+12	C. Div.
191X	2013 151	1314.8	561.1	93.2	−10.2	1.0317	149	1968	2.960E+10	—

An alternate and/or supplemental suggestion was also raised in the 2014 paper [Kliore et al. 2014]. Connerny and Waite [1984] suggested that water inflow from the rings can rapidly convert H^+ into a molecular ion recombines dissociatively and, thus, lead to lower electron densities. The inflow of any other molecule, for example methane, will have the same effect. They called this the ring-rain effect. At that time, there was very little information on the presence of water, but the very little data on the presence and variation of stratospheric water abundances [Bjoraker 2013] was consistent with this suggestion. O'Donoghue et al. [2013] used the W. M. Keck Telescope to observe two bright H_3^+ rotational-vibrational infrared emission lines at Saturn. They reported that their observations was consistent with the so-called ring-rain suggestions of Connerney and Waite [1984]. They detected increased H_3^+ densities where the ionosphere is magnetically connected to the gaps between the rings. An attempt was made to see if this phenomena was noticeable with our ionospheric occultation results. There were only two observations corresponding to the Cassini Division and no noticeable effect was seen. It was somewhat surprising not to see such an effect if it is present, but it is important to note that the two possible opportunities do not provide a statistically meaningful answer.

Gravity

INTRODUCTION

The interior of Saturn is schematically separated into three layers: (i) a helium-depleted, molecular hydrogen envelope, where pressures reach the value of 2 Mbar; (ii) a metallic hydrogen layer, with pressures in the range 2–10 Mbar; and (iii) a heavy element core, with a mass in the range 5–20 Earth masses [Fortney et al. 2016]. Gravity, being determined by the internal distribution of masses, is the primary source of information in the construction of interior models of the planet. Saturn's magnetic field was also expected to provide important additional information, especially on the location of the envelope-metallic hydrogen boundary. If the H-He envelope is fully convective and well mixed, the atmospheric composition may give further constraints, distinct and complementary from those of gravity.

Saturn is a fluid and rapidly rotating planet whose internal mass distribution is largely driven by gravity and centrifugal forces.

Saturn is a fluid and rapidly rotating planet whose internal mass distribution is largely driven by gravity and centrifugal forces. The gravity field is therefore dominated by an axially and hemispherically symmetric component described by even zonal coefficients $J_{2n} \approx q^n$, where q is the ratio of the centrifugal and gravity acceleration at the equator. Deviations from this law are related to two effects: the radial density distribution, and differential rotation associated to flows in the envelope.

Determining the density distribution inside Saturn requires some assumptions on the equation of state (EOS). Due to the lower mass, the dependence of interior models on the assumed EOS is however less critical than for Jupiter. However, models suffer to some extent the uncertainty in rotation rate of the uniformly rotating deep interior.

Dynamical phenomena associated to zonal flows and differential rotation seen in optical images may generate peculiar perturbations in the gravity field. If the differential rotation associated to surface velocity is deep-seated, then internal dynamics affects the gravity field in two ways. Firstly, it perturbs the equipotential surfaces symmetrically, giving rise to a redistribution of mass that appears as a correction to the even zonal coefficients [Hubbard 1999] and a high degree field that does not follow the law $J_{2n} \sim q^n$. Secondly, any north-south asymmetry in the velocity field would necessarily lead to nonzero values for the odd zonal harmonics [Kaspi 2013]. Gravity results from the Juno mission at Jupiter verified these theoretical expectations and were interpreted as an indication of a diffuse core [Wahl et al. 2017] and a wind depth of 2000–3000 km [Iess et al. 2018; Kaspi et al. 2018]. Cassini has repeated these measurements at Saturn, revealing large differences between the two planets.

Another important result of Cassini gravity measurements during the GFO is the determination of the mass of the rings. This quantity, when combined with the percentage of silicate in the ice grains and with the dust flow (both measured by Cassini) can be related to the age of the ring system [Cuzzi and Estrada 1998]. While the masses of the A-ring and C-ring were determined with good accuracy from stellar occultations, the mass of the opaque B-ring remained matter of speculation. Prior to the GFO, Cassini's pericenter was always outside the A-ring, so that the gravitational effects of the rings on the spacecraft motion could not be separated from those of the oblateness of the planet. In the final phase of the mission, Cassini flew between the planet and the rings thus allowing to single out the gravitational pull from the B-ring.

Gravity observations during Cassini's Grand Finale orbits

The range rate of Cassini was the primary observable quantity for gravity determination. Range-rate measurements were obtained from the Doppler shift of a carrier sent from the ground at 7.2 GHz (X-band) and retransmitted back by the onboard transponder at 8.4 GHz. An auxiliary downlink at Ka-band (32.5 GHz) was also available. The nearly edge-on view of the GFO from Earth generated a particularly strong Doppler signature due to Saturn's gravity.

Of the 22 GFO (sequentially labeled as Rev271 through Rev293) six were selected for gravity measurements: Rev273, Rev274, Rev275, Rev278, Rev280, and Rev284. These orbits were chosen to minimize neutral particle drag and tropospheric noise (large spacecraft elevation at closest approach). Unfortunately, data near pericenter for Rev275 could not be used due to a configuration error at the ground station.

Cassini was continuously tracked through pericenter for 24–36 hours from the antennas of the DSN and from the ESA's ESTRACK antennas located in the southern hemisphere (Malargue, Argentina, and New Norcia, Australia). The gravity GFO represented a major coordination effort for the Radio Science group at JPL.

Two-way Doppler measurements at X-band make up 98% of the data. Noise from solar plasma was low due to the large solar elongation angle (> 142° on all six gravity orbits). The data quality was statistically equivalent in X-band and Ka-band data, with an RMS Doppler noise between 0.020 and 0.088 mm/s at 30 s integration time. The main characteristics of the gravity GFO are shown in Table RSS-7 and Figure RSS-11.

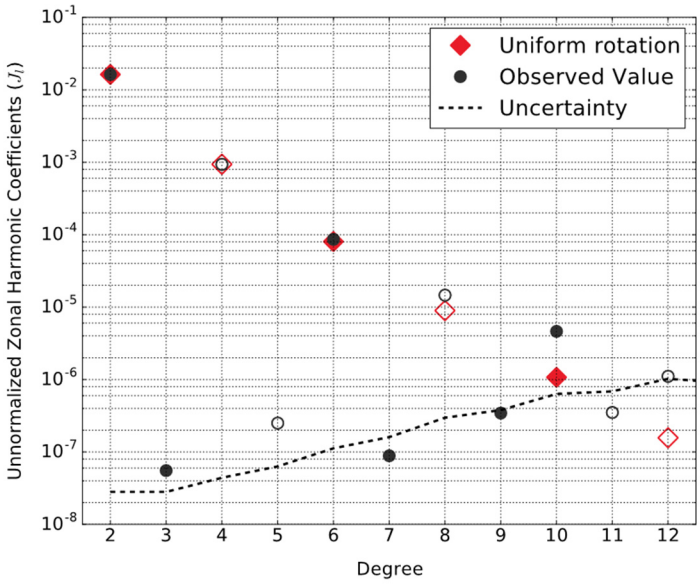

Figure RSS-11. Zonal gravity harmonic coefficients J_2–J_{12}. The dashed line shows the uncertainty from Table RSS-8. Positive values are marked as solid circles, negative values as empty circles. The red diamonds are the theoretical predictions for uniform rotation.

Table RSS-7. Parameters of the osculating orbit at C/A from the RSS reconstructed trajectory. Orbit inclination and C/A latitude are relative to the ring plane. The C/A altitude is relative to the Saturn 1 bar surface (equatorial radius of 60268 km, flattening of 0.09796). The reported noise level refers to the C/A pass only, for Doppler observables at 30 s integration time.

Parameter	Units	Rev273	Rev274	Rev278	Rev280	Rev284
Day (2017)		9 May	15 May	10 June	23 June	19 July
Eccentricity		0.92	0.92	0.92	0.92	0.92
Inclination	(deg)	63	63	62	62	62
EBO	(deg)	96	96	98	99	101
C/A altitude	(km)	2720	2668	3427	3409	2817
C/A latitude	(deg)	−5	−5	−6	−6	−7
SEP	(deg)	142	148	175	172	146
Noise RMS	(μm/s)	29	23	20	88	44

The X-band data were favored for our analysis because of the higher measurements signal to noise ratio (SNR) during ring occultation periods. As predicted, the radio link was lost when the line of sight passed through the densest region of the B-ring, causing a blockage of about 10 minutes. Diffraction and near-forward scattering resulted in a larger Doppler noise at Ka-band than X-band when the beam passed through the rings.

GRAVITY RESULTS

The gravity measurements carried out by Cassini during the Grand Finale orbits reveal a planet with many surprising features. Range rate measurements were successfully used to estimate the zonal field of the planet till degree 10 and the mass of the B-ring, as shown in Table RSS-8. Note: these are preliminary results; for authoritative results, refer to Iess et al. [2019].

Surprisingly, and differently from what was found on Jupiter by Juno, Saturn's gravity shows residual, unexplained, accelerations (at the level of 4×10^{-7} m/s^2) that affected the motion of Cassini and were detected by the Doppler tracking system. These accelerations were absorbed using three different models: stochastic accelerations, acoustic normal modes (zonal component only), and a static tesseral field. As the nature of the unexplained accelerations is unknown at the time of this writing, the stochastic model is preferred. A tesseral field must originate from deep-seated density anomalies in the region of uniform rotation in order to be seen as a static field over the two months of the gravity measurements. This cannot be excluded, although the magnitude of the accelerations and the large degree of the required field (from 8 × 8 to 12 × 12, depending on the assumed rotation period) militates against this hypothesis. In spite of these unexpected features, the solution for the zonal field and the ring mass, relevant for the interpretation, is stable and all parameters are sufficiently well determined.

Table RSS-8. Saturn's gravity harmonic coefficients (unnormalized; reference radius 60330 km) and B-ring mass (in units of Mimas' mass), obtained from the analysis of Cassini's Grand Finale gravity orbits. The uncertainties are 3-sigma for the zonal harmonics and 1-sigma for the B-ring mass.

	Value	Uncertainty
J_2 (× 10^6)	16290.573	0.064
J_3 (× 10^6)	0.059	0.023
J_4 (× 10^6)	−935.314	0.037
J_5 (× 10^6)	−0.224	0.054
J_6 (× 10^6)	86.340	0.087
J_7 (× 10^6)	0.108	0.122
J_8 (× 10^6)	−14.624	0.205
J_9 (× 10^6)	0.369	0.260
J_{10} (× 10^6)	4.672	0.420
J_{11} (× 10^6)	−0.317	0.458
J_{12} (× 10^6)	−0.997	0.672
B ring mass (M_m)	0.23	0.19

The main outcomes of gravity measurements [Iess et al. 2019] can be summarized as follows:

1. The even zonal harmonic coefficients J_6, J_8, J_{10} are so large that only a deep and intense differential rotation can explain their value. The analysis using two different methods (differential rotation on cylinders with the concentric Maclaurin spheroids and differential rotation with finite depth flows from the thermal wind equation) indicate that the flows extend to a depth of ~9000km and must involve a large

fraction of the mass of the planet. This differs from Jupier, where winds are shallower (~3000 km).

2. The favored EOS leads to a core mass in the range 15–18 Earth masses.

3. The mass of the B-ring is not very different from the Voyager-era expectations, pointing to a ring age in the range 10–100 million years. The estimate of the mass under different models for the unexplained accelerations is shown in Table RSS-9. The low value of the ring mass suggests a scenario where the present rings of Saturn are young, probably just 10 million to 100 million years old, to be consistent with their pristine icy composition. Nevertheless, the rings may have evolved substantially since their formation and were perhaps once more massive than they are today. Models for a young ring system invoke the chance capture and tidal disruption of a comet or an icy outer solar system body, suggesting that catastrophic events continued to occur in the solar system long after its formation 4.6 billion years ago.

Table RSS-9. Estimates of the ring masses for the three dynamical models (stochastic, tesseral field, normal modes), in units of Mimas mass (GM_M = 2.5026 km^3/s^2). The uncertainties are 1σ. The solution with the tesseral field shows larger uncertainties due to the large number of free parameters to be estimated. The reference solution (random accelerations) and the solution using normal modes are in good agreement. Although the masses of the three rings are highly correlated, their sum is well determined and consistent at the 1σ level.

	A-ring (M_M)	B-ring (M_M)	C-ring (M_M)	A+B+C-rings (M_M)
A priori	0.11	10.00	0.024	10.00
Random accelerations	0.15 ±0.11	0.23 ±0.20	0.024 ±0.024	0.41 ±0.13
8 × 8 field (10h 32min 45s)	0.14 ±0.11	0.16 ±0.31	0.025 ±0.024	0.32 ±0.27
12 × 12 field (10h 39min 22s)	0.17 ±0.11	0.10 ±0.46	0.024 ±0.024	0.29 ±0.43
10 × 10 field (10h 45min 45s)	0.16 ±0.11	0.43 ±0.37	0.025 ±0.024	0.62 ±0.34
10 × 10 field (10h 47min 06s)	0.17 ±0.11	0.16 ±0.38	0.024 ±0.024	0.35 ±0.35
f-modes	0.10 ±0.11	0.37 ±0.15	0.023 ±0.024	0.49 ±0.07
f- and p- modes	0.13 ±0.11	0.29 ±0.18	0.023 ±0.024	0.45 ±0.12
g- and f- modes	0.10 ±0.11	0.36 ±0.18	0.023 ±0.024	0.48 ±0.13

Open questions

We never got really high latitude occultations of Saturn. Non-radio science efforts includes quite a bit of modeling of Saturn's ionosphere given the proximal orbit observations. The loss of CAPS means that we have no direct information of the ion temperature in Saturn's ionosphere.

What accounts for the tesseral components of Saturn's gravity field?

What accounts for the differences between the overall structure of Saturn's and Jupiter's interior, as revealed by their gravity fields?

Enceladus Science

Gravity

After Titan, Enceladus has been the most observed satellite by the Cassini spacecraft during its exploration of the Saturnian system. Flybys of this small moon revealed a large plume ejected from the south-polar region, with the source being long fractures from which vapor and ice emerge as discrete jets [Spitale and Porco 2007]. Concurrent observations of sodium and potassium salts in the plume [Postberg et al. 2011], and the measured temperatures within the fractures [Spencer et al. 2006], strongly argue for the presence of liquid water in the subsurface source region. The plume exhibits a time variability well correlated to the predicted tidal stresses of the body [Hedman et al. 2013].

The endogenic (non-solar) power emitted from the south-polar region, derived from Cassini CIRS data, is 15.8 gigawatt (GW), with a 20% formal uncertainty [Howett et al. 2011]. This is equivalent to an average surface heat flux of about 20 mW/m^2 and is an order of magnitude larger than conventional estimates of tidal heating if Enceladus' current orbital eccentricity represents a so-called equilibrium resonant state with other satellites [Meyer and Wisdom 2007]. It indicates time-variability in its internal properties [Ojakangas and Stevenson 1986], in a resonant state with other nearby moons [Zhang and Nimmo 2009], or in the rate of heat transport. In any or all of these cases, a plausible internal structure is that of a liquid water ocean overlain by a (thermally conductive) crust [Howett et al. 2011].

Cassini Gravity Flybys and Data Analysis

The design of the Cassini spacecraft did not allow radio tracking from Earth during remote sensing observations. Therefore, only three of the 23 flybys of Enceladus have been used for gravity measurements. In these close encounters the spacecraft was continuously tracked from ground antennas while flying within 100 km of the moon's surface, twice above the southern hemisphere (in the flybys labeled E9 and E19) and once over the northern hemisphere (E12). Enceladus' quadrupole gravity field and degree-3 zonal harmonic coefficient J_3 were determined [Iess et al. 2014] from measurements of spacecraft range-rate. With a radius about 10 times smaller than that of Titan, and about the same density, the gravitational signature of Enceladus in Doppler measurements is much weaker than that of Saturn's largest moon. However, the small perturbation due to J_3 (about 0.2–0.3 mm/s) was still clearly detectable by the Cassini tracking system, whose accuracy was 0.02–0.09 mm/s on a time scale of $\tau \approx 60$ s.

Microwave links between the onboard transponder and ground stations of NASA's DSN enabled precise measurements of the spacecraft range-rate. In addition to gravitational forces, the RSS analysis accounted for the main non-gravitational accelerations, most notably neutral particle drag exerted by the substantial gas plume formed by the jets of the south-polar region. Flying by the moon at latitudes below −70°, the spacecraft interacted with the plume at distances up to 500 km from Enceladus' surface, although most of the effect is localized within 20 seconds from

closest approach. Given the uncertainties in the gas density along the spacecraft flight path, and the short time scale of the interaction, the effect of the drag could be modeled as an unknown, impulsive, vectorial acceleration at closest approach at E9 and E19. The orbital solutions yielded a velocity variation almost parallel to the spacecraft velocity, as expected for a drag force, of magnitude 0.25 mm/s for E9 and 0.26 mm/s for E19, comparable to the J_3 signature. The inclusion of the neutral particle drag in the south-polar flybys is therefore essential for obtaining Doppler residuals free of any signatures, essential for a faithful gravity solution.

As in other Cassini gravity analyses [Iess et al. 2010, 2012; Tortora et al. 2016] the solution for Enceladus' gravity field was obtained from a multi-arc analysis where all data from the three flybys were fitted using separate initial conditions for the spacecraft state vector at each arc (local parameters). The Enceladus state vector, the five degree-2 harmonic coefficients and J_3, were considered global parameters common to all arcs. To avoid biased estimates, the a priori uncertainties on the gravity coefficients were at least 30 times larger than the formal uncertainties obtained from the orbital solution. The non-gravitational accelerations due to anisotropic thermal emission from the three radioisotope thermoelectric generators and solar radiation pressure were modeled using values determined by the spacecraft navigation team from the past eight years of the Saturn tour. By processing the data into a multi-arc least squares filter, all local and global parameters were estimated (Table RSS-10). Furthermore, the solution was proven to be stable with respect to perturbations of the dynamical model, such as the estimation of a full degree-3 field.

The ratio J_2/C_{22} differs from the value required for hydrostatic equilibrium (J_2/C_{22} = 10/3), suggesting that the satellite is not in a fully relaxed shape. The equipotential surface of the tidal, rotational and gravitational potential (the latter limited to 2,0 and 2,2 harmonics) has semiaxis differences of $a–c$ = 6.00 km and $b–c$ = 2.07 km. The tesseral coefficients C_{21}, S_{21}, and S_{22} are null within 3σ, indicating that the adopted rotational model is correct and that the orientation of the principal axes is that expected for a tidally locked body with a fully damped pole. The estimated value of J_3 implies a 2.5 mGal, negative gravity anomaly at the south pole (Figure RSS-12).

Table RSS-10. Solution for the gravity field of Enceladus. Estimated gravity harmonic coefficients from the multi-arc fit of E9, E12, and E19 Doppler data.

Coefficient	Central Value ± 1σ
J_2 (× 10^6)	5435.2 ±34.9
C_{21} (× 10^6)	9.2 ±11.6
S_{21} (× 10^6)	39.8 ±22.4
C_{22} (× 10^6)	1549.8 ±15.6
S_{22} (× 10^6)	22.6 ±7.4
J_3 (× 10^6)	−115.3 ±22.9
J_2/C_{22}	3.51 ±0.05

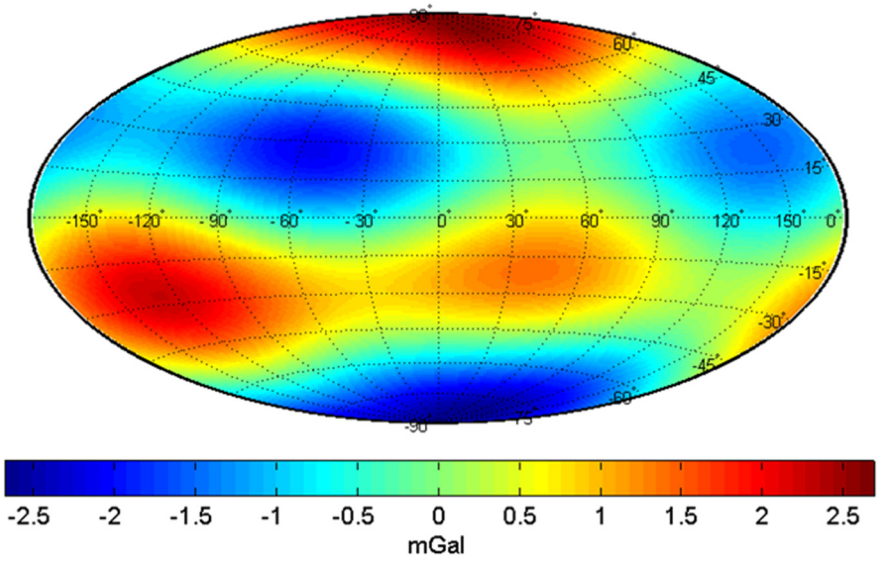

Figure RSS-12. The gravity field due to C_{21}, S_{21}, S_{22}, and J_3 as in Table RSS-10 is mapped onto the reference ellipsoid. The negative anomaly at the south pole, representing the asymmetry between the two hemispheres, is ~2.5 mGal.

INTERIOR MODELS

The interpretation of Enceladus gravity presented a greater difficulty and uncertainty than usual, given the strikingly different appearances of the northern and southern hemisphere, and the apparent confinement of endogenic activity to the high southern latitudes. Still, the deviation of J_2/C_{22} from 10/3 (the value for a laterally homogeneous body) is modest (of order 6%) and the non-degree 2 gravity is small (of order 2% relative to J_2), suggesting that there is some prospect of useful inferences.

The topography of Enceladus [Nimmo et al. 2011] is not that of a relaxed hydrostatic body under the action of tides and rotation in a synchronous orbit. Based on the global shape data which show a topographic depression at the south pole [Thomas et al. 2007], it has long been proposed that the liquid reservoir may be located only in the southern hemisphere [Collins and Goodman 2007], thus explaining why the activity is concentrated around the south pole [Tobie et al. 2008]. First interpretation of the topography and gravity data [Iess et al. 2014; McKinnon 2015] suggests that the ice shell is about 30–40 km thick at the south pole, and its thickness increases to about 60 km in the equatorial region. However, from these data alone, it is not possible to definitively conclude whether the ocean is global or only located in the southern hemisphere. More recently, the detection of a significant physical libration [Thomas et al. 2016] has indicated that the ice shell is mechanically decoupled from the rocky core, thus providing the first direct evidence for a global subsurface ocean. Thomas et al. [2016] have shown that the observed libration is consistent with an average ice shell thickness of 21–26 km, which is significantly less than the value predicted from gravity and topography. Čadek et al. [2016] show that the Cassini observations can be reconciled by considering isostatic compensation including the effect of a few hundred meter thick elastic

lithosphere. Their model predicts that the core radius is 180–185 km, the ocean density is at least 1030 kg/m^3, and the ice shell is 18–22 km thick on average. The ice thicknesses are reduced at poles decreasing to less than 5 km in the south polar region.

Interior modeling of Enceladus remains an active area of research and is important because its internal structure tells us about the thermal state, evolution, and energy budget of this ocean world.

Ionosphere

An unplanned opportunity to observe the Enceladus plume was discovered in a routine search, which indicated that the radio path will pass within a few hundred kilometers from Enceladus' south pole shortly before a scheduled Saturn occultation during orbit 125. The Cassini science engineers were able to adjust the orbit to obtain a plume occultation with the radio path passing about 45 km below the south pole. At the time of the passage of the Cassini radio line-of–sight (LOS) through the center of the plume, its velocity relative to Enceladus was about 13 km s^{-1}, and the distance of Cassini from Enceladus was about 577,400 km. The occultation was observed by two DSN stations near Canberra, Australia: (i) DSS-43 with a 70-m diameter antenna receiving S-band (~13 cm) and X-band (~3.5 cm) signals; and (ii) DSS-34 with a 34-m antenna receiving X-band and Ka-band (~1 cm) signals. The two frequencies from both stations were coherently differenced to obtain frequency data that is sensitive only to the electron plasma.

The differenced frequency residuals were inverted using an Abel integral inversion, cf. Kliore et al. [2004], for the case of circular cylindrical symmetry (with the axis of the cylinder being the north-south polar axis of Enceladus), to obtain the refractivity as a function of distance from the south pole axis, which then can be used to obtain the profiles of electron density shown in Figure RSS-13. This clearly indicates an electron density enhancement with a maximum density of

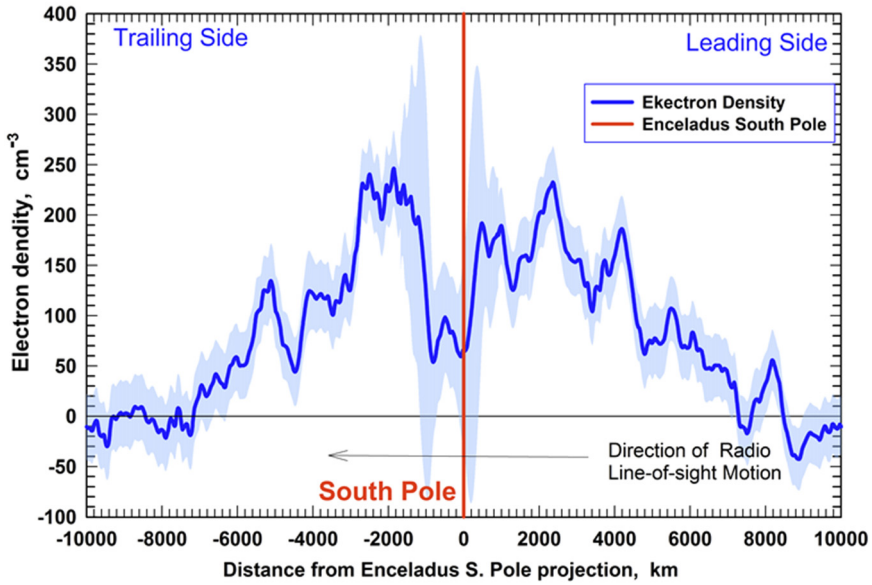

Figure RSS-13. RSS observations of Rev125 Enceladus occultation.

about 225 cm^{-3} on the entry (leading) side, at a distance of about 2000 km from the plume center, and approximately 245 cm^{-3} maximum density on the exit (trailing) side, also at a distance of about 2,000 km from the plume center, extending to about 7,000 km (~28 R_E), in both directions from the plume axis. A significant asymmetric drop in the electron density to about 50 cm^{-3} in the neighborhood of the Enceladus plume, beginning near the plume centerline on the leading side, and continuing for about 1,000 km on the trailing side, can also be seen clearly in the figure. A few smaller dips on both sides are also observable.

The Radio and Plasma Wave Spectrometer (RPWS) in situ observations [Morooka et al. 2011] based on both the Langmuir Probe and the upper hybrid emissions were taken along the E3, E4, E5, and E6 Cassini flybys, which were also close to Enceladus, but basically at right angles to the RSS results. Therefore, no direct comparisons between these data sets can be made, nevertheless, a few comparative statements are possible. The combined data sets indicate significant electron density plumes extending to about 28 R_E in both directions close to the equatorial plane. Both the RPWS and RSS electron density observations indicate a large drop of the density in the immediate vicinity of the Enceladus neutral density plume and smaller fluctuations further out in the wings. These observations are consistent with the direct RPWS measurements in terms of densities, but are in a direction about 72° away, which implies that the extended plasma plume extends in both directions in the equatorial plane. The large electron density bite-out is very likely caused by electron attachment to grains with sizes ranging from nanometers to micron-sized. We also showed by simple calculations that the peak electron densities observed outside this depletion region are consistent with photoionization of neutral gas plus removal by plasma transport.

These results were presented at numerous national and international meetings—for example, Kliore et al. [2006, 2010].

Open questions

What are the long-term spatial and temporal variations in the ionosphere of Enceladus, associated with its plumes originating from the southern hemisphere?

Icy Satellite Science

The determination of the gravity fields of the Saturnian satellites was one of the main scientific goals and responsibilities of the Cassini Radio Science team [Kliore et al. 2004]. Radiometric tracking data were acquired during the flybys of Phoebe, Iapetus, Hyperion, Dione, and Rhea, allowing an accurate determination of the masses of these satellites as well as the gravity quadrupole field of Dione and Rhea [Rappaport et al. 2005; Iess et al. 2005, 2007; Thomas et al. 2007; Mackenzie et al. 2008; Zannoni et al. 2015; Tortora et al. 2016]. These experiments consisted in using X-band and Ka-band coherent, two-way Doppler data and fit them in JPL's Orbit Determination Program in short data arcs. Doppler data were fitted using a spacecraft dynamical model that included the gravitational accelerations from all Saturn system bodies, as well as non-

gravitational accelerations from the spacecraft Radioisotope Thermoelectric Generators and from solar radiation pressure. The noise introduced by the Earth troposphere was calibrated at Goldstone (California) and Madrid (Spain) complexes of the DSN using an Advanced Media Calibration (AMC) system [Resch et al. 2002] at Canberra (Australia) the standard Tracking System Analytical Calibrations (TSAC) is used instead [Bar-Sever et al. 2007], being an AMC not available. AMC devices were specifically developed in support of the cruise Cassini radio science experiments (see the section entitled RSS Non-Saturn Science Results – Cruise Science) and consisted of water vapor radiometers, digital pressure sensors and microwave temperature profilers assembled in a single unit installed a short distance from the DSS-25 and 55 at Goldstone and Madrid, respectively. Since the loss of the Cassini onboard Ka-band transponder in 2003, which in the past allowed a full calibration of the solar and interplanetary plasma [Tortora et al. 2003, 2004], the Sun-Earth-Probe angle also became an important factor in determining the radio link frequency stability [Asmar et al. 2005] and, in turn, the achievable accuracy in the orbit determination and parameter estimation process. Thus, to mitigate the effect of the charged particles in the solar corona, interplanetary space, and the Earth ionosphere X-band uplink, Ka-band downlink (X/Ka) Doppler data were preferred to X/X data, if acquired simultaneously (Ka-band data are more immune to plasma noise); similarly, in order to maximize the phase stability, 2-way data were preferred to 3-way data, if acquired simultaneously.

A close encounter with Phoebe, was performed by Cassini just prior to the Saturn Orbit Insertion (SOI) maneuver, on June 11, 2004.

Phoebe

A close encounter with Phoebe, was performed by Cassini just prior to the Saturn Orbit Insertion (SOI) maneuver, on June 11, 2004. This was the only opportunity during the whole Cassini mission because, after SOI, its maximum distance from Saturn was designed to be smaller than Phoebe's orbital radius. Phoebe's C/A took place at an altitude of about 2000 km and a relative velocity of about 6.4 km/s.

For the determination of Phoebe's GM [Rappaport et al. 2005], X-band Doppler data and optical images of the Saturnian satellites were used. The optical navigation images were used to constrain Phoebe's ephemerides and determine its position relative to the spacecraft, so that the intrinsic correlation (in terms of satellite mass and spacecraft impact parameter) of a hyperbolic flyby could be removed.

Iapetus

Iapetus moves around Saturn on a large orbit of radius ~59 Saturn radii. For the first Cassini encounter (October 17, 2004), the distance at closest approach of Cassini to the satellite was 1.11×10^6 km, so large that the encounter barely deserves the name of flyby. However, Iapetus is a big body with a radius of 733 km, so even a distant encounter allowed to determine its mass. The

large distance at closest approach had a positive effect, in that the determination has only a weak dependence on the impact parameter, and more generally, on the relative orbit of Cassini with respect to Iapetus. Indeed, we expected the correlations between the mass of Iapetus and the orbital elements of both Cassini and Iapetus to be small. The relative velocity between Cassini and Iapetus at closest approach of the first flyby was 3.7 km/s. This relatively small velocity was an advantage since it resulted in a relatively large velocity change of Cassini, due to Iapetus, of about 3.2 cm/s, greater by more than three orders of magnitude than the sensitivity of the radio signal to velocity changes. The SEP angle at C/A was 87°. This implied a solar plasma noise of about 9.2×10^{-14} at 300 s integration time, i.e., larger than the noise introduced by the Earth troposphere [Asmar et al. 2005]. For this reason, the Cassini Radio Science Team requested Ka-band passes to reduce the detrimental effect of plasma noise on Doppler data. For the first Iapetus flyby, the data used for our determination [Iess et al. 2005] consisted of closed-loop tracking data acquired in the period from October 10–25, 2004. The set of data includes Doppler X/X and X/Ka data as well as ranging data at X-band. The Doppler data before and after C/A were compressed at 300 seconds, while those acquired on October 17 and 18 were compressed to 60 seconds.

The second Cassini encounter of Iapetus occurred on December 31, 2004. The distance at C/A of Cassini to the satellite was 123,363 km, the relative velocity was 2.0 km/s and the SEP angle was 165°. As explained in the section entitled Key Objectives for RSS Instrument, this short distance at C/A implied that the uncertainty in the distance at C/A was predominant on the uncertainty in the velocity change so that the estimation (and an update) of the satellite ephemerides was mandatory. The data used for our determination [Iess et al. 2005] consisted of closed-loop tracking data acquired in the period from December 28, 2004 to January 2, 2005. The set of data includes only X-band Doppler coherent with X-band uplink. The Doppler data were compressed at 300 seconds.

Hyperion

The Cassini flyby of Hyperion occurred on September 25–26, 2005. The C/A took place on September 26, 2005, 02:24:47 UTC at a distance of 618 km from the center of mass of the satellite and with a relative velocity between the spacecraft and the moon of about 5.6 km/s. The data used for our determination [Thomas et al. 2007] consisted of closed-loop tracking data acquired in the period from 07:54:07 UTC of September 25 to 21:29:11 UTC of September 26, 2005. The data set was originally designed to comprise four segments of observation: two of them just before and after C/A, acquired over the Goldstone and Madrid complexes, respectively, and two additional passes—the so-called gravity science enhancement (GSE)—to be acquired far from C/A (in the wings of the hyperbolic flyby) about 12 hours before (Madrid) and after (Goldstone) C/A. However, due to a complex-wide failure, all data to be acquired over the Madrid complex on the egress part of the flyby just after C/A were lost, leading to a significant degradation in the GM estimation error. Thus, the exploitable data set consists only of three segments of observation (two before and one after C/A) where the Doppler data are a combination of two-way and three-way, X/X and X/Ka data, predominantly sampled at 60 s.

Dione

During its time in the Saturn system, Cassini has performed five close flybys of Dione, three of which included radio tracking during closest approach: one in December 2011, and two in summer of 2015. As in previous works, the gravity field of Dione was estimated by reconstructing the spacecraft trajectory during these encounters, making use of precise measurements of the Doppler shift of a highly stable microwave radio link between Cassini and the ground station antennas of NASA's DSN.

The available data were analyzed [Zannoni et al. 2015] in a multi-arc fit estimating a fully unconstrained quadrupole gravity field for Dione, the Dione and the spacecraft initial state vectors for each flyby, and modeling parameters for the non-gravitational accelerations. The stability of the solution was tested by perturbing the dynamical model in various ways, including estimating a full 3 × 3 gravity field and changing the a priori uncertainties. The Saturn system dynamics were modeled on the basis of the most recent satellite ephemerides.

Rhea

Before Cassini's arrival in the Saturn system, only the gravitational parameter GM was known from the analysis of Pioneer and Voyager data [Campbell and Anderson 1989]. Using this and the estimated volume (from camera images), a bulk density of about 1200 kg/m^3 was derived, relatively small and compatible with a mixture of about 75% by mass water ice (density 1000 kg/m^3) and 25% rock-metal (density 3000 kg/m^3).

During its mission in the Saturn system, Cassini performed four close encounters of Rhea, of which only two were devoted to gravity investigations. The first gravity flyby, referred to as R1, according to the numbering scheme used by the Cassini project, was performed on November 26, 2005, during the main mission, and the second and last gravity flyby, referred to as R4, was performed on March 9, 2013, during the Solstice mission.

Radiometric data acquired during the first encounter (R1) were used to estimate the gravity field of Rhea. A first estimate [Anderson and Schubert 2007] was obtained under the assumption of hydrostatic equilibrium, i.e., constraining the unnormalized gravity coefficients J_2 and C_{22} to a ratio of 10/3. From this estimation, by applying the Radau-Darwin relation the authors obtained a normalized moment of inertia of about 0.3911 ±0.0045 (a value of 0.4 would imply a constant density interior). The authors concluded that the satellite's interior is a homogeneous, undifferentiated mixture of ice and rock, with possibly some compression of the ice and transition from ice I to ice II at depth.

In parallel, the radiometric data acquired during R1 were independently analyzed by the Cassini Navigation team [MacKenzie et al. 2007] and by the Cassini Radio Science team [Iess et al. 2007]. Both analyses estimated the moon's GM and quadrupole gravity coefficients J_2 and C_{22}, obtaining different solutions, but consistent at the 2σ level, as a result of different analysis approaches. The two approaches were then combined to obtain a joint best unconstrained

estimation of the quadrupole field [MacKenzie et al. 2008]. The solution obtained is not statistically compatible with hydrostatic equilibrium, hence, no useful constraint on Rhea's interior structure could be imposed. Hydrostatic equilibrium was also ruled out by applying this constraint to the estimated quadrupole field coefficients, and this led to a significant degradation of the orbital fit at closest approach. To explain the non-hydrostatic ratio J_2/C_{22}, the authors theorized that a large collision occurred after the completion of the thermal evolution of the satellite, causing a redistribution of mass and a reorientation of the tidal bulge.

Successively, Anderson and Schubert [2010] stated that the differences in the previously published gravity fields are probably caused by a mismodeling of the non-gravitational acceleration acting on Cassini caused by anisotropic thermal emission. To avoid this issue, Anderson and Schubert [2010] restricted the analysis to a subset of data around the closest approach (± 2000 s), where the information from Rhea's quadrupole gravitational field is confined. They obtained a new solution in agreement with Anderson and Schubert [2007] using the hypothesis of hydrostatic equilibrium. Moreover, they concluded that non-hydrostaticity is not supported by the data.

To resolve these discrepancies, a second and final gravity flyby was planned in Cassini's Solstice.

To resolve these discrepancies, a second and final gravity flyby was planned in Cassini's Solstice. R1 was characterized by a very low inclination, about 17° at the closest approach (C/A), in order to decorrelate the estimation of J_2 and C_{22}, while R4 was designed to be nearly polar, with a high inclination at C/A, about 106°. However, the C/A of R4 was about 999 km, twice as high as R1 (about 502 km), thus significantly reducing the information content about Rhea's quadrupole gravity field in this second flyby. The SEP angle was larger than 110° during both encounters, thus range-rate measurements were only slightly affected by the harmful effect of solar plasma.

During the encounters, Doppler data at X-band (8.4 GHz) and Ka-band (32.5 GHz) were acquired by the antennas of NASA's DSN at the three complexes of Goldstone, Madrid, and Canberra. In addition to data obtained around the closest approach, the analysis also used data obtained up to two days before and after the closest approach, during standard navigation tracking passes. The additional data allow an improvement of the orbit determination, in particular, the estimation of Rhea's ephemerides and Rhea's GM, because of the stronger constraints that are imposed on the relative trajectories between Cassini, Rhea, and Saturn.

It is important to note that the closest approach of R1 was tracked only in three-way mode, meaning that the receiving and transmitting stations were different. This represents a suboptimal condition, due to the possible delay between the reference oscillators of the two different uplink and downlink stations. During R4, the closest approach was tracked in two-way mode.

Dual frequency X-band uplink and Ka-band downlink (X/Ka) Doppler data were preferred to the standard X/X data when available, to reduce the effects of the dispersive noise sources, mainly the solar corona and the Earth ionosphere. Two-way Doppler data were preferred to three-way

data in the same band when both were available, to remove the errors due to the clock synchronization between the uplink and downlink ground stations.

When only two-way X/X data and three-way X/Ka data were available, the selection was made on a case-by-case basis.

When available, the wet path delay due to Earth's troposphere was calibrated using measurements from advanced water vapor radiometers [Resch et al. 2002]. When not available, the Earth's troposphere was calibrated using a combination of weather data and dual frequency GPS measurements [Bar-Sever et al. 2007].

The mass estimation results obtained by the Cassini Radio Science team for Phoebe, Iapetus, and Hyperion are summarized in Table RSS-11, along with the rank of each solution (the number of estimated variables) and the tropospheric calibrations used.

The gravity field results obtained by the Cassini Radio Science team are summarized in Table RSS-12 for Rhea.

Table RSS-11. Mass estimation results for the Saturn icy satellites encountered by Cassini.

Saturn Icy Satellite	Estimated GM (km^3/s^s)	Solution Rank	Estimation of Cassini SV	Estimation of Satellite SV	Use of Optical Navigation Images	Tropospheric Calibrations[1]
Phoebe	0.5517 ±0.0007	13	Yes	Yes	Yes[2]	TSAC
Iapetus	120.2064 ±0.0631	7	Yes	No[3]	No	TSAC
Hyperion	0.375 ±0.003	13	Yes	Yes	No	TSAC

[1] AMC = Advanced Media Calibration, TSAC = Tracking System Analytical Calibrations.

[2] The use of optical navigation data for Phoebe's flyby helped constraining the relative distance between the spacecraft and the satellite.

[3] The ODP version used for Iapetus data analysis did not possess the capability to estimate and update the planetary satellite ephemerides as part of the orbit determination procedure.

Table RSS-12. Estimated values and 1-σ formal uncertainties of Rhea's quadrupole gravity unnormalized coefficients for the Cassini Radio Science Team solution [Tortora et al. 2016], compared to the results published in MacKenzie et al. [2008] and Anderson and Schubert [2010]. MacKenzie et al. [2008] did not provide the correlation between J_2 and C_{22}, a zero value was assumed. Anderson and Schubert [2010] solution was obtained by constraining the J_2/C_{22} ratio to the hydrostatic value 10/3. A priori values and uncertainties used by RSS are also shown in the first column.

	Unit	(a priori)	RSS Team	(MacKenzie et al. 2008)	(Anderson and Schubert 2010)
J_2	(× 10^6)	930 ±600	946.0 ±13.9	931.0 ±12.0	892.0 ±1.6
C_{21}	(× 10^6)	0 ±300	−19.9 ±11.0	0 ±0.0	0 ±0.0
S_{21}	(× 10^6)	0 ±300	23.5 ±21.3	0 ±0.0	0 ±0.0
C_{22}	(× 10^6)	240 ±250	242.1 ±4.0	237.2 ±4.5	267.6 ±4.9
S_{22}	(× 10^6)	0 ±250	−15.3 ±5.0	3.8 ±3.8	0 ±0.0
J_2/C_{22}		3.9 ±4.8	3.91 ±0.10	3.92 ±0.9	3.33 ±0.0
corr J_2-C_{22}		0.0	−0.34	0.0 (N/A)	1.00

The results obtained by the Cassini Radio Science team, summarized in Tables RSS-11 and RSS-12, represent a major improvement in the knowledge of the Saturn icy satellite gravitational parameters, with respect to the pre-Cassini published results [Campbell and Anderson 1989; Jacobson 2004]. These more accurate results, along with the satellite geometrical information coming from the Cassini Imaging team, were used by the Cassini Radio Science team to build interior models and allow their geophysical interpretation for some of the encountered icy satellites.

Open questions

- How close to hydrostatic equilibrium are the icy satellites? What does this say about their internal structure and geophysical history?

Ring Science

During a ring occultation observation, Cassini transmits three coherent sinusoidal signals simultaneously through the rings. They are generated from the common onboard USO, allowing measurement of their amplitude, frequency, and phase, as well as their relative phases.

As a transmitted signal passes through the rings, the ring material perturbs it. Two signal components can be identified in the measured spectrum of the perturbed signal. The first is the direct signal, a narrow spectral line that is the remnant of the coherent incident sinusoid after being attenuated and phase shifted by ring material. The time histories of estimated average power and phase change of the direct signal provide a measured extinction and phase shift profile. The extinction is characterized in terms of an optical depth and, with the help of a reconstructed spacecraft trajectory, is used to compute an optical depth versus radius profile of the ring system as a function of wavelength. The initial profile is diffraction-limited. Accurate measurement of the signal phase allows reconstruction of the profile to remove diffraction effects [Marouf et al. 1986].

The second component is the near-forward scattered signal, a frequency-broadened signal that originates from incoherent superposition of the signals scattered by ring particles located within the intersection of the main-lobe of the Cassini high-gain antenna and the rings plane (antenna footprint). The Doppler shift caused by the relative motion of the spacecraft, ring particles, and ground station broadens the spectrum of this signal component. The time history of the scattered signal spectra can be used to determine the size distribution of large (> 1 meter) particles as well as other physical properties [Marouf et al. 1983; Zebker et al. 1985].

RSS ring occultations during the Cassini Prime Mission

Twenty-four one-sided radio occultations of Saturn's rings were observed during the Cassini Prime Mission (Table RSS-13), with additional occultations observed through the Grand Finale orbits. The spacecraft trajectory was chosen so that the path of the radio signals transmitted from Cassini to an observing ground receiving station would be interrupted by the ring system.

The Prime Mission occultation observations sampled a broad range of ring-opening angles, *B*. In particular, a set from Revs 7 to 14 of mostly diametric occultations captured relatively large angles, 19.5–23.5°, allowing detailed profiling of the optically thick ring B for the first time. Another set from Revs 53–67 of mostly chord occultations sampled small ring opening angles ~6-10°. The limited intermediate range of angles, 14–15°, was sampled by occultations from Revs 28, 44, and 46. These 24 occultation cuts also sampled a broad range of ring longitudes both inertial and Earth-relative.

Table RSS-13. RSS Ring Occultations Completed During Cassini Prime Mission.

Occ #	YYYY-DOY[1]	Cassini Rev #	Ingress/Egress/Chord	B (deg)[2]
1	2005-123	7	I	−23.57
2	2005-123	7	E	−23.57
3	2005-141	8	I	−23.17
4	2005-141	8	E	−23.17
5	2005-159	9	E	−22.64
6	2005-177	10	I	−22.01
7	2005-177	10	E	−22.01
8	2005-196	11	E	−21.29
9	2005-214	12	I	−20.54
9	2005-214	12	E	−20.54
11	2005-232	13	E	−19.76
12	2005-248	14	I	−19.12
13a[3]	2006-258	28	I	−14.35
13b[3]	2006-259	28	I	−14.35
14	2007-130	44	E	−15.23
15	2007-162	46	I	−14.37
16	2007-337	53	I	−6.68
17	2007-353	54	C	−6.63
18	2008-015	56	C	−7.04
19	2008-027	57	C	−7.38
20	2008-039	58	C	−7.80
21	2008-062	60	C	−8.65
22	2008-092	63	C	−9.60
23	2008-102	64	C	−9.79
24	2008-130	67	C	−9.91

[1]Observation Year and Day-of-Year.

[2]Ring opening angle.

[3]Ingress occultation was interrupted over Ring B by a high-phase orbiter remote sensing observation.

A gallery of the Earth view of selected RSS occultations is shown in Figure RSS-14, with the spacecraft path shown in blue.

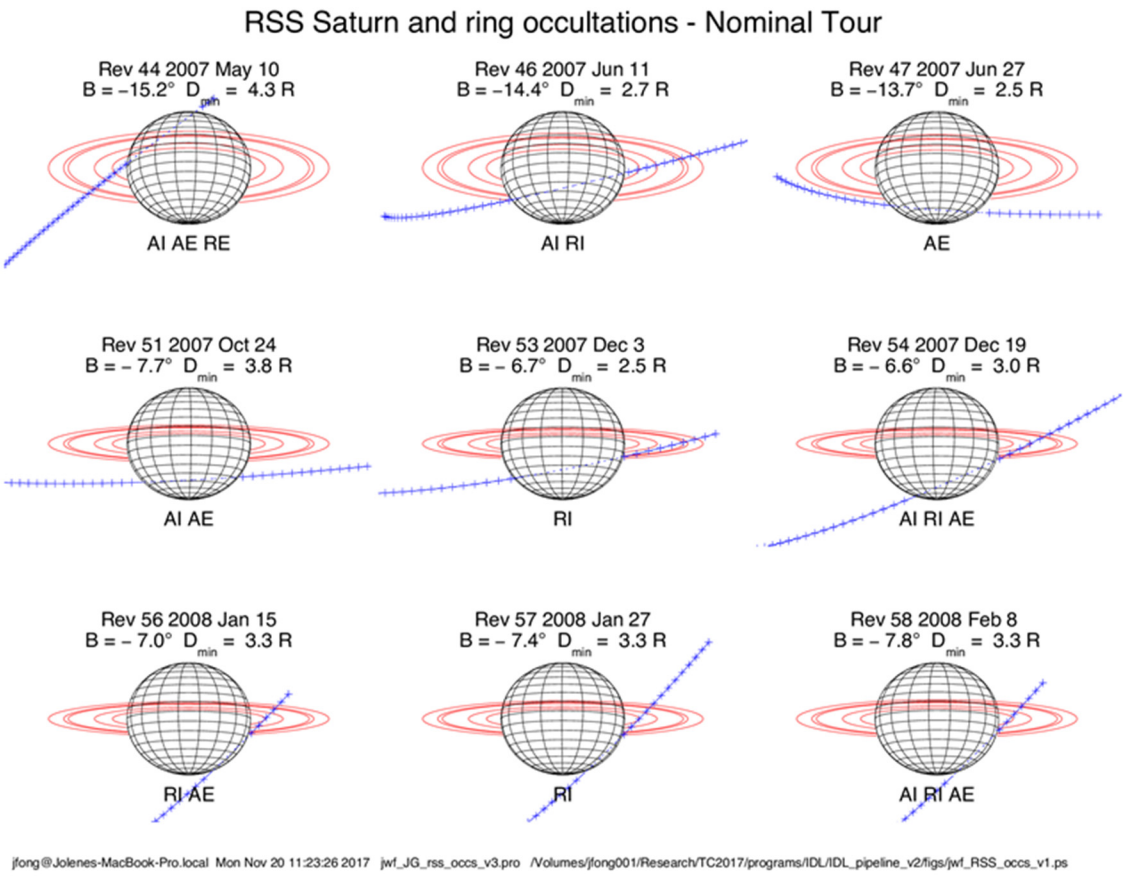

Figure RSS-14. Gallery of Earth-based views of selected RSS ring and atmosphere occultations in 2007 and 2008.

Radial structure in the rings

A major objective of the RSS ring occultation experiments was to determine highly accurate orbits of the rings and to investigate the dynamics and kinematics of ring and gap edges. This work was carried out in collaboration with the Visual and Infrared Imaging Spectrometer (VIMS) and Ultraviolet Imaging Spectrograph (UVIS) teams, in order to combine the full set of occultation data obtained from Cassini instruments. A series of four major papers summarized the results of this joint effort: the edge of Saturn's B-ring [Nicholson et al. 2014a], the C-ring [Nicholson et al. 2014b], the Cassini Division [French et al. 2016], and a determination of the absolute radius scale and pole direction of Saturn [French et al. 2017]. Representative examples of the results from these papers are shown in Figure RSS-15 and Figure RSS-16.

Figure RSS-15 shows the broad influence of Titan's 1:0 inner Lindblad resonance (ILR) over the inner C-ring—from Nicholson et al. [2014b]. Figure RSS-16 shows the structure of the inner C-ring—from Nicholson et al. [2015b]—from the RSS Rev 007 occultation.

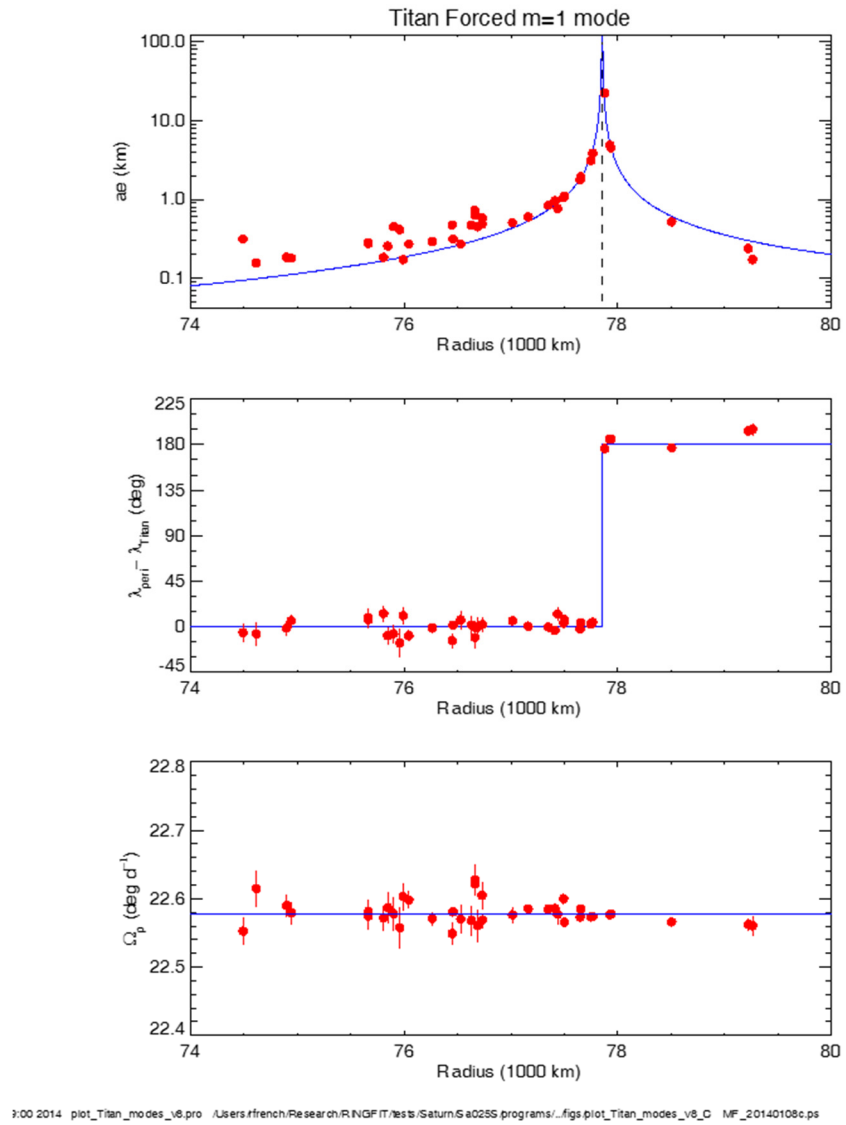

Figure RSS-15. Fitted amplitudes, phases, and pattern speeds versus radius for perturbations induced at a distance by the strong Titan 1:0 ILR. *Upper panel*: curve shows the predicted amplitude, based on a simple test-particle model. *Middle panel*: shows the phase of the perturbation relative to Titan. Note: the orientation changes by 180 from inside to outside the resonant radius, in accord with the same model. *Lower panel*: shows the best-fitting pattern speed compared to Titan's mean motion of 22:577 deg/day. Figure from Nicholson et al. [2014b].

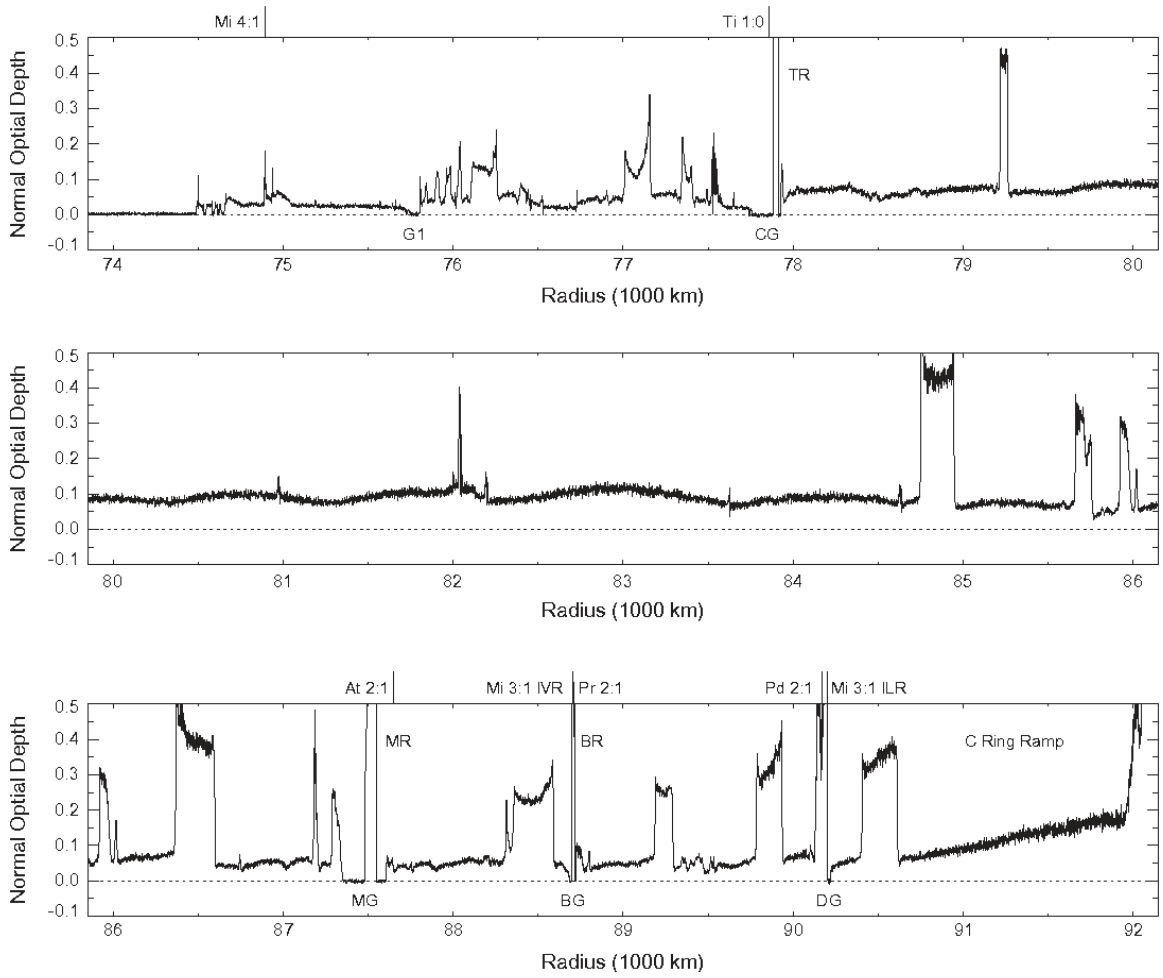

Figure RSS-16. An optical depth profile of the C-ring, derived from the Cassini radio occultation on Rev 7. Abbreviations refer to the Titan ringlet (TR) and Colombo gap (CG), the Maxwell gap and ringlet (MG, MR), the Bond gap and ringlet (BG, BR), and Dawes gap (DG). Tick marks across the top of the plot indicate the locations of significant satellite resonances with Ti = Titan, Mi = Mimas, At = Atlas, Pr = Prometheus, and Pd = Pandora.

From nearly edge-on occultation observations of the C-ring later in the mission, RSS measurements revealed a conspicuous periodic beating pattern between two km-scale waves (Figure RSS-17). From spectral measurements of the power spectrum of the waves and direct model fits, the observations can be interpreted as 10-meter scale vertical corrugations in the C-ring with horizontal wavelengths of order 1 km, increasingly tightly wound as one approaches Saturn (Figure RSS-18). This hints at the possibility that two ancient impacts in the 1300s tilted Saturn's rings—detailed analysis remains to be completed for this provocative possibility.

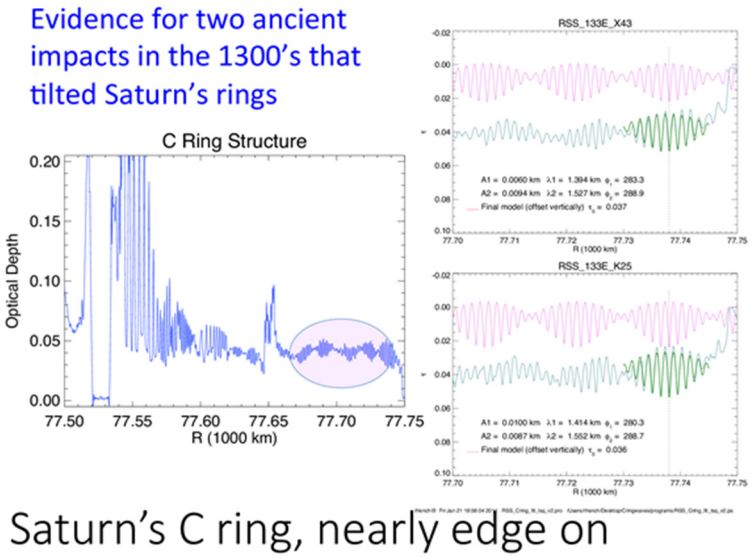

Figure RSS-17. Optical depth profile of the inner C-ring from a nearly edge-on RSS ring occultation.

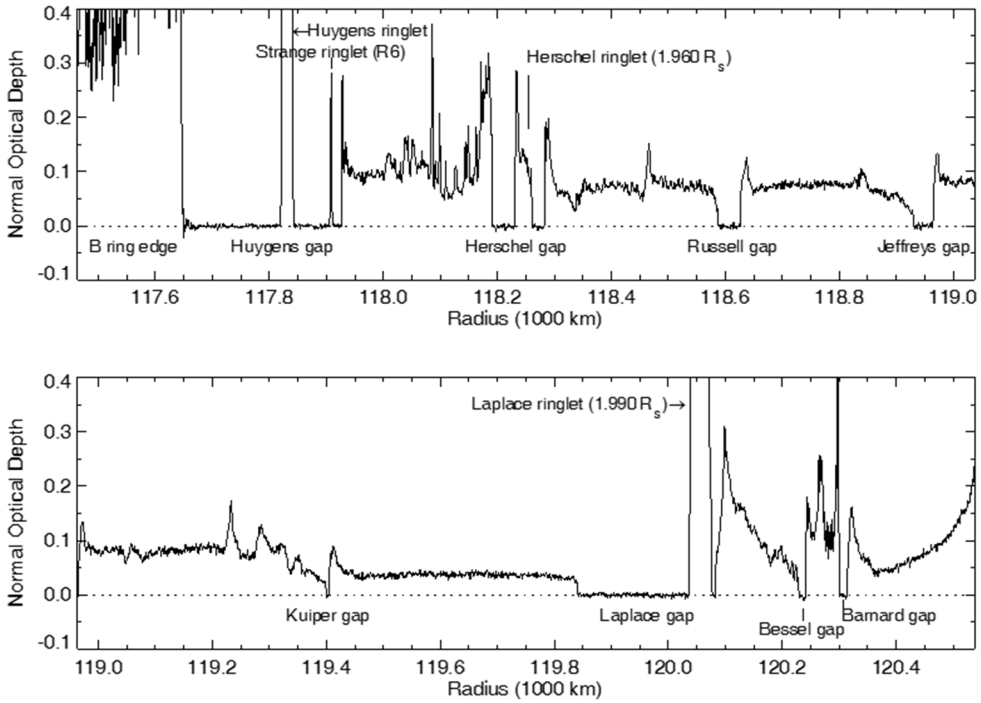

Figure RSS-18. Prominent ringlets and gaps in the Cassini Division shown in an optical depth profile from the Cassini RSS egress occultation on Rev 7. Figure from French et al. [2016].

Among the interesting results found from the analysis of the Cassini Division occultation data is evidence of anomalous precession rates for noncircular features, as shown in Figure RSS-19 from French et al. [2016].

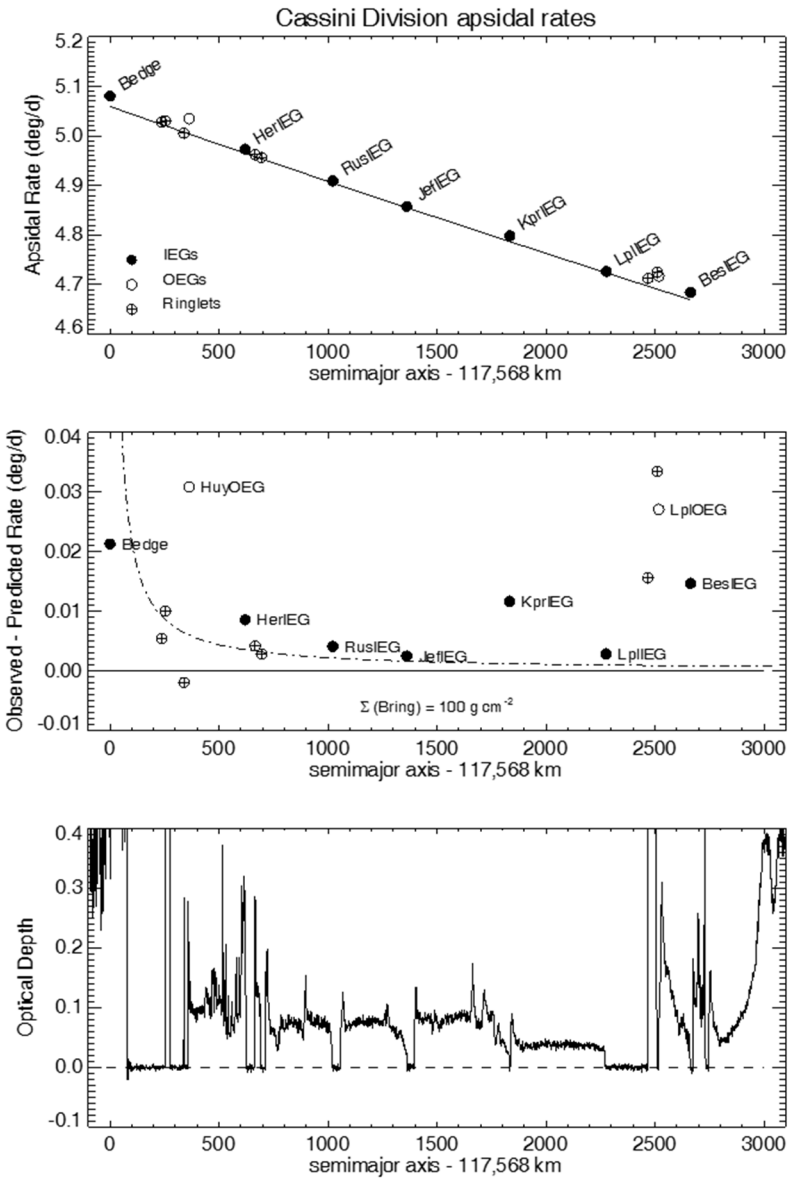

Figure RSS-19. Results found from the analysis of the Cassini Division occultation data *Upper panel*: fitted apsidal precession rates versus mean radius for eccentric features. Note: the quasi-regular sequence in the precession rates for the gap inner edges. The solid line shows the predicted precession rates, calculated from Saturn's zonal gravity coefficients. *Middle panel*: The differences between the fitted and calculated precession rates in the upper panel, using the same symbols. The dot-dashed curve shows the contribution to the apsidal precession rates from the nearby B-ring, assuming a uniform surface mass density of 100 g cm^{-2}. *Lower panel*: Optical depth profile, for context. Figure from French et al. [2016a].

Additional targeted studies of individual ring features were also conducted by the RSS team, including the identification of an m = 2 Saturn-driven density wave in the Maxwell Ringlet [French et al. 2016b]. Figure RSS-20 shows the results of a simulation of the strongly nonlinear density wave embedded in a highly eccentric ringlet.

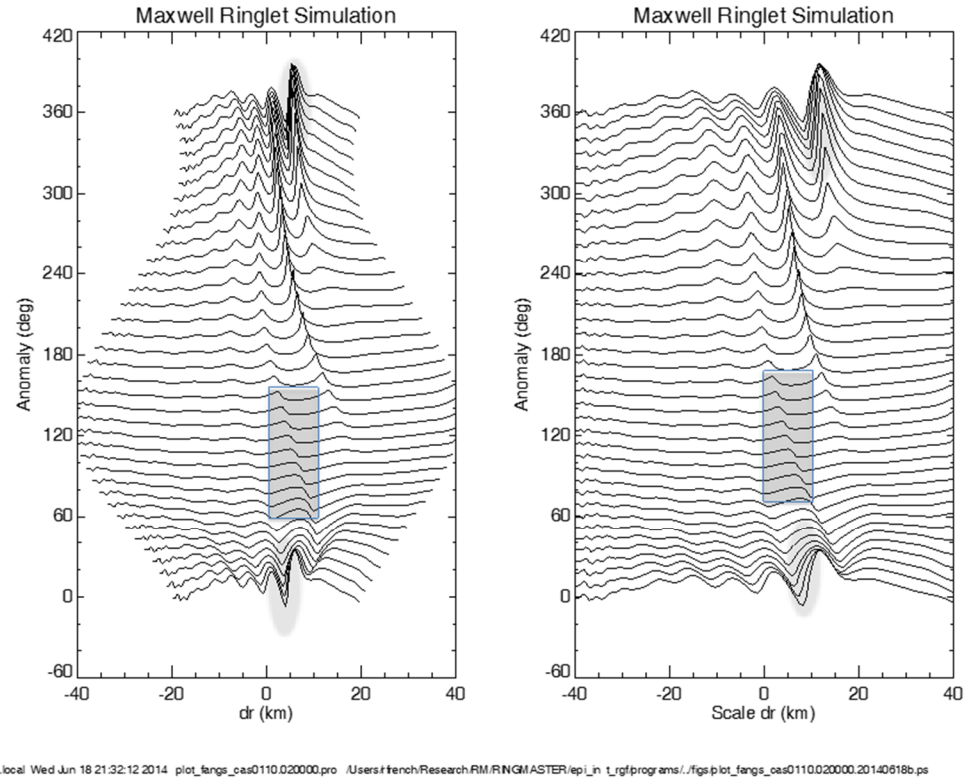

Figure RSS-20. Simulation of non-linear density wave embedded in the eccentric Maxwell Ringlet.

In a recent study of Saturn's F-ring [Cuzzi et al. 2018], RSS F-ring observations, such as those shown in Figure RSS-21, were used to provide evidence for an incomplete core of the F-ring, with arcs of material confined by an unusual resonance with Prometheus.

Density waves in Saturn's rings

Saturn's rings are replete with density waves, and the RSS ring occultations are a rich resource for investigating their properties. Rappaport et al. [2009] developed a novel procedure to analyze nonlinear density waves using multiple occultations, with the goal of determining the underlying unperturbed optical depth of the material in the wave region, and other properties of dynamical interest (Figure RSS-22).

A comparison of density wave profiles observed from RSS, VIMS, and UVIS (Figure RSS-23) shows the exquisite quality of all three occultation techniques.

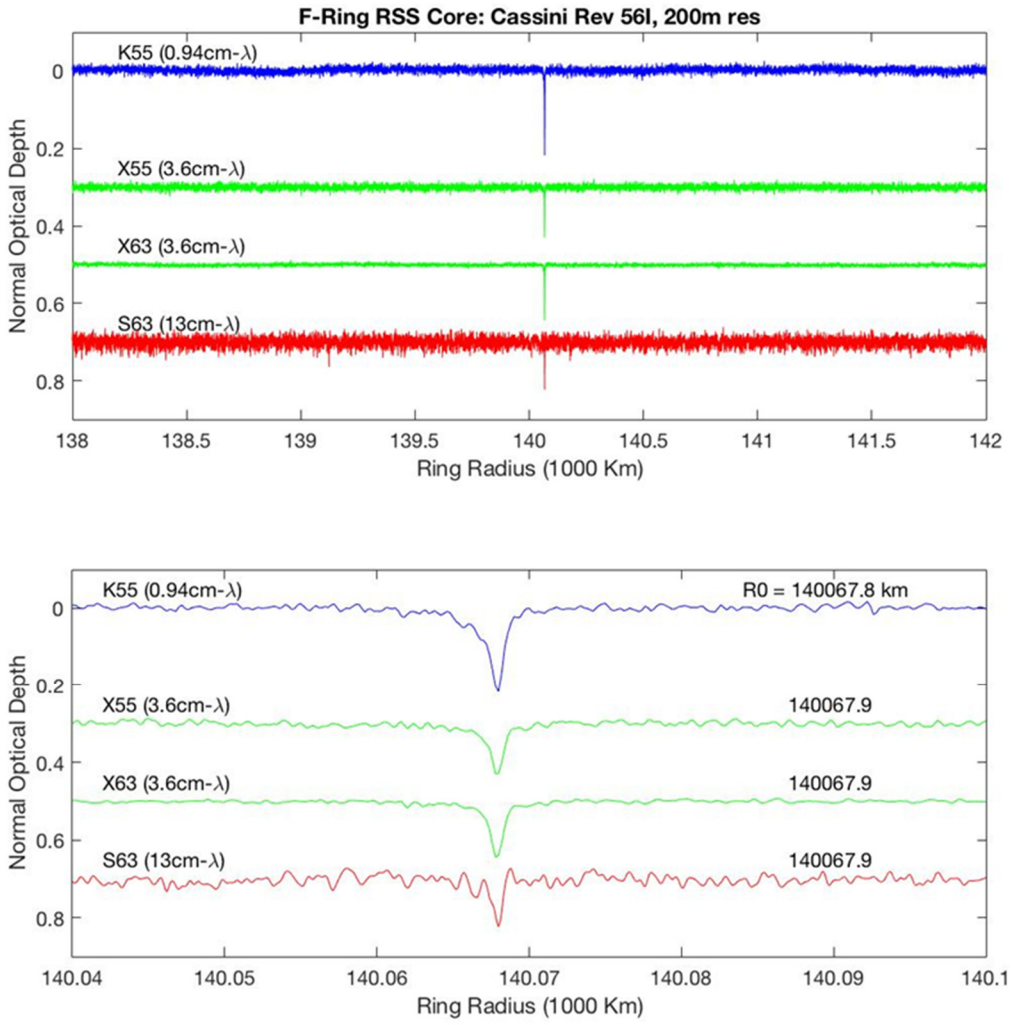

Figure RSS-21. Example Cassini RSS F-ring core detection (ingress occultation on Rev 54, December 19, 2007). The core was detectable in the 0.94, 3.6, and 13 cm-wavelength measurements (Ka-band, X-band, and S-band, respectively; blue, green, and red lines). The measurements were acquired by two of the NASA DSN stations at the Madrid, Spain, complex. DSS-63, a 70-m station, acquired X-band and S-band; DSS-55, a 34-m station, acquired X-band and Ka-band, hence, the four profiles in each panel. The measurements were reconstructed to remove diffraction effects, yielding 200 m radial resolution optical depth profiles. The upper panel shows the profiles over a broad 4000 km wide region outside the outer edge of the A-ring, primarily to provide a free-space baseline for the experiment. A single feature of optical depth large compared with the baseline noise fluctuations is evident in all three bands at ring radius of about 140,100 km. The stretched radius scale of the lower panel (60 km wide) reveals a single feature about 900 m wide of wavelength-dependent peak normal optical depth < 0.2. The narrow RSS F-ring core was detectable in 23 out of 66 ingress or egress Cassini RSS ring occultations completed between May 2005 and August 2013 (~35%). The S-band core was not detectable in all 23.

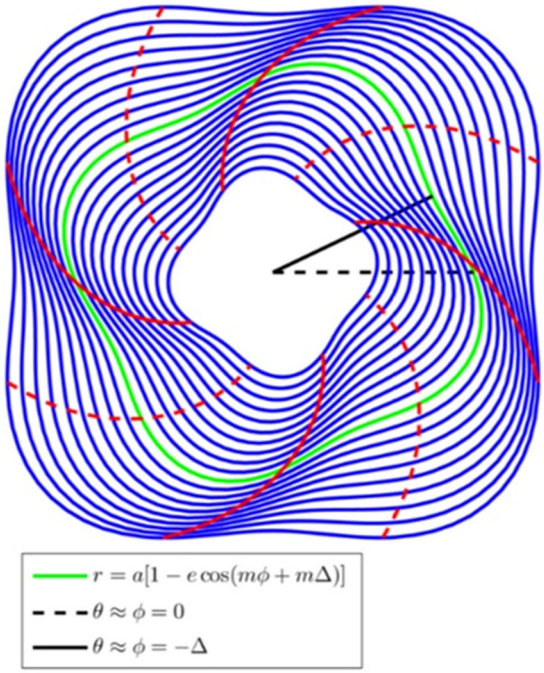

Fig. 1. Streamlines of a 4-lobe ($m = 4$) density wave, such as Mimas 5:3. The lag angle Δ provides the relative shift in angle of one streamline to the next. The loci of constant profile phase ψ corresponding to the density maxima ($\psi = 2\pi n$ with $n = 1$ to 5, solid line) and minima ($\psi = \pi$ modulo 2π, dashed line) are also shown to illustrate the geometrical meaning of ψ. A streamline has been singled out, to show the phase angle Δ.

Figure RSS-22. Density wave model used to analyze RSS observations of Mimas 5:3 density wave. Figure from Rappaport et al. [2009].

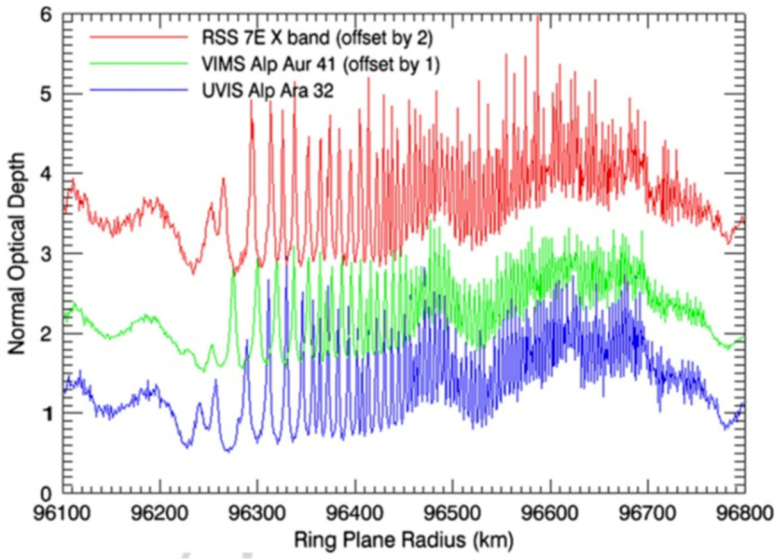

Figure RSS-23. Occultation profiles of the Janus/Epimetheus 2:1 density wave in the B1 region. The resonance locations for Janus and Epimetheus shift when the satellites perform their horseshoe orbit swap every four years and are between 96,210 and 96,250 km. Figure from Colwell et al. [2009].

Particle size distribution

The three-wavelength capability of the RSS observations provides the opportunity to measure the wavelength dependence of the ring optical depth, which can be related to the ring particle size distribution using scattering theory. Figure RSS-24 shows an example of the differential extinction over eight different ring features [Cuzzi et al. 2009]. Figure RSS-25 shows the optical depth contrasts at multiple wavelengths, and the inferred minimum and maximum particle sizes, based on an analysis of RSS occultation data [Cuzzi et al. 2009].

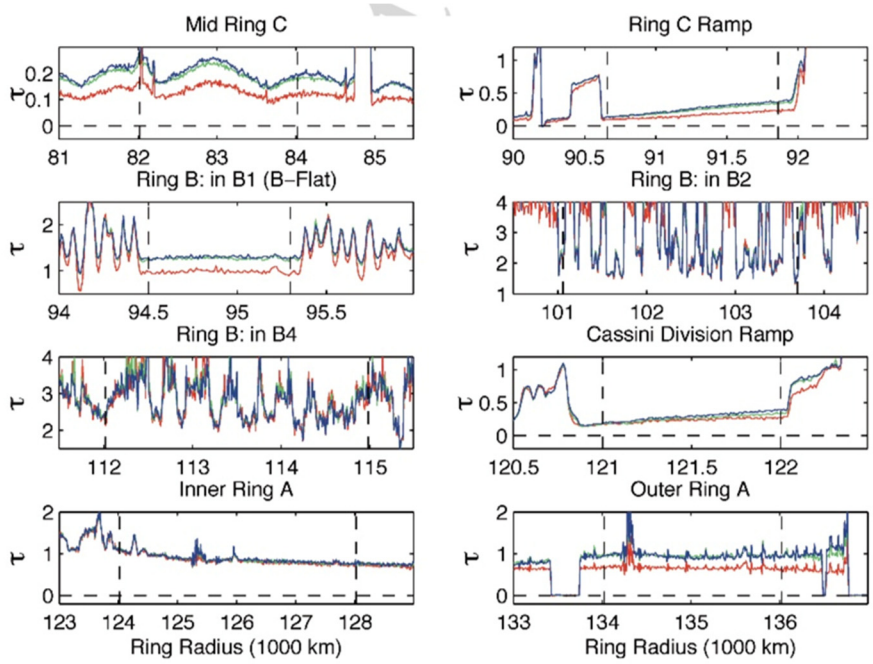

Figure RSS-24. Three-wavelength RSS optical depth profiles of eight ring features identified for examination of the constraints imposed by observed interesting differential extinction, or lack thereof, on parameters of a power-law size distribution model. Figure from Cuzzi et al. [2009].

Periodic microstructure in Saturn's rings A and B

Radio occultation of Saturn's rings by the Cassini spacecraft on May 3, 2005, revealed several remarkable phenomena in rings A and B. In limited regions of the rings, the observations indicate the presence of fine-scale structure characterized by periodic variations in optical depth of period 100–250 meters, which we refer to as periodic microstructure (PM). Our discovery of these structures [Thomson et al. 2006] is based on observation of diffraction effects in 0.94 cm and 3.6 cm wavelength coherent sinusoidal signals transmitted from Cassini through the rings, and received at the ground stations of the DSN. Figure RSS-26 shows the geometry of the ring occultation experiment used to determine the ring microstructure, seen in the spectra illustrated in Figure RSS-27.

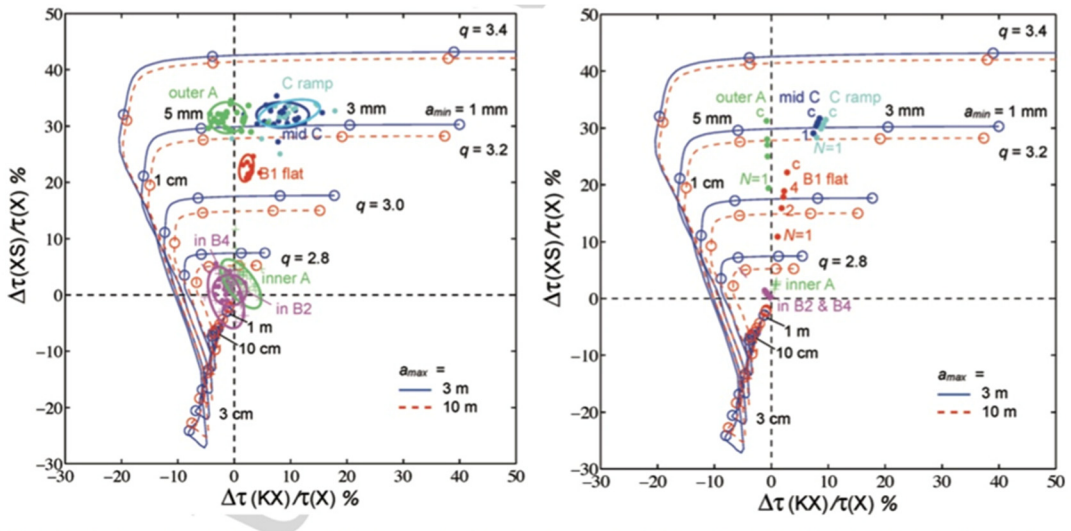

Fig. 15.3 (*Left*) Comparison of the measured X-S (*vertical axis*) and Ka-X (*horizontal axis*) differential optical depth with predictions of a power-law size distribution model of the indicated parameters. For a given power-law index q, the predicted differentials are plotted using the minimum radius a_{min} as a parameter. Points $a_{min} = 0.1, 0.3, 0.5, 1, 3, 10$, and 100 cm are as identified. For each case, dependence on a_{max} is illustrated for the two cases $a_{axn} = 3$ (*solid blue*) and 10 m (*dashed red*). The seven clusters are the values measured for seven of the ring features identified in Figure 3, as labeled. Individual points within each cluster are 80 km resolution samples. The comparison is based on the assumption of a classical (many-particle-thick) ring model. (*right*) Same figure, except that the measured values are scaled based on the thin layers ring model. The five points for each feature correspond to number of layers fours N = 1 to 4 and the classical model result 'c', as labeled. Each point is an average over the radial width of the corresponding ring feature (Marouf et al. 2009)

Figure RSS-25. Optical depth contrasts at multiple wavelengths and the inferred minimum and maximum particle sizes. Figure from Cuzzi et al. [2009].

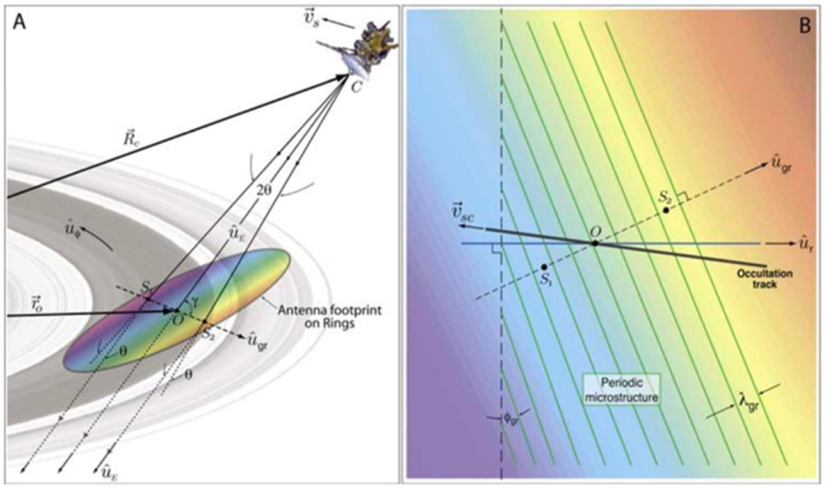

Figure 1. Geometry of the ring occultation experiment. (a) Line-of-sight ray linking Cassini and Earth is directed along $\hat{u}_E$ and pierces the ring plane at point **O**; $\hat{u}_{gr}$ is in the plane of the rings, and defines the orientation of the periodic structure. Points S_1 and S_2 correspond to locations in the ring plane where first-order diffraction grating lobes of the structure originate and propagate along $\hat{u}_E$ to the Earth-based receiver. The grating lobes are directed at angle $\pm\theta$ relative to $\hat{u}_E$. All angles shown are in the plane defined by $\hat{u}_E$ and $\hat{u}_{gr}$. Color within the antenna footprint represents variations in Doppler shift of signals scattered to Earth by the rings; footprint size is exaggerated for clarity. (b) View is of the ring plane. Signals diffracted to Earth from S_1 and S_2 are Doppler-shifted by f_{D1} and f_{D2} relative to the signal along the line-of-sight, represented by the colors at S_1 and S_2. $\hat{u}_r$ is a radial unit vector pointing from the center of Saturn to **O**, and $\vec{v}_{sc}$ is the projection in the ring plane of Cassini velocity $\vec{v}_c$.

Figure RSS-26. The geometry of the ring occultation experiment used to determine the ring microstructure. Figure from Thomson et al. [2006].

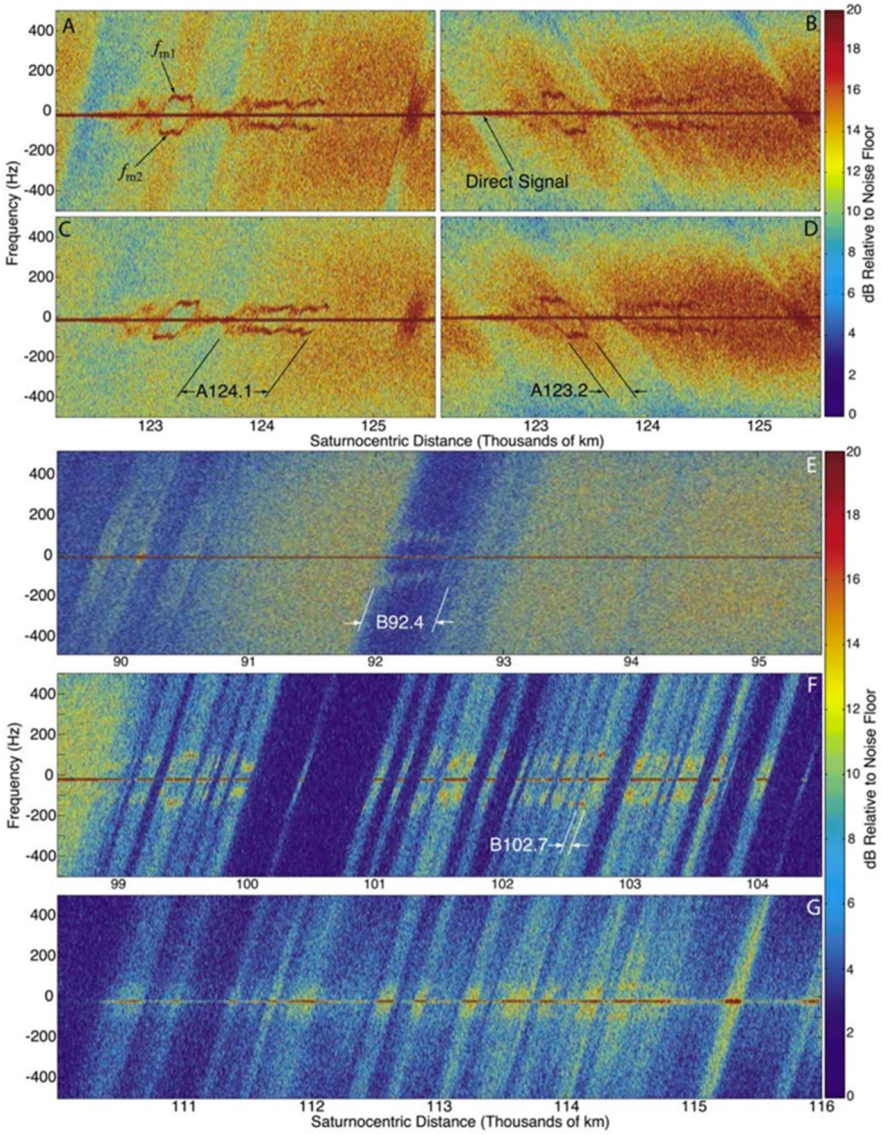

Figure 2. Spectrograms of 3.6 cm-λ signal observed during May 3, 2005, ring occultation (a, e, f, g) ingress and (b) egress; and on August 2, 2005, occultation (c) ingress and (d) egress. The direct signal is the horizontal brown line near the center of each panel. The diffraction signature of periodic microstructure appears as roughly parallel horizontal lines displaced ±70–100 Hz from the direct signal in Ring A (Figures 2a–2d) and ±50–120 Hz Ring B (Figures 2e–2g). The signature is clearly evident for the two indicated features in inner Ring A, over the roughly 500 km inner part of region B1 (Figure 2e) and over most of the detectable subregions of the ≈5000 km-wide region B2 (Figure 2f). It is more muted over most of region B4 (Figure 2g). Other evident broadband features correspond to energy forward scattered by the background wake structure in the rings.

Figure RSS-27. The geometry of the ring occultation experiment seen in the spectra. Figure from Thomson et al. [2006].

Open questions

After more than a decade of ring observations at Saturn, fundamental questions remain about the origin of ring structure and confinement mechanisms for sharp-edged ring features.

- What confines the Titan and Maxwell ringlets?
- Is it a coincidence that the Maxwell ringlet harbors a density wave?
- Did the driving resonance behind the density wave contribute in some fashion to the formation of the ringlet?
- Did the Titan ringlet form in response to its near-resonance with Titan itself?
- Where did the C-ring plateaus originate?
- What drives the host of normal modes detected in sharp ring and edge gaps?
- Is there detectable radial evolution of ring features on the time scale of decades and centuries?

RSS Non-Saturn Science Results

Cruise Science

Gravitational wave experiment

Introduction[1]

One of the cruise-phase Cassini science investigations was to use Cassini's precision Doppler tracking capability to search for GWs. The idea [Estabrook and Wahlquist 1975] is that Earth and Cassini act as electromagnetically-tracked free test masses. The Earth-spacecraft relative velocity is continuously measured via Doppler shifts of microwave links referenced to a ground-based precision frequency standard. Such as system can be used to search for low-frequency (~10^{-6} to 10^{-1} Hz) GWs.[2]

Signal response

Figure RSS-28 shows the effect of a burst GW incident on the Earth-Cassini system. The Doppler responds to a projection of the time-dependent wave metric, in general producing a three-pulse

---

[1] *Much of this report, including the figures, comes from Armstrong, et al. [2003], and Armstrong [2006].*

[2] *Gravitational wave bands conventionally divide based on detector technology [Thorne 1987]: extremely-low-frequency (~10^{-18} to ~10^{-15} Hz) search programs are based on mapping the intensity and polarization of the cosmic microwave background; very-low frequency observations (~10^{-9} to ~10^{-6} Hz) use pulsar timing observations; low-frequency (~10^{-6} to ~10^{-1} Hz) observations currently use Doppler tracking of spacecraft (in the 2030s, a laser interferometer in space); high-frequency (~10 to ~10^{3} Hz) observations involve ground-based laser interferometers. The ground-based LIGO detectors made the first detection of GWs in 2015, for which the 2017 Nobel Prize in physics was awarded.*

response to a pulse of incident gravitational radiation: one event due to buffeting of the Earth by the GW, one event due to buffeting of the spacecraft by the GW, and a third event in which the original Earth buffeting is transponded a two-way light time later. The amplitudes and locations of the pulses depend on the arrival direction of the GW with respect to the Earth-spacecraft line, the two-way light time, and the wave's polarization state [Estabrook and Wahlquist 1975]. Technical details of the detector, including polarization response, are in references in Armstrong [2006].

The Cassini experiment is distinguished by its 5-link radio system. This system (X-up, X-down coherent with X-up, Ka-down coherent with X-up, Ka-up, Ka-down coherent with Ka-up) allowed essentially perfect rejection of plasma scintillation noise, a dominant noise source for earlier-generation spacecraft observations—for example, Tortora et al. [2004]; Asmar et al. [2005]; Mariotti and Tortora [2013]. Cassini observations also benefitted from an Advanced Media Calibration unit—water vapor radiometer and microwave temperature profiler—which allowed measurement and removal of a substantial fraction of propagation noise from the neutral atmosphere [Keihm et al. 2004]. Discussion of the noise budget is in Bertotti et al. [2003]; Asmar et al. [2005]; and Armstrong [2006].

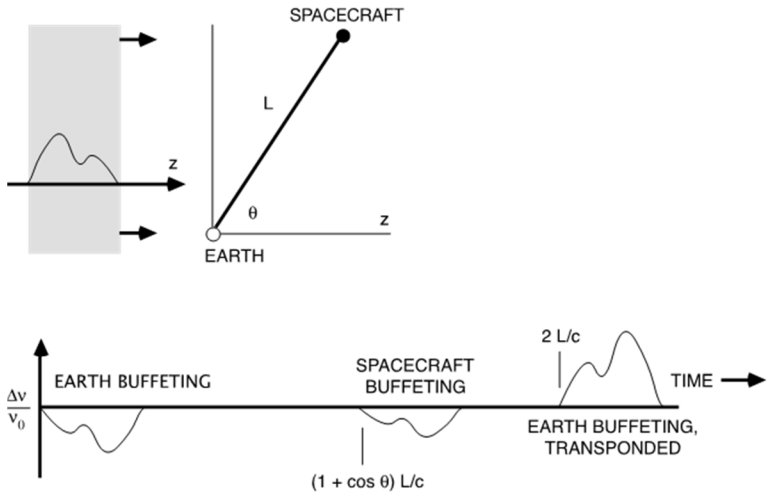

Figure RSS-28. Schematic response of two-way Doppler tracking to a GW [Estabrook and Wahlquist 1975]. The Doppler exhibits three pulses having amplitudes and relative locations which depend on the GW arrival direction, the two-way light time, and the wave's strain amplitude and polarization state. The sum of the three pulses is zero, so the pulses overlap and partially cancel when the characteristic time of the GW pulse is comparable to or larger than the light time between the Earth and spacecraft.

Three GW observing campaigns were done during Cassini cruise: (i) November 25, 2001 to January 4, 2002; (ii) December 5, 2002 to January 14, 2003; and (iii) November 10, 2003 to November 28, 2003—the last being done with X-up and X-down only due to the failure of the Cassini Ka-band translator.

The spectrum of the propagation-corrected data from the first observing campaign is shown in Figure RSS-29. The associated 1000-second Allan deviation (fractional frequency variation), for

the full 40 days of the observation, is 6×10^{-15}. The velocity noise is thus about 1 μm/sec in a 1000-second integration. These are the most sensitive deep space Doppler measurements ever made.

Sensitivity is conventionally stated as the sky- and polarization-averaged sinusoidal signal strength required to achieve a given signal to noise ratio in a specified integration time, as a function of Fourier frequency. This is shown in Figure RSS-30 for a signal-to-noise ratio of unity in a 40-day integration. This ~10^{-16} value (in the ~decade Fourier range of best sensitivity) is also the SNR = 1 sensitivity limit for sinusoidal GWs or linear chirps.

For GW signals having more complicated Fourier composition the sensitivity is lower and in general depends on waveform shape and angle-of-arrival of the GW relative to the Earth-Cassini line. Figure RSS-31 shows the characteristic strain sensitivity for generic burst waves (bandwidth = center frequency) averaged over the sky and polarization states.

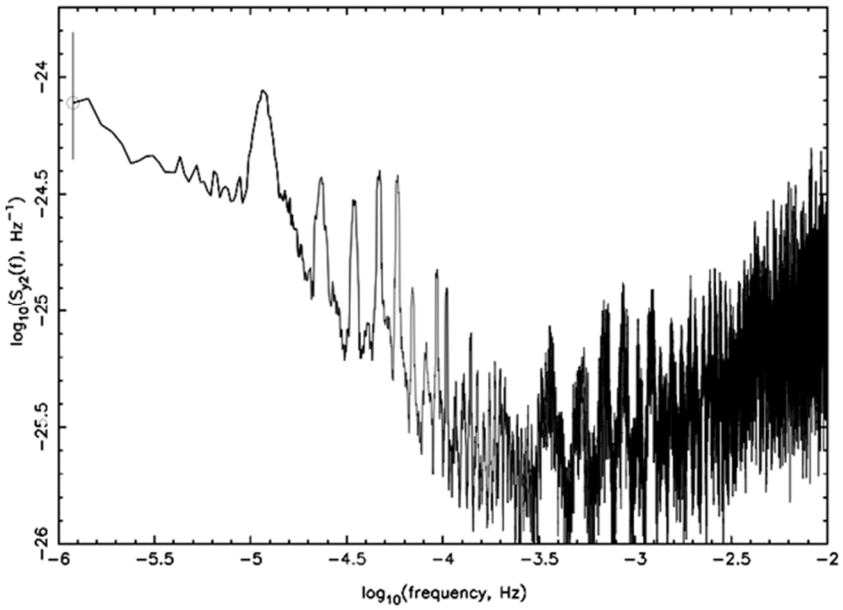

Figure RSS-29. Spectrum of two-way Doppler for the 2001–2002 Cassini observations. The associated 1000s Allan deviation is 6×10^{-15}, corresponding to 1 μm/sec velocity noise on a 1000s integration time [Armstrong et al. 2003].

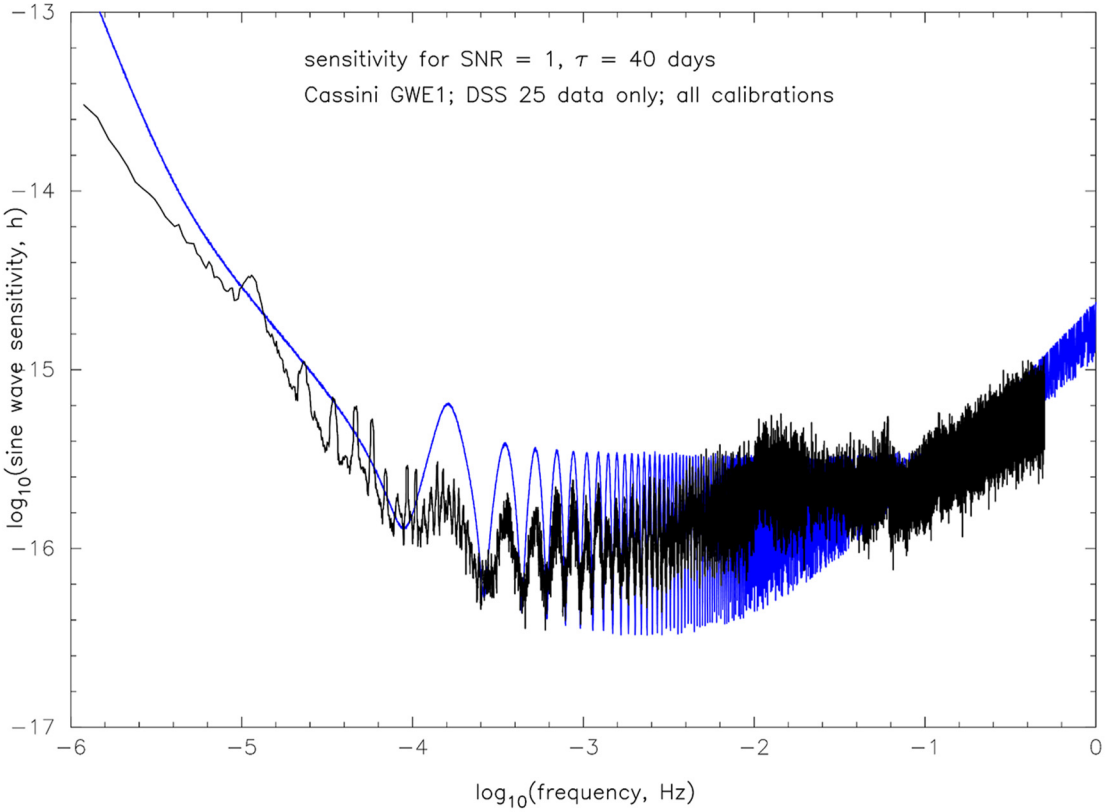

Figure RSS-30. Sensitivity of the Cassini 2001–2002 gravitational wave observations, expressed as the equivalent sinusoidal strain sensitivity required to produce SNR = 1 for a randomly polarized isotropic background, as a function of Fourier frequency. This reflects both the levels, spectral shapes, and transfer functions of the instrumental noises and the GW signal transfer function. Black curve: sensitivity computed using smoothed version of observed Doppler spectrum. Blue curve: sensitivity computed from pre-observation predicted noise spectrum. Figure from Armstrong [2006].

The Cassini data can also be used to bound the level of a stochastic background of GWs [Armstrong et al. 2003]. This is shown in Figure RSS-32 relative to the density required to gravitationally close the universe. These limits are about three orders of magnitude more stringent than any others from Doppler tracking.

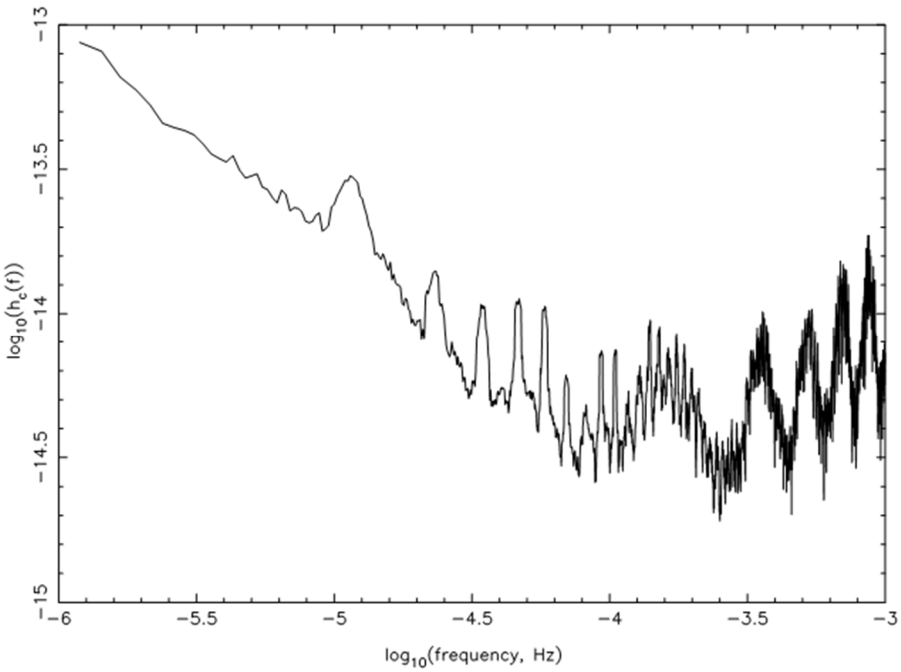

Figure RSS-31. Sensitivity of the Cassini 2001–2002 burst gravitational wave observations, expressed as characteristic strain sensitivity (GW bandwidth = center frequency) averaged over the sky and polarization state. Figure from Armstrong [2006].

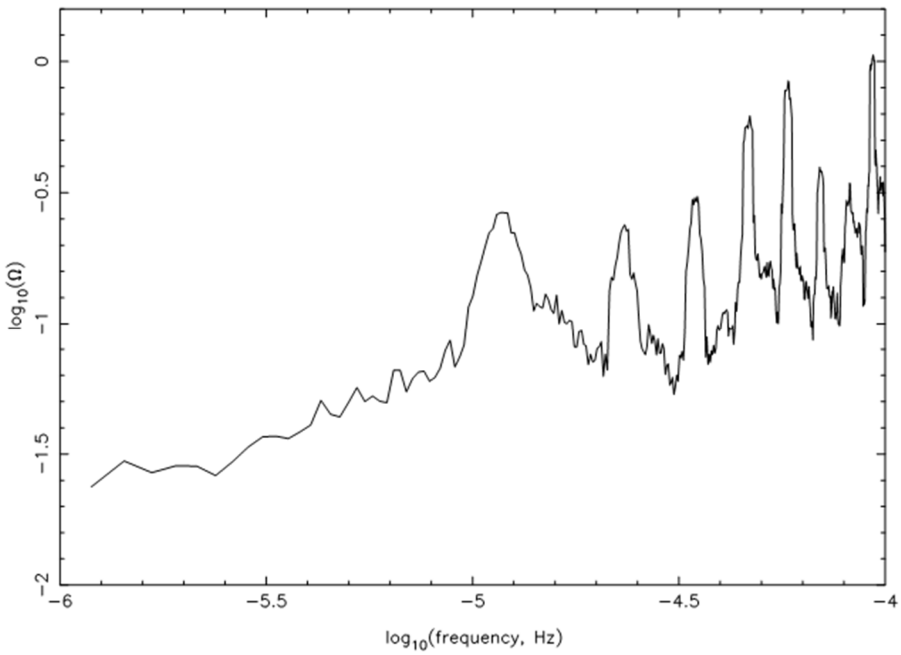

Figure RSS-32. Upper limits to GW energy density (bandwidth = center frequency) divided by the critical density required to close the universe of an isotropic GW background. Figure from Armstrong et al. [2003].

Solar conjunction experiment

INTRODUCTION[3]

In addition to the gravitational wave experiment, another cruise-phase Cassini science investigation was to use Cassini's radiometric data to measure the space components of the Sun's metric tensor. In the parameterized post-Newtonian formalism, this quantity is controlled by a parameter (γ) which is unity in General Relativity but may assume slightly different values in other metric theories of gravity. The measurement of γ with Cassini is based upon a new observable quantity: the frequency shift induced on a radio wave when the spacecraft is near solar conjunction. The calibration of the large frequency fluctuations induced by the solar corona, necessary in order to guarantee the required signal stability, was performed using the novel Cassini radio frequency system, based on a multi-frequency link.

PREVIOUS TESTS AND CASSINI'S EXPERIMENTAL CONFIGURATION

During a SCE, radio-metric data are used to measure the space curvature produced by the Sun. The parametrized post-Newtonian (PPN) parameter γ was estimated by other space-based experiments which allowed to bound the value of γ-1 to less than 0.001 using range measurements to the Viking landers [Reasenberg et al. 1979], an experiment carried out more than 20 years before Cassini's one, and more recently, using Very Long Baseline Interferometry techniques [Eubanks et al. 1997].

The measurement of γ with Cassini is based upon a new observable quantity: the frequency shift induced on a radio wave when the spacecraft is near solar conjunction. For this experiment, the geometry is particularly favorable and the relativistic relative frequency shift is on the order of 10^{-9}. On the other hand, this large Doppler signal is obtained only at small impact parameters, when the radio beam, well inside the solar corona, exhibits large frequency fluctuations. The solar plasma calibration, made possible by the multi-frequency link [Bertotti et al. 1993; Tortora et al. 2003, 2004; Mariotti and Tortora 2013], plays a crucial role in the experiment. In this method, the sky-frequencies in the three bands (X/X, X/Ka, Ka/Ka) are coherently combined to remove the effects of the solar plasma, the major noise source in the Doppler observable. Furthermore, the use of water vapor radiometers and microwave temperature profilers [Resch at al. 2002; Keihm et al. 2004], developed for the Cassini RSE, provides a precise calibration of the frequency shift due to the troposphere. The predicted stability of the radio link, once all media calibrations were applied, was in the order of 10^{-14} at integration times of 1000 s, showing that the Cassini experiment may have provided a measurement of γ to a level between 10^{-5} and 10^{-4}, one or two orders of magnitude better than previous experimental tests.

---

[3] *Much of this report, including the figures, comes from Iess et al [2003], and Bertotti et al [2003].*

CASSINI EXPERIMENT

The increase Δt produced by the gravitational field of the Sun (with mass M_S and radius R_S) in the roundtrip light-time between the ground antenna and the spacecraft, respectively, at the distances r_1 and r_2 from the Sun, is [Will 1993]:

$$\Delta t = 2(1+\gamma)\frac{GM_S}{c^3}\ln\left(\frac{4r_1r_2}{b^2}\right), \quad \text{(Eq. 1)}$$

where G is the gravitational constant and b (<< r_1, r_2) the impact parameter. The motion of the spacecraft and Earth produces a change in b and Δt, equivalent to a change in distance, hence to a relative radial velocity. The corresponding fractional frequency $y_{gr} = \Delta v/v$ shift for a two-way radio signal is [Iess et al. 1999]:

$$y_{gr} = \frac{d\Delta t}{dt} = -2(1+\gamma)\frac{GM_S}{c^3 b}\frac{db}{dt} = -(1\times 10^{-5}\ \text{sec})(1+\gamma)\frac{1}{b}\frac{\mathrm{d}b}{\mathrm{d}t}. \quad \text{(Eq. 2)}$$

For a spacecraft much farther away from the Sun than Earth, db/dt is not very different from the Earth's velocity v_E = 30 km/sec. In the Cassini solar conjunction the peak value of y_{gr} is 6×10^{10}. The Cassini experiment, exploiting this new observable [Iess et al. 1999; Bertotti and Giampieri 1992], has been carried out from June 6, 2002 to July 7, 2002, when the spacecraft was on its way to Saturn, around the time of a solar conjunction (Figure RSS-33).

The gravitational signal and the tracking passes which provided useful data [Iess et al. 2003] are shown in Figure RSS-34.

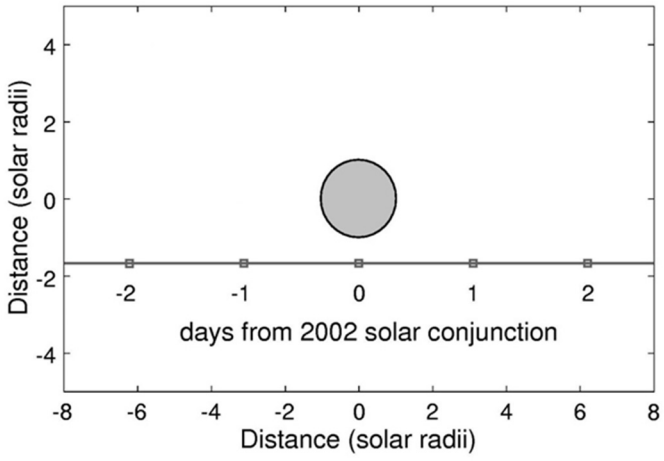

Figure RSS-33. Geometry of the 2002 Cassini solar conjunction. Cassini's motion in the sky relative to the Sun, as a function of days from the 2002 solar conjunction; coordinates are in solar radii. The conjunction, at which the spacecraft (at a geocentric distance of 8.43 AU) Sun and Earth were almost aligned (in this order), occurred on 21 June 2002 with a minimum impact parameter b_{min} = 1.6 R_S, and no occultation.

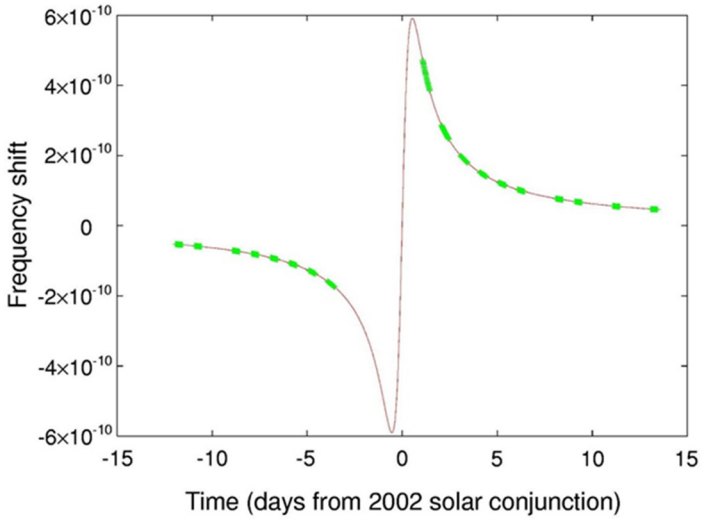

Figure RSS-34. The gravitational signal. The two-way relativistic frequency shift y_{gr} due to the sun and the available 18 passages, each lasting about 8 hours. Unfortunately, no data could be acquired for three days just before conjunction, due to a failure of the ground transmitter; moreover, the tracking data acquired near closest approach were particularly noisy. A much larger plasma noise was detected in some passes after conjunction and was fully removed by the multilink technique. Remarkably, in these days Solar and Heliospheric Observatory (SOHO) observations have shown large coronal mass ejections (CME) traversing the radio beam.

The main reason why the Doppler method has not been applied before is the overwhelming noise contribution due to the solar corona. The Cassini mission has overcome this hindrance with: a) high-frequency carriers in Ka-band, in addition to the X-band for standard operation; and b) a multi-frequency link in which three different phases are measured at the ground station. The resulting measurement errors are four orders of magnitude smaller than the relativistic signal (Eq. 2).

The dynamical model used in the orbital fit of Doppler data is particularly simple, thanks to the large distance from the Sun, the location of the spacecraft in interplanetary space and the lack of unknown gravitational perturbations by solar system bodies. JPL's Orbit Determination Program has been used in the integration of the equations of motion and the orbital solution, based upon planetary ephemerides and ancillary data, such as station location and Earth orientation parameters.

We have used up to 12 free solve-for parameters: a) the six components of the state vector at the start of the experiment; b) the three components of the non-gravitational acceleration due to the RTG in the spacecraft frame; c) the specular and diffuse reflectivity of the high gain antenna, which determine the magnitude (and the direction) of the non-gravitational acceleration due to solar radiation pressure; and d) the relativistic parameter γ. Consider-parameters (quantities not solved-for, but whose uncertainty is taken into account in the solution) include the dry troposphere, the station location, polar motion, and the Earth Love numbers (which intervene in the solid tide model).

Among the five parameters which control the nongravitational acceleration, three (the nonradial components of the thermal thrust from the RTG and one of the two optical coefficients of the high gain antenna) are poorly determined. It is, therefore, appropriate to investigate a solution including

only the other two, namely the radial acceleration due to the RTG and the diffuse reflectivity of the antenna; by so doing, most nongravitational perturbations are accounted for at a level consistent with the accuracy of the tracking data. The value of the other three parameters, the specular reflectivity and the nonradial components of the RTG acceleration, together with their uncertainties, have been taken from a separate fit carried out on the data from the Cassini solar opposition experiment, as mentioned earlier. This is our main orbital fit (see Figure RSS-35), with only nine parameters to be determined. The a priori uncertainty of the parameters which are not estimated, but affect the solution (such as the station geocentric coordinates and those derived from the gravitational wave experiment) has been included in the computation of the covariance matrix.

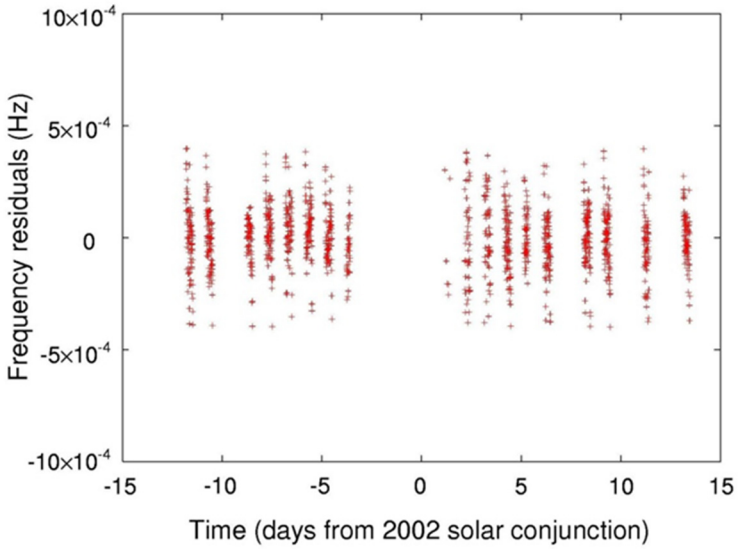

Figure RSS-35. The Doppler residuals. Two-way frequency residuals, relative to an 8.4 GHz carrier, as a function of time (in days from solar conjunction), obtained from the final 9-parameter fit on the calibrated data. The rms value of the 1094 data points (compressed at a 300 s integration time) is 1.2×10^{-4}, Hz corresponding to a one-way range rate of 2.2×10^{-6} m/s; this is an unprecedented accuracy for tracking data at solar conjunction.

Our result [Bertotti et al. 2003] $\gamma = 1 + (2.1 \pm 2.3) \times 10^{-5}$ agrees with Einstein's, with an accuracy ≈ 50 times better than published measurements. While a fundamental force such as gravity must always be investigated as accurately as possible, our result approaches a sensitivity at which, theoretically, deviations from General Relativity are expected.

Conclusions

The question, at what level violations of General Relativity can be expected, does not have a satisfactory answer yet. A long-range scalar field is currently assumed to play a fundamental role in primordial cosmology; although it decays with the expansion of the Universe, its present remnant would entail not only violations of the two main tests of General Relativity, but also a lack of universality of the constants of microphysics, as assumed in the Equivalence Principle [Damour et al. 1994, 2002].

A claim, based upon quasar absorption lines, that the fine structure constant α was weaker in the distant past has been recently made, thereby violating the Equivalence Principle [Murphy 2001a, 2001b, 2001c, 2001d]; if confirmed, and reconciled with other constraints on the variation of fundamental constants [Damour 2003], such finding would be the first serious challenge to Einstein's paradigm. No detailed theory is available about the expected amounts of these violations, but $\gamma - 1$ should be negative and, possibly, in the range 10^{-5}–10^{-7}. Therefore, our result, with an accuracy not far from this range, places an important constraint on this cosmological scenario.

Solar wind

INTRODUCTION

Before the failure of the Ka-band translator, Cassini's five-link radio system (X-up, X-down coherent with X-up; Ka-down coherent with X-up; Ka-up; Ka-down coherent with Ka-up) allowed a decomposition of the Doppler time series into three components: a non-dispersive component, the uplink-path plasma component, and the downlink-path plasma component [Iess et al. 2003; Bertotti et al. 2003; Tortora et al. 2003, 2004]. Having the up- and downlink plasma time series separately allowed the first localization along the line-of-sight and time of plasma turbulence between the ground station and the Cassini spacecraft.

Before the failure of the Ka-band translator, Cassini's five-link radio system … allowed a decomposition of the Doppler time series into three components: a non-dispersive component, the uplink-path plasma component, and the downlink-path plasma component … .

The idea has its origin in noise budget analysis of precision Doppler tracking experiments [Estabrook and Wahlquist 1975; Estabrook 1978; Vessot and Levine 1978] and is illustrated in Figure RSS-36. The upper plot is a space-time diagram, showing the ground station continuously transmitting a signal to Cassini and continuously receiving a signal from the spacecraft. In the two-way mode, the Doppler time series $y_2(t)$ has its phase perturbed by a localized plasma blob at distance x along the line-of-sight as illustrated, giving rise to two events in the two-way tracking time series separated by a time lag depending on the Earth-blob distance: $T_2 - 2\ x/c$, where T_2 is the two-way light time.

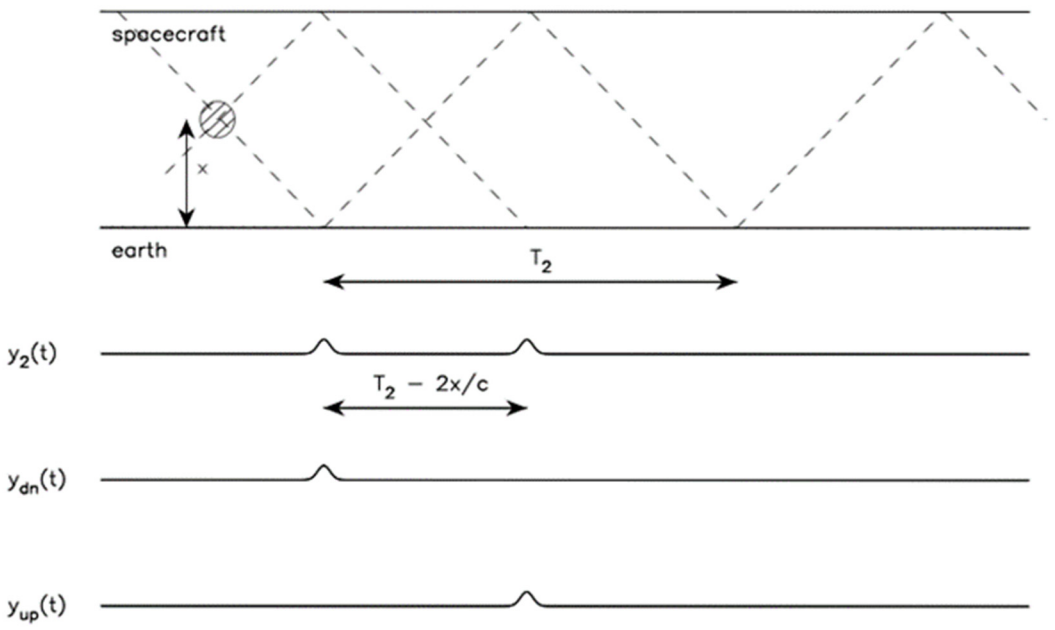

Figure RSS-36. Transfer function of plasma fluctuations to one-way and two-way phase/Doppler scintillation allows localization of plasma blobs along the line-of-sight. Upper plot is a space-time diagram (space vertically, time horizontally). The ground station and the spacecraft are continuously exchanging microwave signals, some of which are shown as dashed lines. If the signals pass through a well-localized plasma blob (indicated by the crosshatched circular area) the phase is perturbed. This perturbation is observed on both the uplink and downlink signals and on the two-way Doppler. The two-way, $y_2(t)$, and the one-way plasma-contribution Doppler time series, $y_{up}(t)$ and $y_{dn}(t)$, are shown in the *lower plot*. The phase perturbation is seen initially on the downlink, and (in the two-way Doppler) latter when the perturbation on the uplink is phase-coherently retransmitted back to the ground. The effect in $y_2(t)$ is two positively-correlated features in the time series, separated in time by $T_2 - 2x/c$, where T_2 is the two-way light time and x is the distance of the blob from the Earth. The one-way up and down Doppler time series detect the blob once each, but also separated by $T_2 - 2x/c$. Cross-correlation or windowed matched filtering between y_{up} and y_{dn} allows an estimate of the time delay thus the location of the blob.

Demonstration with Cassini Data on 2001 DOY 149

As described more completely in Richie-Halford et al. [2009] (from which the discussion and figures here are taken), the proof of concept observations were made with Cassini and DSS25 on 2001 DOY 149 (= 2001 May 29; Sun-Earth-spacecraft angle ≈ 6.6 degrees; $T_2 \approx 6825$ seconds, varying by ≈ 2 seconds over the pass). The full five-link system was used and Figure RSS-37 shows the inferred uplink and downlink plasma scintillation as a function of time. It is usually thought that plasma scintillation arises from distributed scattering along a large fraction of the line of sight. In this case, however, large, similarly-shaped events in the two time series are obvious. The time-offset is indicative of highly localized plasma turbulence in the solar wind on this day. Figure RSS-38 shows the location of this dominant screen in the solar wind as a function of time on DOY 149.

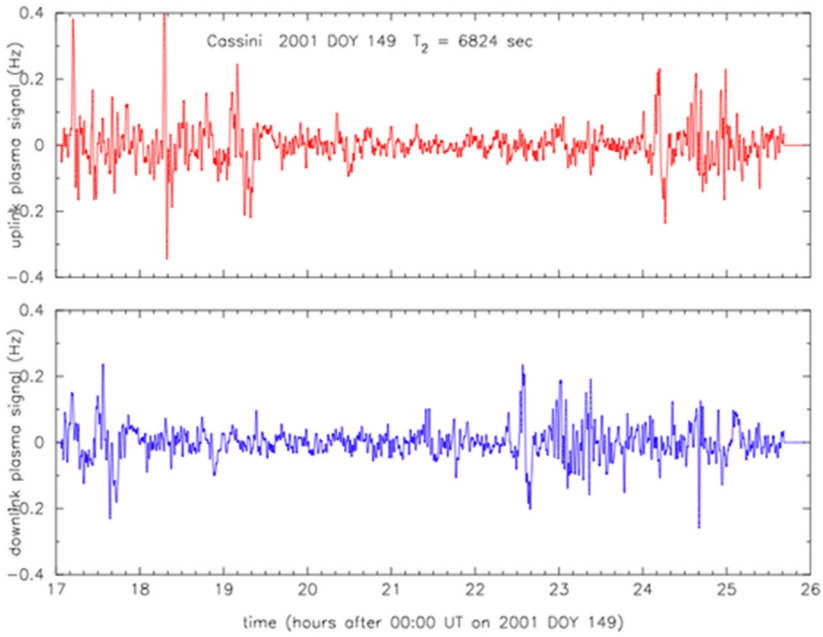

Figure RSS-37. Time series of the plasma contribution to the X-band up- and down links, $y_{up}(t)$ and $y_{dn}(t)$, for DSS25 Cassini track on 2001 DOY 149 = 2001 May 29. The two-way light time T_2 was ≈ 6824 seconds. Several large amplitude features in the downlink time series, for example at about 1730 UT, 2230 UT, 2300 UT, have clear echoes in the uplink time series with time difference ~T_2 − 2∗1.028 AU/c.

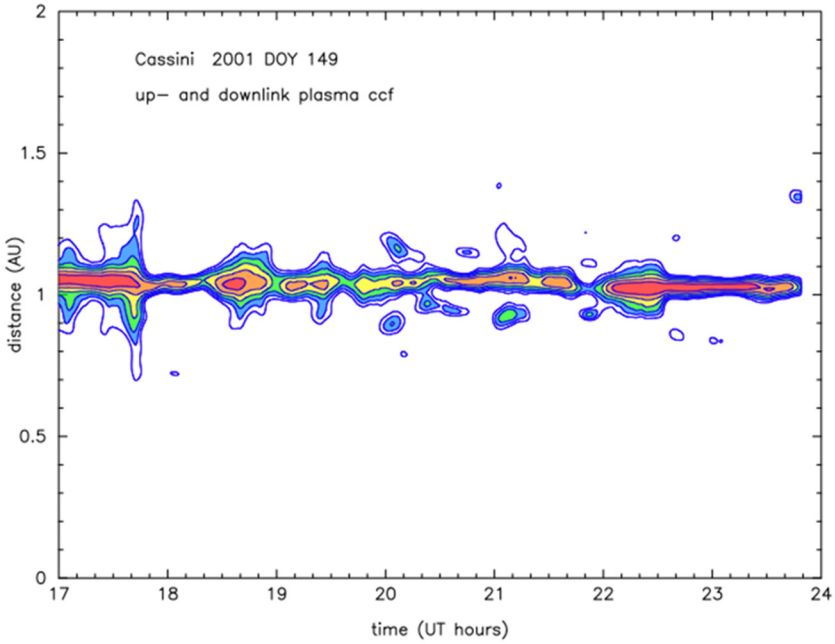

Figure RSS-38. Space-time cross-correlation function of the 2001 DOY 149 plasma up- and downlink time series plotted in Figure RSS-37. Y-axis is the distance from the Earth; x-axis is downlink received time. Contours of cross correlation value are plotted between 0.9 and 0.4, in 0.1 increments. Correlations > 0.9 are shaded red, those between 0.8 and 0.9 in orange, etc.

CONTEXT FROM NEAR-SUN CORONAL DENSITY OBSERVATIONS

Richie-Halford et al. [2009] looked at coronal data to see if there was an obvious plane-of-sky counterpart for the localized plasma on 2001 DOY 149. Figure RSS-39 shows a map of the coronal density structure at a height of four solar radii for Carrington Rotation 1976. Red is high density, black is low. The x-axis is Carrington rotation longitude, the y-axis is solar latitude. The point along the Earth-Cassini line of sight closest to the Sun is shown as a diamond on the map. The three dotted and dashed lines are the position of the heliospheric current sheet, calculated using various models. The positional agreement suggests the highly-localized plasma seen by Cassini is associated with the heliospheric current sheet on DOY 149.

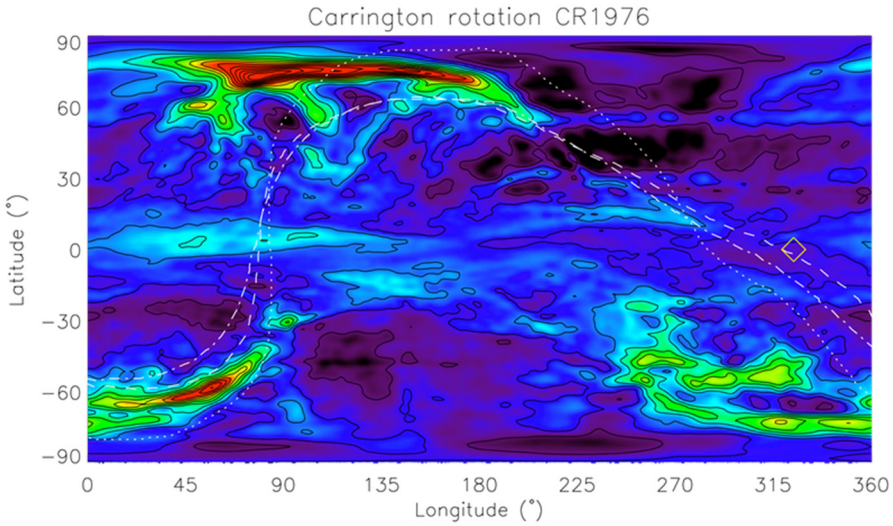

Figure RSS-39. Map of coronal density structure at a height of 4 solar radii for Carrington Rotation 1976, calculated using a solar rotational tomography technique from ~2 weeks of LASCO/SOHO C2 coronagraph observations. Red is high density, black is low. The x-axis refers to Carrington longitude, the y-axis to solar latitude. The point along the Earth-Cassini line of sight closest to the Sun is shown as a diamond. The three dotted and dashed lines are the position of the heliospheric current sheet, calculated using different models. The positional agreement suggests the highly-localized plasma seen by Cassini is associated with the heliospheric current sheet on this day.

LOCALIZATION ON OTHER DAYS

The localization of the dominant plasma turbulence on 2001 DOY 149 is remarkable but perhaps not typical. Figure RSS-40 shows analysis for 2002 DOY 160 = 2002 June 9 (Sun-Earth-spacecraft angle ≈ 9.5 degrees; two-way light time ≈ 8365 seconds). Correlation levels are in general lower than those in Figure RSS-38 for 2001 DOY 149. At the start of the track a scattering region nearer to the Earth than the ray path closest approach point (≈ 1AU∗cos(9.5 degrees) = 0.986 AU) is indicated. In mid-track, the correlation is particularly low, indicative of extended, rather than localized, scattering for much of this day.

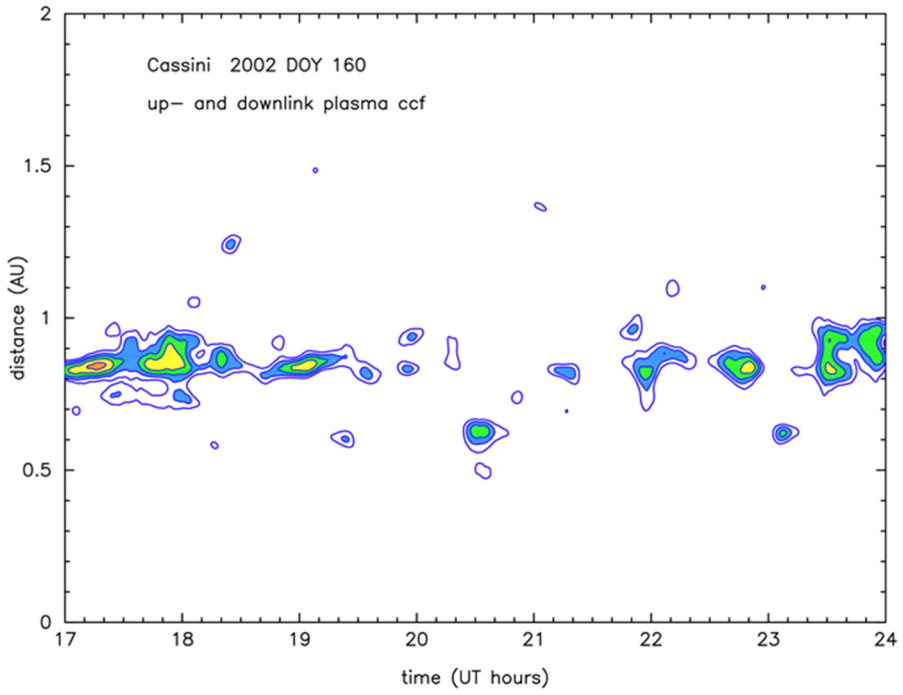

Figure RSS-40. As Figure RSS-38, but for 2002 DOY 160 = 2002 June 9. The Sun-Earth-spacecraft angle was about 9.5 degrees and the two-way light time was about 8365 seconds. Correlation levels in general lower than those in Figure RSS-38. At the start of the track a scattering region nearer to Earth than the ray path closest approach point (≈ 1AU cos (9.5 degrees) = 0.986 AU) is indicated. In mid-track the correlation is particularly low, indicative of extended, rather than localized, scattering.

OTHER SOLAR CONJUNCTION OBSERVATIONS

In addition to the 2001–2002 observations analyzed by Richie-Halford et al. [2009], subsequent solar conjunction data were collected. Full information (including Doppler modes, link information, spacecraft operational modes, exact start/stop times, etc.) are included in Project documentation [Anabtawi 2018]. Table RSS-14, for reference, is an overview of times when data were taken.

Table RSS-14. Overview of data times.

Year	Day-of-Year	Comment	Year	Day-of-Year	Comment
2005	196, 198, 208		2011	270–300	SCE8
2006	203–233	SCE3	2012	279–319	SCE9
2007	219–247	SCE4	2013	297–324	SCE10
2008	233–259	SCE5	2014	308–335	SCE11
2009	245–275	SCE6	2015	322–348	SCE12
2010	261–285	SCE7	2016	330–360	SCE13

SCE = solar conjunction experiment

Open questions

Cassini's principal non-Saturn science investigations were the gravitational wave experiment, solar conjunction relativity experiment, and solar wind plasma localization experiment. In all cases, Doppler tracking between Cassini and the DSN was used as the raw observation. The scientific objectives of future spacecraft cruise experiments would be to improve on current results.

The search for low frequency gravitational waves in space is the goal of the ongoing LISA mission, to be launched in the early 2030. This major undertaking of ESA and NASA confirms the motivations of the Cassini GWE, an attempt to search for gravitational wave sources in the mHz band at distances reaching the Virgo cluster.

The Cassini SCE increased our confidence in the validity of general relativity (GR), pushing possible violations of the metric in the solar system to the fifth decimal place. However, in spite of its apparent success, the Cassini test is just one more step in the quest for the breakdown of GR. Unfortunately, the theoretical framework does not give any clue on the level at which GR could be violated. Every test capable of improving the Cassini results is therefore significant. The BepiColombo Mission, which has a multilink radio system similar to Cassini's, with the additional feature of a pseudo-noise, high accuracy, ranging system, is expected to improve the SCE result by a factor 5–10 [Iess and Asmar 2007; Imperi and Iess 2017]. Remarkably, astrometric measurements of the gravitational deflection with the mission GAIA will reach a similar accuracy.

Here we comment on limiting noises in Cassini's precision Doppler observations and how these might be mitigated in future spacecraft cruise experiments. This section draws heavily on Bertotti et al. [2003]; Armstrong et al. [2003]; Asmar et al. [2005]; Armstrong [2006]; and Richie-Halford et al. [2009].

Precision Doppler tracking: noise in two-way observations

The Earth and the Cassini spacecraft act as separated test masses, electromagnetically tracked using microwaves. The ground stations for the Doppler system are the antennas of the NASA/JPL DSN. In particular, DSS25 was instrumented with Ka-band uplink and an advanced tropospheric calibrations system. The Cassini spacecraft was gravitationally very quiet when its attitude was controlled by reaction wheels and it had a sophisticated radio system. A precision frequency standard provided the frequency reference to both the transmitter and receiver chains. On the transmitter side, the exciter produced a near-monochromatic signal, referenced to the Fourier Transform Spectrometer (FTS) signal but at the desired transmit frequency. This was amplified by the transmitter—with closed-loop feedback around the power amplifier to ensure frequency stability was not degraded—and routed via waveguide to the transmitter feed horn in the basement of DSS25. To correct for aberration the Ka-band transmit feed horn was on a table which articulated in the horizontal plane. This allowed the Ka-band transmitted beam to be pointed correctly relative to the received beam. In a DSN beam waveguide antenna, the transmitted beam is reflected off six mirrors within the antenna up to the subreflector (near the prime focus), then back to the main dish

and out to the spacecraft (passing first through the troposphere, ionosphere, and solar wind). When the signal is received at the spacecraft, it is amplified and phase-coherently retransmitted to Earth. The received beam bounces off the main reflector to the subreflector and then, via mirrors and dichroic plates, to the receiver feed horn. The received signal is downconverted to an intermediate frequency where it is digitized. The digital samples are processed to tune out the (predictable) gross Doppler shift, and reduce the bandwidth of the samples.

For cruise operations, the bandwidth of the predetection data was typically reduced to 1 kHz and those data were recorded to disk along with the tuning information. The phase of the signal was detected in software and, using the tuning information, the received sky frequency could be reconstructed. This and the known frequency of the transmitted signal was used to compute the Doppler time series. Removal of the orbital signature and correction for charged particle and tropospheric scintillation gave Doppler residuals, which were used in subsequent processing steps for cruise experiments.

The main noises, along with the transfer functions of the noises to the two-way Doppler observable, are listed in Table RSS-15—see also Bertotti et al. [2003]; Asmar et al. [2005]; Armstrong [2006]. Cassini's multilink radio system, plus tropospheric corrections using the Advanced Media Calibration system, allowed: a) precise measurement of the PPN parameter γ [Bertotti et al. 2003]; b) improved limits to gravitational wave signal strength in the 10^{-6} to 10^{-1} Hz band [Armstrong et al. 2003]; and c) the first space-time localization of plasma turbulence in the inner heliosphere [Richie-Halford et al. 2009].

Table RSS-15. Cassini Cruise-phase Doppler noises and their transfer functions to two-way observations.

Noise source	Noise level (approx. Allan deviation at 1000s integration) during Cassini cruise phase	Transfer function of raw noise to Doppler observation (T_2 = two-way light time)
Frequency standard	8×10^{-16}	$\delta(t) - \delta(t - T_2)$
Antenna mechanical	2×10^{-15}	$\delta(t) + \delta(t - T_2)$
Ground electronics	2×10^{-16}	$\delta(t)$
Plasma scintillation	$< 10^{-15}$ at Ka-band for Sun-Earth-spacecraft angle > 150 degrees	variable, depending on effective phase screen location
Stochastic spacecraft motion	2×10^{-16}	$\delta(t - T_2/2)$
Receiver thermal	few $\times 10^{-16}$	$\delta(t)$
Spacecraft transponder	10^{-16}	$\delta(t - T_2/2)$
Tropospheric scintillation	$< 3 \times 10^{-15}$ to 30×10^{-15} (raw) $< 1.5 \times 10^{-15}$ to 3×10^{-15} (corrected)	$\delta(t) + \delta(t - T_2)$

Noise Mitigation in Future Precision Two-Way Doppler Observations

This section briefly outlines how future spacecraft Doppler observations might be made with 10x lower noise level, to a few times 10^{-16} Allan deviation at 1000s. In addition to possible innovation in Doppler extraction in the presence of moderate-to-strong interplanetary scintillation (relevant for

near-Sun relativity tracking and the decomposition of Doppler into dispersive uplink and downlink components for turbulence localization close to the Sun), Table RSS-16 shows the required improvements to the various subsystems or other noise contributors for typical tracking conditions—adapted from Armstrong [2006].

Table RSS-16. Required Noise improvement factors to reach ~10^{-16} Doppler noise.

Noise source	Comment/Allan deviation	Approximate improvement required
Frequency standard	currently ~8 × 10^{-16}	~8×
Antenna mechanical	currently ~2 × 10^{-15} under favorable conditions	~20×
Ground electronics	currently ~2 × 10^{-16}	~2×
Plasma scintillation	Cassini-class radio system probably adequate for ~10^{-16} with multilink calibration	~1×
Stochastic spacecraft motion	currently ~2 × 10^{-16}	~2×
Receiver thermal	few × 10^{-16}	~few ×
Spacecraft transponder	10^{-16}	~1×
Tropospheric scintillation	currently ~few × 10^{-15}, under favorable conditions and with calibration	~20×

Improving frequency standards and frequency distribution over what was possible in the Cassini cruise era by 8× is thought to be straightforward. Ground electronics can probably be improved by 2× by even more careful design. Similarly, spacecraft buffeting can probably be improved by 2× by careful design. Thermal noise can be improved by increasing the downlink SNR.

The big problems are antennal mechanical noise and tropospheric scintillation. These enter with the same transfer function: $\delta(t) + \delta\ (t - T_2)$. A possible way to mitigate this noise is to simultaneously track with an additional 3-way link (i.e., with a separate, listen only, ground antenna). As suggested by Estabrook [1978] and Hellings [private communication] in the context of tropospheric mitigation, a linear combination of the 2-way and 3-way Doppler data streams can be used to remove both the antenna mechanical and tropospheric noise of the 2-way station and replace it with those of the 3-way station [Armstrong et al. 2008]. If the 3-way station is located in a favorable tropospheric site and if it is mechanically stiff, this can in principle significantly improve the quality of the observation. Experiments demonstrating proof of concept have been done [Armstrong et al. 2008] and the practical limits of this approached are being investigated [Notaro et al. 2018]. These techniques may be useful in future precision radio science observations, for example BepiColombo, where substantial improvement in selected PPN parameters is possible, as well as future highly-accurate spacecraft navigation determinations [Tortora et al. 2004].

ACRONYMS

Note: For a complete list of Acronyms, refer to Cassini Acronyms – Attachment A.

AACS	Attitude and Articulation Control Subsystem
AMC	Advanced Media Calibration
AO	Announcement of Opportunity
AU	astronomical units
AU	astronomical unit
bps	bits per second
BSR	bistatic radar
C/A	closest approach
CAPS	Cassini Plasma Spectrometer
CDS	Command & Data Subsystem
CIRS	Composite Infrared Spectrometer
CME	coronal mass ejections
DOY	day of year
DSN	Deep Space Network
DSS	Deep Space Station
ELS	Electron Spectrometer
EM	electromagnetic
EOS	equation of state
ESA	electrostatic energy analyzer
FTS	Fourier Transform Spectrometer
GFO	Grand Finale Orbits
GM	gravitational mass
GR	general relativity
GSE	gravity science enhancement
GW	gigawatt
GWE	gravitational wave experiment
HASI–PWA	Huygens Atmospheric Structure and Permittivity, Wave, and Altimetry
HGA	high-gain antenna
ILR	inner Lindblad resonance
INMS	Ion and Neutral Mass Spectrometer
JPL	Jet Propulsion Laboratory
KaT	Ka-band translator
LCP	left circularly polarized
LEM	lower equipment module
LGA	low-gain antennas
LOS	line-of–sight
MHD	magneto-hydrodynamic

MOIF	moment of inertia factor
PLL	phase-locked loop
PM	periodic microstructure
PMS	Propulsion Module Subsystem
PPN	parametrized post-Newtonian
PPS	Power and Pyrotechnics Subsystem
RADAR	Titan Radar Mapper
RCP	right circularly polarized
RFIS	Radio Frequency Instrument Subsystem
RFS	Radio Frequency Subsystem
rms	root-mean-square
RPWS	Radio and Plasma Wave Spectrometer
RS	radio science
RSR	radio science receiver
RSS	Radio Science Subsystem
RSSG	Radio Science Systems Group
RTG	radioisotope thermoelectric generator
SCE	solar conjunction experiment
SEP	Sun-Earth-Probe
SNR	signal to noise ratio
SOHO	Solar and Heliospheric Observatory
SOI	Saturn Orbit Insertion
TCS	Temperature Control Subsystem
TM	Traceability Matrix
TSAC	Tracking System Analytical Calibrations
UEM	upper equipment module
USO	ultra-stable oscillator
UTC	Coordinated Universal Time
UVIS	Ultraviolet Imaging Spectrograph
VIMS	Visual and Infrared Imaging Spectrometer
VLBI	very-long-baseline interferometry
VSR	VLBI Science Receiver

REFERENCES

Disclaimer: The partial list of references below correspond with in-text references indicated in this report. For all other Cassini references, refer to Attachment B – References & Bibliographies; Attachment C – Cassini Science Bibliographies; the sections entitled References contributed by individual Cassini instrument and discipline teams located in Volume 1 Sections 3.1 and 3.2 Science Results; and other resources outside of the Cassini Final Mission Report.

Anabtawi, A., (2018), RSS Datasheet, PDS: The Planetary Atmosheres Node https://atmos.nmsu.edu/data_and_services/atmospheres_data/Cassini/logs/PDS_RSSArchivedDataProducts_Final_sorted.htm.

Anderson, J. D. and G. Schubert, (2010), Rhea's gravitational field and interior structure inferred from archival data files of the 2005 Cassini flyby, Physics of the Earth and Planetary Interiors 178, 176–182.

Anderson, J. D. and G. Schubert, (2007), Saturn's satellite Rhea is a homogeneous mix of rock and ice, Geophysical Research Letters, 34, 4–7.

Armstrong, J. W., F. B. Estabrook, S. W. Asmar, L. Iess, P. Tortora, (2008), Reducing antenna mechanical noise in precision spacecraft tracking. Radio Sci. 43, RS3010.

Armstrong, J. W., (2006), Low-frequency gravitational wave searches using spacecraft Doppler tracking, Living Reviews in Relativity, 9, 1, updated 11 January 2016.

Armstrong, J. W., L. Iess, P. Tortora, B. Bertotti, (2003), Stochastic gravitational wave background: Upper limits in the 10^{-6}–10^{-3} Hz band, The Astrophysical Journal, 599, 806–813.

Asmar,S. W., A. S. Konopliv, M. M. Watkins, J. G. Williams, R. S. Park, G. Kruizinga, M. Paik, D.-N. Yuan, E. Fahnestock, D. Strekalov, N. Harvey, W. Lu, D. Kahan, K. Oudrhiri, D. E.Smith, M. T.Zuber, (2013), The scientific measurement system of the Gravity Recovery and Interior Laboratory (GRAIL) Mission, Space Science Reviews, 178, 25–55, doi: 10.1007/s11214-013-9962-0.

Asmar, S. W, J. W. Armstrong, L. Iess, P. Tortora, (2005), Spacecraft Doppler tracking: Noise budget and accuracy achievable in precision radio science observations, Radio Science, 40, 1.

Bar-Sever Y. E., C. S. Jacobs, S. Keihm, G. E. Lanyi, C. J. Naudet, H. W. Rosenberger, T. F. Runge, A. B. Tanner, Y. Vigue-Rodi, (2007), Atmospheric media calibration for the deep space network, Proceedings of the IEEE, 95, 2180–2192.

Béghin, C., O. Randriamboarison, M. Hamelin, E. Karkoschka, C. Sotin, R. C. Whitten, J.-J. Berthelier, R. Grard, F. Simões, (2012), Analytic theory of Titan's Schumann resonance: Constraints on ionospheric conductivity and buried water ocean, Icarus, 218, 1028–1042.

Bertotti, B., L. Iess, P. Tortora, (2003), A test of general relativity using radio links with the Cassini spacecraft, Nature, 425, 374–376.

Bertotti, B., G. Comoretto, L. Iess, (1993), Doppler tracking of spacecraft with multifrequency links, Astronomy & Astrophysics, 269, 608–616.

Bertotti B. and G. Giampieri, (1992), Relativistic effects for Doppler measurements near solar conjunction, Classical and Quantum Gravity, 9, 777–793.

Bills, B. G. and F. Nimmo, (2011), Rotational dynamics and internal structure of Titan, Icarus 214, 351–355.

Bills, B. G. and F. Nimmo, (2008), Forced obliquity and moments of inertia of Titan, Icarus, 196, pp. 293–296.

Bird, M. K., R. Dutta-Roy, S. W. Asmar, T. A. Rebold, (1997), Detection of Titan’s ionosphere from Voyager 1 radio occultation observations, Icarus 130, 426–436.

Bjoraker, G., (2013), Oxygen compounds in Saturn’s atmosphere during the 2010 northern storm, American Geophysical Union (AGU) Fall Meeting, abstracts.

Buratti, B. J., (1988), Enceladus: Implications of its unusual photometric properties, Icarus 75, 113–126.

Čadek, O., G. Tobie, T. Van Hoolst, M. Massé, G. Choblet, A. Lefèvre, G. Mitri, et al., (2016), Enceladus's internal ocean and ice shell constrained from Cassini gravity, shape, and libration data, Geophysical Research Letters, 43, 5653–5660.

Campbell, J. K. and J. D. Anderson, (1989), Gravity field of the Saturnian system from Pioneer and Voyager tracking data, The Astronomical Journal, 97, 1485–1495

Castillo-Rogez, J. C. and J. I. Lunine, (2010), Evolution of Titan's rocky core constrained by Cassini observations, Geophysical Research Letters, 37, 20.

Choukroun, M. and C. Sotin, (2012), Is Titan's shape caused by its meteorology and carbon cycle? Geophysical Research Letters, 39, 4.

Collins, G. C. and J. C. Goodman, (2007), Enceladus' south polar sea, Icarus, 189, 72–82, doi: 10.1016/j.icarus.2007.01.010.

Colwell, J. E., P. D. Nicholson, M. S. Tiscareno, C. D. Murray, R. G. French, E. A. Marouf, (2009), The structure of Saturn's rings, Chapter 13, In Saturn from Cassini-Huygens, (eds.) M. K. Dougherty, L. W. Esposito, S. M. Krimigis, Springer, Dordrecht, pp. 375–412.

Connerney, J. A. P. and J. H. Waite, (1984), New model of Saturn’s ionosphere with an influx of water from the rings, Nature, 312, 136–138.

Cravens, T. E., I. P. Robertson, S. A. Ledvina, D. Mitchell, S. M. Krimigis, J. H. Waite Jr, (2008), Energetic ion precipitation at Titan, Geophysical Research Letters, 35, 3 CiteID L03103.

Cuzzi, J. N., E. A. Marouf, R. G. French, R.A. Jacobson, C. D. Murray, N. J. Cooper, (2018), Saturn’s F Ring is shepherded by Prometheus, Science Advances, in review.

Cuzzi, J., R. Clark, G. Filacchione, R. French, R. Johnson, E. Marouf, L. Spilker, (2009), Ring particle composition and size distribution, Chapter 15, In Saturn from Cassini-Huygens, (eds.) M. K. Dougherty, L. W. Esposito, S. M. Krimigis, Springer, Dordrecht, pp. 459–509.

Cuzzi, J. N. and P. R. Estrada, (1998), Compositional evolution of Saturn's rings due to meteoroid bombardment, Icarus, 132, 1–35.

Damour, T., (2003), String theory, cosmology and varying constants, Astrophysics and Space Science, 283, 445–456.

Damour T., F. Piazza, G. Veneziano, (2002), Violations of the equivalence principle in a dilaton-runaway scenario, Physical Review, D 66, no. 4, 046007, doi: 10.1103/PhysRevD.66.046007.

Damour, T. and A. M. Polyakov, (1994), The string dilaton and a least coupling principle, Nuclear Physics B, vol. 423, Issues 2–3, pp. 532–558, doi: 10.1016/0550-3213(94)90143-0.

Durante, D., D. J. Hemingway, P. Rachioopa, L. Iess, D. J. Stevenson, (2019), Titan's gravity field and interior structure after Cassini, Icarus, 326, 123–132.

Estabrook, F. B., (1978), Gravitational wave detection with the Solar Probe. II. The Doppler tracking method, In A Close-Up of the Sun (JPL Publication 78-70), September 1, 1978, pp. 441–449.

Estabrook, F. B. and H. D. Wahlquist, (1975), Response of Doppler spacecraft tracking to gravitational radiation, General Relativity and Gravitation, 6, 439–447.

Eubanks, T. M., D. N. Matsakis, J. O. Martin, B. A. Archinal, A. L. Fey, F. J. Josties, D. D. McCarty, S. A. Klioner, E. Formalont, A. J. Beasley, I. I. Shapiro, (1997), Advances in solar system tests of gravity, Joint American Physical Society (APS)/American Association of Physics Teachers (AAPT) Meeting, Washington D.C., 1997 April 18–21, paper K11.05, http://flux.aps.org/meetings/YR97/BAPSAPR97/abs/S1280005.html.

Fjeldbo, G., (1964), Bistatic radar methods for studying planetary ionospheres and surfaces, Science Report, no. 2, Stanford Electronics Laboratories, Stanford, CA, NsG-377, SU-SEL-64-025.

Flasar, F. M., R. K. Achterberg, P. J. Schinder, (2014), Thermal structure of Titan's troposphere and middle atmosphere, Chapter 3, Titan: Interior, Surface, Atmosphere, and Space Environment, (eds.) I. Müller-Wodarg, C. A. Griffith, E. Lellouch, T, E. Cravens, Cambridge University Press.

Fortes, A. D., P. M. Grindrod, S. K. Trickett, L. Vočadlo, (2007), Ammonium sulfate on Titan: Possible origin and role in cryovolcanism, Icarus, 188, 139–153.

Fortney, J. J., R. Helled, N. Nettelmann, D. J. Stevenson, M. S. Marley, W. B. Hubbard, L. Iess, (2016), The Interior of Saturn, Astrophysics: Earth and Planetary Astrophysics Cornell University, http://www.ucolick.org/~jfortney/Saturn21st.pdf.

French, R. G., C. A. McGhee-French, K. Lonergan, T. Sepersky, R. A. Jacobson, P. D. Nicholson, M. M. Hedman, E. A. Marouf, J. E. Colwell, (2017), Noncircular features in Saturn's rings IV: Absolute radius scale and Saturn's pole direction, Icarus, 290, 14–45.

French, R. G., P. D. Nicholson, C. A. McGhee-French, K. Lonergan, T. Sepersky, M. M. Hedman, E. A. Marouf, J. E. Colwell, (2016), Noncircular features in Saturn's rings III: The Cassini Division, Icarus 274, 131–162.

French, R. G., P. D. Nicholson, M. M. Hedman, J. M. Hahn, C. A. McGhee-French, J. E. Colwell, E. A. Marouf, N. J. Rappaport, (2016), Deciphering the embedded wave in Saturn's Maxwell ringlet, Icarus, 279, 62–77.

García-Melendo, E., S. Pérez-Hoyos, A. Sánchez-Lavega, R. Hueso, Saturn's zonal wind profile in 2004–2009 from Cassini ISS images and its long-term variability, Icarus, 215, no. 1, 62–74.

Hedman, M. M., C. M. Gosmeyer, P. D. Nicholson, C. Sotin, Robert H. Brown, R. N. Clark, K. H. Baines, B. J. Buratti, M. R. Showalter, (2013), An observed correlation between plume activity and tidal stresses on Enceladus, Nature, 500, 182–184, doi: 10.1038/nature12371.

Hellings, R., (private communication).

Hemingway, D., F. Nimmo, H. Zebker, L. Iess, (2013), A rigid and weathered ice shell on Titan, Nature, 500, 550–552, doi: 10.1038/nature12400.

Howett, C. J. A., J. R. Spencer, J. Pearl, M. Segura, (2011), High heat flow from Enceladus' south polar region measured using 10-600 cm^{-1} Cassini/CIRS data, Journal of Geophysical Research, vol. 116, Issue E3, doi: 10.1029/2010JE003718.

Hubbard, W. B., (1999), Gravitational signature of Jupiter's deep zonal flows, Icarus, vol. 137, Issue 2, pp. 357–359, doi: 10.1006/icar.1998.6064.

Iess, L., B. Militzer, Y. Kaspi, P. Nicholson, D. Durante, P. Racioppa, A. Anabtawi, et al., (2019), Measurement and implications of Saturn's gravity and ring mass, Science, vol. 364, Issue 6445, eaat2965, doi: 10.1126/science.aat2965.

Iess, L., W. M. Folkner, D. Durante, M. Parisi, Y. Kaspi, E. Galanti, and D. R. Buccino, (2018), Measurement of Jupiter's asymmetric gravity field, Nature, 555, 220–222, doi: 10.1038/nature25776.

Iess, L., D. J. Stevenson, M. Parisi, D. Hemingway, R. A. Jacobson, J. I. Lunine, F. Nimmo, et al., (2014), The gravity field and interior structure of Enceladus, Science, 344, 78–80, doi: 10.1126/science.1250551.

Iess, L., P. Racioppa, N. J. Rappaport P. Tortora, (2012), The tides of Titan, Science, 337, 457–459, doi: 10.1126/science.1219631.

Iess, L., N. J. Rappaport, R. A. Jacobson, P. Racioppa, D. J. Stevenson, P. Tortora, J. W. Armstrong, S. W. Asmar, (2010), Gravity field, shape, and moment of inertia of Titan, Science, 327, 1367, doi: 10.1126/science.1182583.

Iess, L., N. J. Rappaport, P. Tortora, J. Lunine, J. W. Armstrong, S. W. Asmar, L. Somenzi, F. Zingoni, (2007), Gravity field and interior of Rhea from Cassini data analysis, Icarus, 190, 585–593.

Iess, L. and S. Asmar, (2007), Probing space-time in the solar system: from Cassini to BepiColombo, International Journal of Modern Physics D, vol. 16, no. 12a, pp. 2117–2126, doi: 10.1142/S0218271807011449.

Iess, L., N. Rappaport, P. Tortora, G. Rapino, L. Somenzi, (2005), The determination of Iapetus mass from Doppler tracking of the Cassini spacecraft, In Geophysical Research Abstracts, European Geosciences Union General Assembly, Vienna, Austria, 24–29 April 2005, vol. 7, Union Symposia, US9 Titan-Huygens-Cassini: First Results, US9/PS1.5-1MO4O-002, EGU05-A-11176, https://www.cosis.net/abstracts/EGU05/11176/EGU05-J-11176-1.pdf.

Iess, L., R. A. Jacobson, M. Ducci, D. J. Stevenson, J. I. Lunine, J. W. Armstrong, S. W. Asmar, S. J. Keihm, A. Tanner, H. Rosenberger, (2004), Measurements and calibration of tropospheric delay at Goldstone from the Cassini Media Calibration System, IPN Progress Report, 42–158.

Iess L., P. Tortora, J. D. Anderson, S. W. Asmar, E. Barbinis, B. Bertotti, D. U. Fleischman, M. S. Gatti, et al., (2003), The Cassini solar conjunction experiment: a new test for general relativity, IEEE Aerospace Conference, Big Sky, MT, 8–15 March 2003, IEEE Aerospace Conference Proceedings (Cat. No.03TH8652), https://ieeexplore.ieee.org/stamp/stamp.jsp?tp=&arnumber=1235053.

Iess, L., G. Giampieri, J. D. Anderson, B. Bertotti, (1999), Doppler measurement of the solar gravitational deflection, Classical and Quantum Gravity, 16, 5, 1487–1502.

Imperi, L. and L. Iess, (2017), The determination of the post-Newtonian parameter γ during the cruise phase of BepiColombo, Classical and Quantum Gravity, vol. 34, no. 7, 075002, doi: 10.1088/1361-6382/aa606d.

Jacobson, R. A., P. G. Antreasian, J. J. Bordi, K. E. Criddle, R. Ionasescu, J. B. Jones, R. A. Mackenzie, et al., (2006), The gravity field of the Saturnian system from satellite observations and spacecraft tracking data, The Astronomical Journal, vol. 132, no. 6, pp. 2520–2526.

Jacobson, R. A., (2004), The orbits of the major Saturnian satellites and the gravity field of Saturn from spacecraft and Earth-based observations, The Astronomical Journal, vol. 128, no. 1, pp. 492–501.

Kaspi, Y., E. Galanti, W. B. Hubbard, D. J. Stevenson, S. J. Bolton, L. Iess, and D. Durante, (2018), Jupiter’s atmospheric jet streams extend thousands of kilometres deep, Nature, 555, 223–226, doi: 10.1038/nature25793.

Kaspi, Y., (2013), Inferring the depth of the zonal jets on Jupiter and Saturn from odd gravity harmonics, Geophysical Research Letters, 40, 676–680.

Kliore, A. J., A. Nagy, S. Asmar, A. Anabtawi, E. Barbinis, D. Fleischman, D. Kahan, J. Klose, (2014), The ionosphere of Saturn as observed by the Cassini radio science system, Geophysical Research Letters, 41, no. 16, 5778–5782.

Kliore, A. J., A. F. Nagy, T. E. Cravens, M. S. Richard, A. M. Rymer, (2011), Unusual electron density profiles observed by Cassini radio occultation in Titan’s ionosphere: Effects of enhanced magnetospheric electron precipitation, Journal of Geophysical Research, 116, A11, CiteID A11318.

- - - - - - - - - - - - - -

Kliore, A. J., A. Nagy, E. Marouf, (2010), The plasma cloud of Enceladus, In European Planetary Science Congress, Angelicum Centre – Pontifical University of Saint Thomas Aquinas, 19–24 September 2010, Rome, Italy, EPSC abstracts, vol. 5, EPSC2010-113.

Kliore, A. J., A. F. Nagy, E. A. Marouf, A. Anabtawi, E. Barbinis, D. U. Fleischman, D. S. Kahan, (2009), Mid-latitude and high latitude electron density profiles in the ionosphere of Saturn obtained by radio occultations, Journal of Geophysical Research: Space Physics, 114, A4, CiteID A04315.

Kliore, A. J., A. F. Nagy, E. A. Marouf, R. G. French, F. M. Flasar, N. J. Rappaport, A. Anabttawi et al., (2008), First results from the Cassini radio occultations of the Titan ionosphere, Journal of Geophysical Research: Space Physics, 113, A9, CiteID A09317.

Kliore, A. J., J. Armstrong, F. Flasar, R. French, E. Marouf, A. Nagy, N. Rappaport, et al., (2006), Cassini radio occultation by Enceladus plume, American Geophysical Union (AGU) Fall Meeting, abstract.

Kliore, A. J., J. D. Anderson, J. W. Armstrong, S. W. Asmar, C. L. Hamilton, N. J. Rappaport, H. D. Wahlquist, R. Ambrosini, F. M. Flasar, R. G. French, L. Iess, E. A. Marouf, A. F. Nagy, (2004), Cassini Radio Science, Space Science Reviews, 115, Issue 1–4, 1–70.

Kozai, Y., (1957), Observations of the satellites of Saturn, Annals of the Tokyo Astronomical Observatory, Series 25, 73.

Lebonnois, S., F. M. Flasar, T. Tokano, C. Newman, (2014), The general circulation of Titan's lower and middle atmosphere, Chapter 4, In Titan: Interior, Surface, Atmosphere, and Space Environment, (eds.) I. Müller-Wodarg, C. A. Griffith, E. Lellouch, T. E. Cravens, Cambridge University Press, pp. 122–157, doi: 10.1017/CBO9780511667398.007.

Lorenz, R. D., B. W. Stiles, R. L. Kirk, M. D. Allison, P. Persi del Marmo, L. Iess, J. I. Lunine, S. J. Ostro, S. Hensley, (2008), Titan's rotation reveals an internal ocean and changing zonal winds, Science, 319, 5870, 1649–1651.

Mackenzie, R. A., L. Iess, P. Tortora, N. J. Rappaport, (2008), A non-hydrostatic Rhea, Geophysical Research Letters, 35, L05204, doi: 10.1029/2007GL032898, pp. 1–5.

Mackenzie, R. A., P. G. Antreasian, J. J. Bordi, K. E. Criddle, R. Ionasescu, R. A. Jacobson, J. B. Jones, D. W. Parcher, F. J. Pelletier, D. C. Roth, J. R. Stauch, (2007), A determination of Rhea’s gravity field from Cassini navigation analysis. Proceedings of the American Astronomical Society (AAS)/American Institute of Aeronautics and Astronautics (AIAA) 17th Space Flight Mechanics Meetings, 28 January–1 February 2007, Sedona, AZ.

Mariotti, G. and P. Tortora, (2013), Experimental validation of a dual uplink multifrequency dispersive noise calibration scheme for Deep Space tracking, Radio Science, vol. 48, Issue 2, pp. 111–117, doi: 10.1002/rds.20024.

Marouf, N. Rappaport, R. French, R. Simpson, A. Kliore, C. McGhee, P. Schinder, A. Anabtawi, (2008), Dialectric constant of Titan’s south polar region from Cassini Radio Science bistatic scattering observations, American Geophysical Union (AGU) Fall Meeting, abstract P21A-1319.

Marouf, E., M. Flasar, R. French, A. Kliore, A. Nagy, N. Rappaport, C. McGhee et al., (2006), Evidence for likely liquid hydrocarbons on Titan's surface from Cassini Radio Science bistatic scattering observations, American Geophysical Union (AGU) Fall Meeting, abstract P11A-07.

Marouf, E. A., G. L. Tyler, P. A. Rosen, (1986), Profiling Saturn's rings by radio occultation, Icarus vol. 68, Issue 1, pp. 120–166, doi: 10.1016/0019-1035(86)90078-3.

Marouf, E. A., G. L. Tyler, H. A. Zebker, R. A. Simpson, V. R. Eshleman, (1983), Particle-size distributions in Saturn's rings from Voyager 1 radio occultation, Icarus, 54, pp. 189–211.

McKinnon, W. B., (2015), Effect of Enceladus's rapid synchronous spin on interpretation of Cassini gravity, Geophysical Research Letters, 42, 2137–2143, doi: 10.1002/2015GL063384.

Meyer, J. and J. Wisdom, (2007), Tidal heating in Enceladus, Icarus, 188, 535–539.

Mitri, G., R. Meriggiola, A. Hayes, A. Lefevre, G. Tobie, A. Genova, J. I. Lunine, H. Zebker, (2014), Shape, topography, gravity anomalies and tidal deformation of Titan, Icarus, 236, 169–177.

Morooka, M. W., J.-E. Wahlund, A. I. Eriksson, W. M. Farrell, D. A. Gurnett, W. S. Kurth, A. M. Persoon, M. Shafiq, M. Andre, M. K. G. Holmberg, (2011), Dusty plasma in the vicinity of Enceladus, Journal of Geophysical Research, 116, A12221, doi: 10.1029/2011JA017038.

Murphy, M. T., J. K. Webb, V. V. Flambaum, V. A. Dzuba, C. W. Churchill, J. X. Prochaska, J. D. Barrow, A. M. Wolfe, (2001a), Possible evidence for a variable fine-structure constant from QSO absorption lines: Motivations, analysis and results, Monthly Notices of the Royal Astronomical Society (MNRAS), 327, 1208–1222.

Murphy, M. T., J. K. Webb, V. V. Flambaum, C. W. Churchill, J. X. Prochaska, (2001b), Possible evidence for a variable fine-structure constant from QSO absorption lines: systematic errors. Monthly Notices of the Royal Astronomical Society (MNRAS), 327, 1223–1236.

Murphy, M. T., J. K. Webb, V. V. Flambaum, J. X. Prochaska, A. M. Wolfe, (2001c), Further constraints on variation of the fine-structure constant from alkali-doublet QSO absorption lines. Monthly Notices of the Royal Astronomical Society (MNRAS), 327, 1237–1243.

Murphy, M. T., J. K. Webb, V. V. Flambaum, M. J. Drinkwater, F. Combes, T. Wiklind, (2001d), Improved constraints on possible variations of physical constants from H I 21-cm and molecular QSO absorption lines, Monthly Notices of the Royal Astronomical Society (MNRAS), 327, 1244–1248.

Nagy, A. F., A. J. Kliore, E. Marouf, R. French, M. Flasar, N. J. Rappaport, A. Anabtawi, et al., (2006), First results from the ionospheric radio occultations of Saturn by the Cassini spacecraft, Journal of Geophysical Research, 111, A6, CiteID A06310.

Nicholson, P. D., R. G. French, M. M. Hedman, E. A. Marouf, J. E. Colwell, (2014a), Noncircular features in Saturn’s rings I: The edge of the B ring, Icarus, 227, 152–175.

Nicholson, P.D., R. G. French, C. A. McGhee-French, M. M. Hedman, E. A. Marouf, J. E. Colwell, K. Lonergan, T. Sepersky, (2014b), Noncircular features in Saturn’s rings II: The C ring, Icarus 241, 373–396.

Nimmo, F., B. G. Bills, P. C. Thomas, (2011), Geophysical implications of the long-wavelength topography of the Saturnian satellites, Journal of Geophysical Research, 116, E11001.

Nixon, C. A., R. D. Lorenz, R. K. Achterberg, A. Buch, P. Coll, R. N. Clark, R. Courtin, et al., (2018), Titan's cold case files - Outstanding questions after Cassini-Huygens, Planetary and Space Science, 155, 50–72.

Notaro, V., M. J. Mariani, A. Di Duscio, L. Iess, J. W. Armstrong, S. W. Asmar, (2018), Feasibility of an innovative technique for noise reduction in spacecraft doppler tracking, IEEE Aerospace Conference, 3–10 March 2018, Big Sky, MT, paper 2187 3.

Null, G. W., E. L. Lau, E. D. Biller, J. D. Anderson, (1981), Saturn gravity results obtained from Pioneer 11 tracking data and Earth-based Saturn satellite data, The Astronomical Journal, 86, 456–468.

O'Donoghue, J., T. S. Stallard, H. Melin, G. H. Jones, S. W. H. Cowley, S. Miller, K. H. Baines, J. S. D. Blake, (2013), The domination of Saturn's low-latitude ionosphere by ring 'rain', Nature, 496, 193–195.

Ojakangas, G. W. and D. J. Stevenson, (1986), Episodic volcanism of tidally heated satellites with application to Io, Icarus, 66, 341.

Postberg, F., J. Schmidt, J. Hillier, S. Kempf, R. Srama, (2011), A salt-water reservoir as the source of a compositionally stratified plume on Enceladus, Nature, 474, 620.

Rappaport, N. J., P.-Y. Longaretti, R. G. French, E. A. Marouf, C. A. McGhee, (2009), A procedure to analyze nonlinear density waves in Saturn's rings using several occultation profiles, Icarus, vol. 199, Issue 1, pp. 154–173, doi: 10.1016/j.icarus.2008.08.014.

Rappaport, N. J., L. Iess, J. Wahr, J. I. Lunine, J. W. Armstrong, S. W. Asmar, P. Tortora, M. Di Benedetto, P. Racioppa, (2008), Can Cassini detect a subsurface ocean in Titan from gravity measurements?, Icarus, 194, 711–720.

Rappaport, N. J., L. Iess, P. Tortora, S. W. Asmar, L. Somenzi, A. Anabtawi, E. Barbinis, D. U. Fleischman, G. L. Goltz, (2005), Gravity science in the Saturnian system: the masses of Phoebe, Iapetus, Dione and Enceladus, 37th Annual Meeting of the Division for Planetary Sciences of the American Astronomical Society, Cambridge, UK, 4–9 September 2005, presentation 39.02.

Reasenberg, R. D., I. I. Shapiro, P. E. MacNeil, R. B. Goldstein, J. C. Breidenthal, J. P. Brenkle, D. L. Cain, T. M. Kaufman, T. A. Komarek, A. I. Zygielbaum, (1979), Viking Relativity Experiment: Verification of signal retardation by solar gravity, The Astrophysical Journal, 234, 219–221.

Resch, G. M., S. J. Keihm, G. E. Lanyi, R. P. Linfield, C. J. Naudet, A. L. Riley, H. W. Rosenberger, A. B. Tanner, (2002), The media calibration system for Cassini Radio Science: Part III, IPN Progress Report, 42–148.

Richie-Halford, A. C., L. Iess, P. Tortora, J. W. Armstrong, S. W. Asmar, R. Woo, S. R. Hab-bal, H. Morgan, (2009), Space-time localization of heliospheric plasma turbulence using multiple spacecraft links, Space Weather 7, S12003, doi: 10.1029/2009SW000499.

Sanchez-Lavega, A., J. F. Rojas, P. V. Sada, (2000), Saturn's zonal winds at cloud level, Icarus, vol. 147, Issue 2, pp. 405–420, doi: 10.1006/icar.2000.6449.

Schinder, P. J., F. M. Flasar, E. A. Marouf, R. G. French, E. Barbinis, D. Fleischman, A. Anabtawi, R. K. Achterberg, (2019), The structure of Titan's atmosphere from Cassini radio occultations: One- and two- way occultations, Icarus, submitted 26 July 2019.

Schinder, P. J., F. M. Flasar, E. A. Marouf, R. G. French, A. Anabtawi, E. Barbinis, A. J. Kliore, (2015), A numerical technique for two-way radio occultations by oblate axisymmetric atmospheres with zonal winds, Radio Science, 50, 712–727.

Schinder, P. J., F. M. Flasar, E. A. Marouf, R. G. French, C. A. McGhee, A. J. Kliore, N. J. Rappaport, E. Barbinis, D. Fleischman, A. Anabtawi, (2012), The structure of Titan's atmosphere from Cassini radio occultations: Occultations from the Prime and Equinox missions, Icarus, 221, 1020–1031.

Schinder, P. J., F. M. Flasar, E. A. Marouf, R. G. French, C. A. McGhee, A. J. Kliore, N. J. Rappaport, E. Barbinis, D. Fleischman, A. Anabtawi, (2011a), Saturn's equatorial oscillation: Evidence of descending thermal structure from Cassini radio occultations, Geophysical Research Letters, 38, L08205.

Schinder, P. J., F. M. Flasar, E. A. Marouf, R. G. French, C. A. McGhee, A. J. Kliore, N. J. Rappaport, E. Barbinis, D. Fleischman, A. Anabtawi, (2011b), The structure of Titan's atmosphere from Cassini radio occultations, Icarus 215, 460–474.

Simpson, R. A., (2007), Planetary Exploration, Chapter 5, In Advances in Bistatic Radar, (eds.) N. J. Willis, H. D. Griffiths, SciTech Publishing Inc., pp. 56–77.

Sohl, F., H. Hussmann, B. Schwentker, T. Spohn, R. D. Lorenz, (2003), Interior structure models and tidal Love numbers of Titan, Journal of Geophysical Research: Planets, vol. 108, Issue E12, doi: 10.1029/2003JE002044.

Spencer, J. R., J. C. Pearl, M. Segura, F. M. Flasar, A. Mamoutkine, P. Romani, B. J. Buratti, A. R. Hendrix, L. J. Spilker, R. M. C. Lopes, (2006), Cassini encounters Enceladus: Background and the discovery of a south polar hot spot, Science, 311, 1401–1405.

Spitale, J. N. and C. C. Porco, (2007), Association of the jets of Enceladus with the warmest regions on its south-polar fractures, Nature, 449, 695.

Thomas, P. C., R. Tajeddine, M. S. Tiscareno, J. A. Burns, J. Joseph, T. J. Loredo, P. Helfenstein, C. Porco, (2016), Enceladus's measured physical libration requires a a global subsurface ocean, Icarus, 264, 37–47.

Thomas, P. C., J. A. Burns, P. Helfenstein, S. Squyres, J. Veverka, C. Porco, E. P. Turtle, et al., (2007), Shapes of the Saturnian icy satellites and their significance, Icarus, 190, 573–584, doi: 10.1016/j.icarus.2007.03.012.

Thomas, P. C., J. W. Armstrong, S. W. Asmar, J. A. Burns, T. Denk, B. Giese, P. Helfenstein, L. Iess, T. V. Johnson, A. McEwen, L. Nicolaisen, C. Porco, N. Rappaport, J. Richardson, L., Somenzi, P. Tortora, E. P. Turtle, J. Veverka, (2007), Hyperion sponge-like appearance, Nature, 448, 50–53.

Thomson, F. S., E. A. Marouf, G. L. Tyler, R. G. French, N. J. Rappaport, (2007), Periodic microstructure in Saturn's rings A and B, Geophysical Research Letters, 34, L24203.

Thorne, K. S., (1987) Gravitational radiation, In Three Hundred Years of Gravitation, (eds.) S. W. Hawking, W. Israel, Cambridge University Press, pp. 330–458.

Tobie, G., D. Gautier, F. Hersant, (2012), Titan's bulk composition constrained by Cassini-Huygens: implication for internal outgassing, The Astrophysical Journal, 752, no. 2, 125.

Tobie, G., O. Čadek, C. Sotin, (2008), Solid tidal friction above a liquid water reservoir as the origin of the south pole hotspot on Enceladus, Icarus, 196, 642–652, doi: 10.1016/j.icarus.2008.03.008.

Tobie, G., J. I. Lunine, C. Sotin, (2006), Episodic outgassing as the origin of atmospheric methane on Titan, Nature, 440, 7080, 6.

Tobie, G., A. Mocquet, C. Sotin, (2005), Tidal dissipation within large icy satellites: Applications to Europa and Titan, Icarus 177, 534–549.

Tortora, P., M. Zannoni, D. Hemingway, F. Nimmo, R. A. Jacobson, L. Iess, M. Parisi, (2016), Rhea gravity field and interior modeling from Cassini data analysis, Icarus, 264, 264–273, doi: 10.1016/j.icarus.2015.09.022.

Tortora, P., M. Zannoni, D. Hemingway, F. Nimmo, R.A. Jacobson, L. Iess, M. Parisi, (2015), Rhea gravity field and interior modeling from Cassini data analysis, Icarus, 264, 264–273, doi: 10.1016/j.icarus.2015.09.022.

Tortora, P., J. W. Armstrong, S. W. Asmar, L. Iess, N. J. Rappaport, A. Ardito, L. Somenzi, (2009), Cassini's determination of the gravity fields of the Saturnian satellites, 58th International Astronautical Congress, 24–28 September 2009, Hyderabad, India, paper IAC-07- A3.I.A.29, pp. 1263–1271.

Tortora, P., L. Iess, J. J. Bordi, J. E. Ekelund, D. C. Roth, (2004), Precise Cassini navigation during solar conjunctions through multifrequency plasma calibrations, Journal of Guidance, Control and Dynamics, 27, 251–257.

Tortora, P., L. Iess, R. G. Herrera, (2003), The Cassini multifrequency link performance during 2002 solar conjunction, IEEE Aerospace Conference, 8–15 March 2003, Big Sky, MT, vol. 3, 1465–1473.

Tortora, P., L. Iess, J. E. Ekelund, (2002), Accurate navigation of deep space probes using multifrequency links: The Cassini breakthrough during solar conjunction experiments, The World Space Congress, 10–19 October 2002, Houston, TX.

Tyler, G. L., V. R. Eshleman, J. D. Anderson, G. S. Levy, G. F. Lindal, G. E. Wood, T. A. Croft, (1982), Radio science with Voyager 2 at Saturn: Atmosphere and ionosphere and the masses of Mimas, Tethys, and Iapetus, Science, 215, 553–558.

Tyler, G. L., V. R. Eshleman, J. D. Anderson, G. S. Levy, G. F. Lindal, G. E. Wood, T. A. Croft, (1981), Radio science investigations of the Saturn system with Voyager 1: Preliminary results, Science, 212, 201–206.

Vessot, R. F. C. and B. W. Levine, (1978), A timed-correlated four-link Doppler tracking system, In a close-up of the Sun, JPL Publication 78-70, pp. 457–497.

Wahl, S. M., W. B. Hubbard, B. Militzer, T. Guillot, Y. Miguel, N. Movshovitz, Y. Kaspi, et al., (2017), Comparing Jupiter interior structure models to Juno gravity measurements and the role of a dilute core, Geophysical Research Letters, vol. 44, Issue 10, 4649–4659, doi: 10.1002/2017GL073160.

Wahlund, J. E., M. W. Morooka, L. Hadid, D. J. Andrews, W. S. Kurth, G. Hospodarsky, A. M. Persoon, (2017), First in-situ determination of the ionospheric structure of Saturn by Cassini/RPWS, In European Planetary Science Congress, vol. 11.

Waite, J. H., C. R. Glein, R. S. Perryman, B. D. Teolis, B. A. Magee, G. Miller, J. Grimes, et al., (2017), Cassini finds molecular hydrogen in the Enceladus plume: evidence for hydrothermal processes, Science, 356, no. 6334, 155–159.

Waite Jr., J. H., (2017), Cassini INMS Measurements of Saturn's Atmosphere and Ionosphere, In American Geophysical Union (AGU) Fall Meeting, abstract.

Will, C. M., (1993), Theory and experiment in gravitational physics, Cambridge University Press.

Zannoni, M., P. Tortora, L. Iess, R. A. Jacobson, J. W. Armstrong, S. W. Asmar, (2015), The determination of Dione’s gravity field after four Cassini flybys, European Geoscience Union (EGU) General Assembly, 12–17 April 2015, Vienna, Austria, Id.13211.

Zebker, H. A., B. Stiles, S. Hensley, R. Lorenz, R. L. Kirk, J. Lunine, (2009), Size and shape of Saturn's moon Titan, Science, vol. 324, Issue 5929, pp. 921–923, doi: 10.1126/science.1168905.

Zebker, H. A., E. A. Marouf, G. Leonard Tyler, (1985), Saturn's rings: Particle size distributions for thin layer models, Icarus, 64, no. 3, 531–548.

Zhang, K. and F. Nimmo, (2009), Recent orbital evolution and the internal structures of Enceladus and Dione, Icarus, 204, 597.

- - - - - - - - - - - - - -